Design and execution of energy piles : Validation by in-situ and laboratory experiments

Andreea-Roxana Vasilescu

THESE DE DOCTORAT DE

L'ÉCOLE CENTRALE DE NANTES

COMUE UNIVERSITE BRETAGNE LOIRE

Par

Andreea-Roxana VASILESCU

DESIGN AND EXECUTION OF ENERGY PILES

VALIDATION BY IN-SITU AND LABORATORY TESTS

Rapporteurs avant soutenance :

Pierre Breul   Professeur des Universités, Université Clermont Auvergne
Frédéric Collin   Professeur des Universités, Université de Liège

Composition du Jury :

Président :   Jean-Michel PEREIRA   Professeur des Universités, Ecole des Ponts Paris Tech

Examinateurs : Pierre BREUL   Professeur des Universités, Université Clermont Auvergne
                 Frédéric COLLIN   Professeur des Universités, Université de Liège
                 Alice DI DONNA   Maître de Conférences, Université Grenoble Alpes
                 Jean-Michel PEREIRA   Professeur des Universités, Ecole des Ponts Paris Tech

Dir. de thèse : Panagiotis KOTRONIS   Professeur des Universités, Ecole Centrale de Nantes
Encadrants: Christophe DANO   Maître de Conférences, Université Grenoble Alpes
                 Anne-Laure FAUCHILLE   Maître de Conférences, Ecole Centrale de Nantes

Invité(s)
Richard MANIRAKIZA   Directeur Technique, ENTREPRISE PINTO

ACKNOWLEDGEMENTS

RÉSUMÉ

Les pieux énergétiques représentent une solution alternative intéressante, face à l'accroissement des besoins mondiaux en énergie et à la réduction de l'utilisation des énergies fossiles. Les pieux géothermiques sont des fondations profondes à double fonction: elles reprennent les charges de la structure et sont des échangeurs thermiques (Brandl 2006). La température du sol est généralement constante au cours de l'année pour des profondeurs supérieures à 5m (Williams & Gold Veuillez 1977) et se situe autour de 13°C en France. Pour profiter de cette énergie contenue dans le sol, les pieux sont équipés d'un système de tubes dans lequel la circulation (en circuit fermé) d'un fluide caloporteur permet l'échange thermique entre les pieux et le sol afin de chauffer ou refroidir le bâtiment selon la saison. Au fil des saisons, ces pieux sont soumis à des cycles de chauffage et de refroidissement entraînant respectivement des cycles de dilatation et de contraction, qui participent à l'augmentation de déplacements verticaux et la modification de la contrainte verticale dans les pieux, de la résistance du sol ou de manière plus générale à des modifications du comportement thermomécanique du sol. Cependant, malgré le nombre croissant des études sur les pieux géothermiques ces dernières années, l'impact de cycles thermomécaniques sur le comportement du sol et de l'interface sol-pieu sont encore mal documentés.

L'objectif principal de la thèse est d'identifier et de quantifier les principaux facteurs influençant le dimensionnement des pieux géothermiques, qui sont impactés par les changements de température des pieux lors de leur activité. Pour ce faire, ce travail de thèse a été dressé en 3 campagnes expérimentales, dont deux à échelle réelle : (i) une première campagne à chargement thermomécanique contrôlé (Marne La Vallée), (ii) une seconde campagne en conditions d'utilisation réelles sous une station d'épuration (Sept Sorts) et (iii) une troisième campagne à l'échelle du laboratoire grâce à une nouvelle machine de cisaillement direct d'interface permettant l'étude du comportement thermo mécanique des interfaces sol-structure. Ces trois campagnes expérimentales ont pour but de quantifier l'effet de la température et des cycles de température sur le comportement des pieux énergétiques. Les premiers résultats expérimentaux de la campagne de Sept Sorts ont ensuite été simules dans le code LAGAMINE via la méthode des éléments finis, afin d'adopter une approche complémentaire permettant de mieux appréhender la réponse thermomécanique de ce type de pieu lors de l'activation géothermique.

ABSTRACT

The global energy demand as well as the socio-economical stakes concerning the increase of energy costs due to fossil fuels has stimulated the research for new sustainable and cost effective energy sources. Energy piles, also called thermo-active piles, are an alternative solution for heating and/or cooling needs. Energy piles are double purpose structures that allow transferring the loads from the superstructure to the soil and that integrate pipe circuits allowing heat exchange between the pile and the surrounding ground. It is due to the fact that below 5m deep, the soil temperature, around 13°C in France, remains constant throughout the year, hence the soil can be used as a source of heat during winter and conversely as a heat sink during summer. During the operation of the ground source system energy piles undergo cyclic temperature changes that can have an impact on the pile mechanical behaviour as well as on the soil-pile interface. Although this solution has been used for some time and an increasing number of research results are available on this topic, the information concerning the long term behaviour of the foundation and of the surrounding soil is still limited.

The objective of this thesis is to identify and quantify the principal parameters involved in the geotechnical design of pile foundations impacted by temperature changes associated with geothermal activation. For this purpose, this research work was organised in 3 experimental campaigns: (i) A full scale load controlled test at Ecole des Ponts Paris-Tech, (ii) Full scale energy piles monitoring under real exploitation conditions at Sept Sorts, (Seine et Marne, France), (iii) Laboratory tests in order to assess the effect of temperature and temperature cycles at the soil-pile interface. The experimental results are used to estimate the effect of geothermal activation of a pile foundation, on its bearing capacity as well as on its long-term exploitation. Finally, preliminary numerical simulations were performed using a thermo-hydro mechanical model, using the finite element method code LAGAMINE able to capture the main phenomena.

CONTENTS

INTRODUCTION

The global aim to reduce greenhouse gas emission to avoid the energy dependence on fossil fuels and the new building energy requirements have urged the search for new environmentally friendly energy sources worldwide. Directive 2001/77/EC laid down a framework for encouraging energy production from renewable energy sources in the European Union. This framework was further reinforced by Directive 2009/28/EC which requires member states to establish mandatory national targets consistent with the EU strategy. In the case of France it was set that by 2020, 23% of the energy consumed should come from renewable energy sources. This percentage should further increase to 32% by 2030.

According to the European Environment Agency, the building sector (residential and tertiary buildings) accounted for about 25.71% of the end-use energy consumption in 2016. Moreover, heating represents the source of an average of 69.1% of the energy consumption of French homes. Similar values of the energy use can be found in other countries with comparable climate, while in cold climate countries, building heating can account for more than 80% of the entire energy consumption in the residential and tertiary sector (Figure 0-1 a, b).
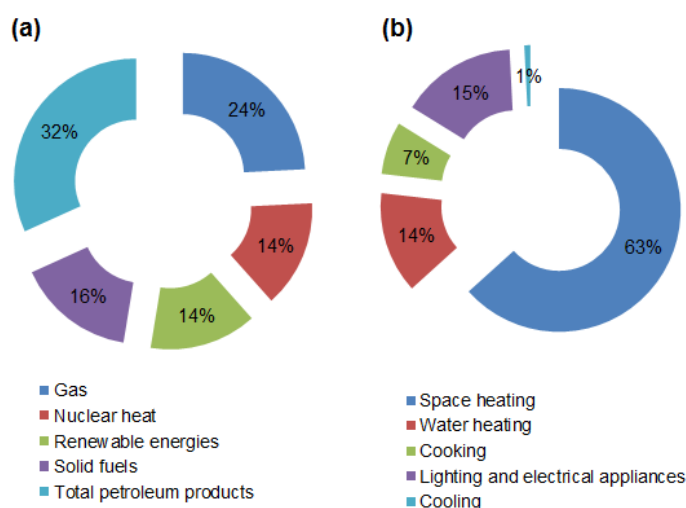
Figure 0-1 Energy consumption in Europe, according to the European Environment Agency (a) by energy vector, (b) by sector.

Furthermore, energy consumption in European buildings is responsible for around 25% of the total CO_2 emissions (Connolly et al. 2012). In order to address target reductions for low-carbon economies, new buildings must comply strict requirements on energy efficiency, such as the Directive 2010/31/EU regarding 'Nearly zero-energy Building (NZEB)'. Geothermal District Heating is considered a key technology to decarbonise the heat sector and reduce Europe's dependency from fossil fuels. This approach is based on the use of geothermal energy to provide heat through a distribution network. Current installed capacity is 4,400 MWth and it is forecasted that it will grow to 6,500 MWth in 2018 (EGEC 2011).

To comply with NZEB regulations, the use of shallow geothermal heat (i.e. those using the thermal energy from depths up to 100 m) for heating and cooling of buildings has experimented lastly an expansion. Energy geostructures such as energy piles represent the next generation of ground heat exchangers for geothermal heat pumps. Energy pile foundations are double purpose structures as they are used for transferring loads from the structure to the ground and as energy production systems due to the fact that they are equipped with polyethylene pipes (the heat exchange system) through which a heat carrier fluid is circulated (Figure 0-2).
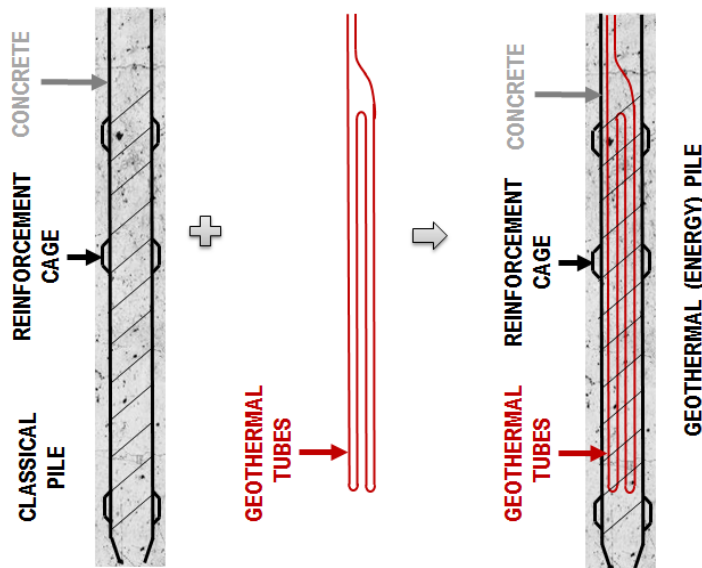
Figure 0-2 Energy piles structure.

The system, connected to a heat pump, extracts thermal energy for heating or injects it into the ground for cooling purpose. A single energy pile may deliver on average between 25-50W/m (SIA 2005) depending on its size, construction details, soil stratification or how it is operated.

However, despite the promising capabilities, the deployment of energy piles has been hindered by several factors such as: (i) insufficient information on the pile response to pile cyclic thermal loading, (ii) lack of reliable data on the long-time behaviour of energy foundations, (iii) high installation costs due to non-standardized procedures.

Research objectives

This PhD thesis resulted as the collaboration between PINTO, the French National Federation of Public Works (FNTP) and Centrale Nantes (thèse CIFRE) and presents a framework for understanding the factors participating in the energy piles design and execution. The main goal of this work is to improve the understanding of the thermo-mechanical behavior of energy piles, hence the main objectives set are:

- Objective 1: Identify the physical processes and geotechnical challenges involved in the geothermal activation of pile foundations
- Objective 2: Qualitative and quantitative characterization of the impact of geothermal activation of pile foundation through a proof of concept : in-situ tests
- Objective 3: Evaluation of the effect of temperature and temperaure cycles at the pile-soil interface
- Objective 4: Numerical simulations of energy piles

Research outline

The present work is organized in 5 chapters as follows:

Chapter 1 presents an introduction to the concept of energy piles. This chapter is meant to underline the physical processes and geotechnical challenges involved in the exploitation of energy piles and to identify the different factors involved in the design and execution of energy piles. The literature overview of the state of the art for energy piles is presented for each subsequent chapter.

Chapter 2 focusses on the in-situ behavior of energy piles by presenting the results of two full scale experimental campaigns. After assessing the state of the art, the experimental setup and the results of a first experimental campaign, designed in an academic setting is presented. An energy pile, first loaded to its estimated serviceability limit state was subjected to several heating-cooling cycles over the period of 6 weeks. The pile was then loaded to failure in order to determine the effect of temperature cycles on its bearing capacity. A second full scale experimental campaign focusses on the

long-term behavior of an energy foundation under exploitation conditions. Three piles (two energy piles and a conventional pile) were instrumented during the construction of a new building in a water treatment plant. The energy foundation made out of 100 piles, out of which, 45 energy piles, was designed to cover 100% of the heating and cooling needs of the nearby 340 m2 office building. Seasonal variations in ground temperature and axial strain change were recorded for a year prior to the operation of the ground source heat pump system, and more than one year after the foundation's geothermal activation.

Chapter 3 investigates the thermomechanical behavior of the soil-structure interface in the laboratory. A new advanced interface direct shear test device was used in order to evaluate the effect of temperature and temperature cycles at the soil-structure interface. The device was first validated and then employed for of a series of tests using the most commonly encountered sand types (silica sand and carbonate sand).

Chapter 4 is related to the numerical simulation of energy piles. Thermo-hydro-mechanical simulations of a reduced scale experiment (controlled material and loading conditions) are first presented in order to validate the chosen simulation strategy, and then numerical simulations of a real case study are detailed.

Chapter 5 presents the summary of the work, the main results, conclusions and recommendations for further research.

1. ENERGY PILES OVERVIEW

1.1 Principles of geothermal utilization of foundations

According to the definition given in the Directive 2009/28/EC of the European Parliament, "geothermal energy is the energy stored in the form of heat beneath the surface of the solid Earth". In other words: geothermal energy is the natural heat contained within the Earth. Part of this enormous amount of heat (contained in water or steam transported to the surface) can be extracted and used for various purposes, i.e. to generate electricity, or directly for many applications (GEOCOM 2015) such as energy geostructures.
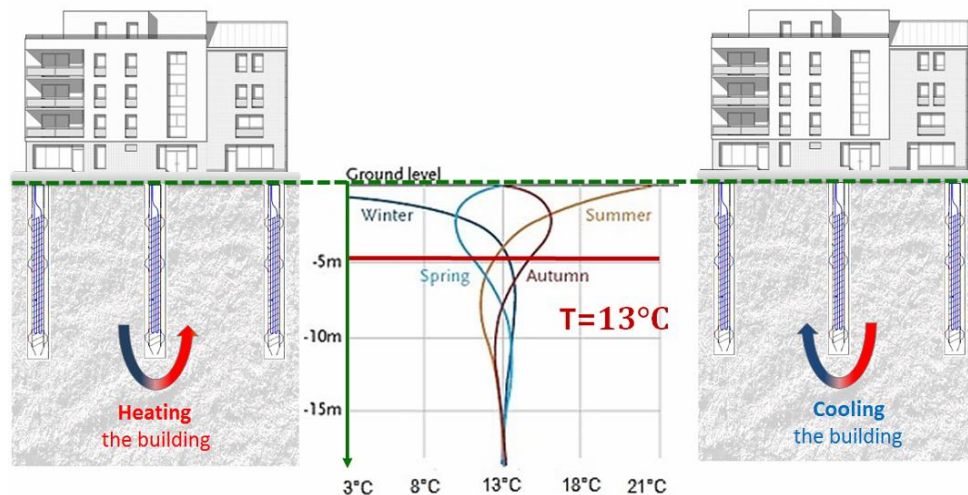
Figure 1-1 Principle of geothermal activation of pile foundations: (a) Heat is extracted from the ground during the cold seasons in order to heat the building, (b) Ground temperature evolution, (c) Heat is injected into the ground during the warm seasons in order to cool the building.

Energy geostructures are systems that couple their load bearing role with the ground heat exchange and are designed to operate within the shallow surface of the Earth (depth < 100m) which is in thermal equilibrium with the atmosphere (Figure 0-1). At this depth the undisturbed soil temperature is close to the annual average air temperature, which depends on the site. Heat can be extracted from the ground at a relatively low temperature (the average undisturbed soil temperature in France is equal to 13°C, Figure 1-1), that is then increased through a heat pump and used in a heating system. For each kWh of heating input, only 0.2 – 0.3 kWh of electricity are required to

operate the system, i.e. the seasonal performance factor amounts to $3.3 - 4.5$ (Sanner et al. 2001). For cooling, the system can be reversed, and the heat from the building can be injected into the ground (Figure 1-1).

Heat pumps are a form of heat engine that uses mechanical work to transfer heat from a low temperature source to a higher temperature sink. Although various forms of thermodynamic cycle can be used to move heat between source and sink, the predominant form is based on the vapour compression cycle in which a refrigerant gas is evaporated, compressed, and condensed in turn to transfer heat. A schematic representation of the principle of functioning of a heat pump is presented in Figure 1-2 a et b. The prime reason for the interest in using heat pumps to provide heating and cooling is that it takes less work to move heat from source to sink than it does to convert primary energy into heat. In other words, the power required is noticeably less than the heating or cooling delivered. This effect is quantified in classical thermodynamics by the coefficient of performance (COP Eq. 1-1).
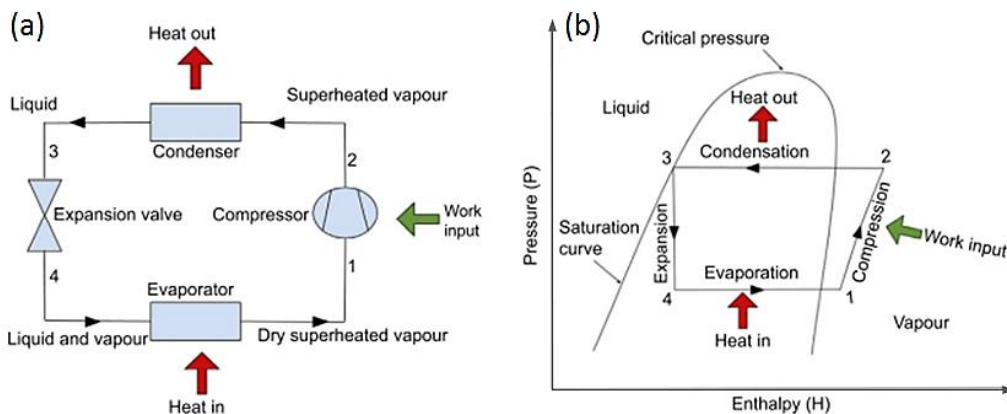
Figure 1-2 (a) Conceptual model of a heat pump, (b) an idealized cycle represented on an enthalpy-pressure diagram (Rees 2016).

$$COP = \frac{energy\ output\ after\ heat\ pump\,[kW]}{energy\ input\ for\ operation\,[kW]}$$

Eq. 1-1

For economic reasons the required value of **COP** should be ≥4 (Brandl 2006). This means that at least 75% of the energy should come from the ground. The **COP** can be different between summer and winter. For example the winter operation **COP** may vary between 3 and 5 while the summer **COP** may vary between 2.5 and 3.5 (Brandl 2006). The efficiency of the heat pump is strongly influenced by the difference between the extracted and the used temperature. A high user temperature and a low extraction temperature in the heat exchanger, reduces the system's efficiency (Figure 1-2 b). This

means that the usable temperature in the secondary circuit should not be higher than 35-40°C and the extraction temperature in the primary circuit should not be lower than 5°C.

Another parameter useful in the evaluation of the performance of ground source heat pumps system is the seasonal performance factor (SPF, Eq. 1-2). This is not useful for rating equipment but is more useful when making comparisons with other technologies or making realistic estimates of running costs or carbon emission savings. It is defined as the ratio of the usable energy output to the energy input required to obtain it. Therefore SPF includes not only the heat pump but also the other energy consuming elements (the circulation pump). Common values for SPF may vary between 3.8 and 4.3 (Brandl 2006; Yavari et al. 2016b).

$$SPF = \frac{usable\ energy\ output\ of\ the\ energy\ system[kW]}{energy\ input\ of\ the\ energy\ system[kW]} \qquad \textit{Eq. 1-2}$$

Experience has shown that systems using ground source heat pumps (GSHP) may save up to two thirds of conventional heating costs. Moreover they represent an effective contribution to environmental protection by providing clean renewable energy.

1.2 Physical processes involved in the exploitation of energy piles

1.2.1 Heat transfer in soil

The soil is a multiphase material with a complex heat transfer mechanism involving conduction, convection, radiation, vaporization and condensation, ion exchange and freezing-thawing process.

As suggested in Figure 1-3 the main heat transfer mechanism in soil is conduction, followed by convection. Heat conduction is also possible if there is a phase change of water (latent heat during vaporization and condensation). Radiation only bares minimum importance (1%) and is restricted to the upper soil layers and freezing-thawing, even though may help transfer heat more efficiently, is to be avoided for thermoactive foundations due to geotechnical reasons.

The total heat transfer, q_{tot} (Eq. 1-3), may be defined as (Rees et al. 2000):

$$q_{tot} = q_{cond} + q_{l,conv} + q_{v,conv} + q_{lat} \qquad \textit{Eq. 1-3}$$

where q_{cond} represents heat transfer by heat conduction, $q_{l,conv}$ represents heat transfer by liquid convection, $q_{v,conv}$ represents heat transfer by vapour convection and q_{lat} represent the latent heat transfer.

The latent heat transfer (Eq. 1-4) occurs as a result of change phase of pore water (vaporisation) and depends only on the quantity of vapour transfer occurring in

the soil pores. It increases with decreasing water content and it can be expressed as follows:

$$q_{lat} = L_0 \rho_l v_v \qquad \qquad Eq.\ 1\text{-}4$$

where L_0 is the latent vaporisation heat, ρ_l is the density of water and v_v is the vapour velocity.
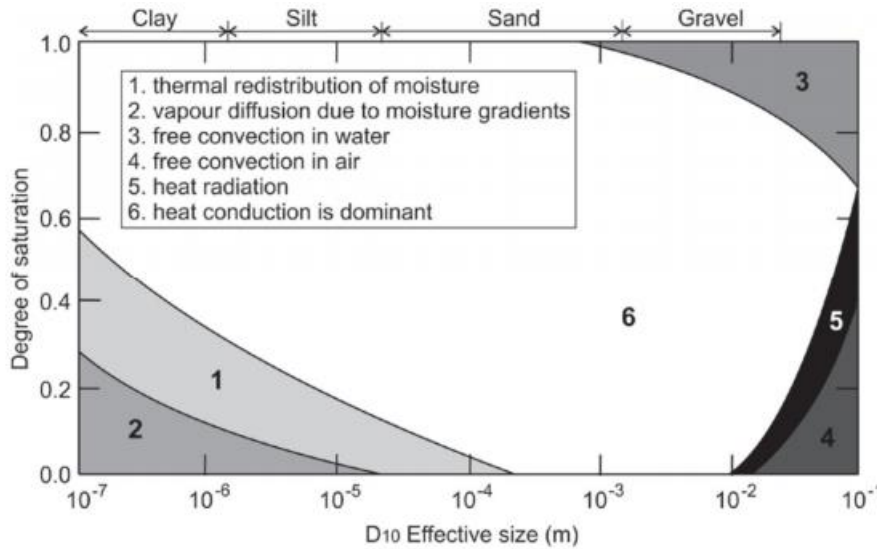
Figure 1-3 Predominant heat transfer mechanism in soil depending on the degree of saturation and grain size (after Farouki 1981 and Loveridge 2012).

Heat convection occurs between thermo-dynamic systems that move relative to each other. In soils, the solid phase is static: hence convection can occur only in the water or (pore) gas phase. Heat transfer by fluid convection, $q_{l,conv}$ (Eq. 1-5), and heat transfer for vapour (pore gas), $q_{v,conv}$ (Eq. 1-6), may be defined as follows:

$$q_{l,conv} = c_l \rho_l v_l \Delta T \qquad \qquad Eq.\ 1\text{-}5$$

where c_l is the specific heat capacity of pore water , ρ_l is the density of water, v_l is the water velocity and ΔT is the change in temperature.

$$q_{v,conv} = c_v \rho_v v_v \Delta T \qquad \qquad Eq.\ 1\text{-}6$$

where c_v is the specific heat capacity of soil vapour , ρ_w is the density of soil vapour, v_v is the vapour velocity and ΔT is the change in temperature.

Heat conduction (Eq. 1-7) is a process whereby heat is transferred from one region of the medium to another, without visible motion in the medium. The heat energy is passed from molecule to molecule. According to Fourier's law, the heat flux for a heat volume Q through an arbitrary area A, during time t, that is, the heat flux per unit area, q_{cond}, generated by conduction is defined as:

$$q_{cond} = \frac{Q}{At} = -\lambda \nabla T \qquad \qquad Eq.\ 1\text{-}7$$

where λ is the thermal conductivity of the medium, ∇ is the gradient operator and T is the temperature.

Moisture migration produces changes in soil thermal properties, especially in unsaturated soils (Farouki 1981). Evaporation of water in the soil induces temperature gradients and the water vapour can move through the pores towards the lower vapour pressure. If the temperature is lower in the new location, condensation occurs releasing heat and changing the water content of the soil. This moisture migration affects the thermal properties of the soil by changing the degree of saturation but also contributing to the heat transfer process. The process may become important in soils with high porosity and high temperature differences.

Correctly assessing the thermal properties of soil is of great importance in designing energy geostructures. These thermal properties may vary with phase composition, water content or dry density. According to (Andersland and Ladanyi 2013) the basic thermal properties are:

- Thermal conductivity: λ [W/mK] is the ability of a material to transport thermal energy. It is defined as the amount of heat Q (Eq. 1-8) passing through a unit area (A) of the soil in unit time under a temperature gradient applied in the direction of the heat flow:

$$Q = \lambda A \frac{dT}{dx}$$

Eq. 1-8

- Heat capacity: c [J/m^3K] (Eq. 1-9) is the ability of a material to store thermal energy. It is defined as the quantity of heat necessary to increase the temperature by 1K. It does not depend on microstructure so in most cases, it is considered acceptable to calculate the heat capacity of soil from the values of the heat capacity of its components:

$$c = c_s x_s + c_w x_w + c_a x_a$$

Eq. 1-9

where : $x_s = 1 - n$ is the percentage of solid phase in the soil composition, n is the soil's porosity, $x_w = nS$ is the percentage of the pore water in the soil composition, S is the degree of saturation and $x_a = n(1 - S)$ is the pore air percentage in the soil composition

- Thermal diffusivity: α [m^2/s] (Eq. 1-10) is the ability of a material to level temperature differences and reach thermal balance in an unsteady state:

$$\alpha = \frac{\lambda}{c\rho}$$

Eq. 1-10

where λ is the thermal conductivity, c is the heat capacity and ρ is the soil density.

A list of typical values for different soils thermal properties is provided in Table 1-1.

Material(20°C)	Heat Capacity c [kJ/kgK]	Thermal conductivity λ [W/mK]	Thermal diffusivity α [m²/s]
Air	1.0024	0.024	22.07 E-6
Water	4.186	0.6	0.143 E-6
Clay	0.92	1.1(dry)/4(saturated)	200-340
Silt	0.8	1.67	380
Sand	0.8	0.15-0.25(dry)/2-4(saturated)	380

Table 1-1Thermal properties of different materials (after Andersland and Ladanyi 2013)

In the long term, consolidation or shrinkage processes of soil (under external loads, or self-weight or heat extraction) may play a role on its thermal properties due to the volume ratios change (Brandl 2006). The overall thermal capacity increases with the water content and decreases in the case of freezing. The most important thermal soil parameter is the thermal conductivity. For preliminary design of complex energy foundations or for the detailed design of simple projects, the value of λ can be deduced with sufficient accuracy from diagrams considering water content, saturation density and texture of the soil (SIA 2005).

However for more complex projects the thermal conductivity should be determined from laboratory and/or field tests. The most common field test is the thermal response test, which involves applying a finite amount of heat energy into a closed loop borehole over a certain period of time (up to several days), while monitoring the rate at which heat dissipates into the surrounding ground. Appropriate analysis of the test data allows accurate values of ground thermal properties. The advantage of this test is that it can be performed using one of the installed energy piles but the disadvantage is that this test is time consuming and expensive. In the laboratory both steady state methods and transient methods can be applied. The steady state methods, like the thermal cell test, imply applying a one directional heat flow to a specimen and measuring the power input and the temperature difference across it when a steady state is reached (Low et al. 2013). The thermal conductivity is then calculated directly using Fourier's Law of heat conduction. Transient methods such as the needle probe test involve applying heat to the specimen and monitoring temperature changes over time and using the transient data to determine the thermal conductivity.

The specific heat capacity can be determined in the laboratory by mixing water and soil of different temperatures. If the total energy of both components remains constant and the specific heat capacity of one component is known (for example the water) then the specific heat capacity of the soil can be achieved.

1.2.2 Heat transfer in concrete energy piles

The temperature difference between the ground, the pile and the heat carrier fluid passing through the geothermal installation, produces the heat transfer in the geothermal system. The mechanisms involved in this process are resumed in Figure 1-4 a et b, i.e. convective heat flow between the heat carrier fluid and pipe, conductive heat flow in the pipe's wall, conductive heat flow in the concrete pile, conductive heat flow in the soil and convective heat flow in the soil if the groundwater flow speed is higher than 0.5-1.0 m/day (Loveridge and Powrie 2012).
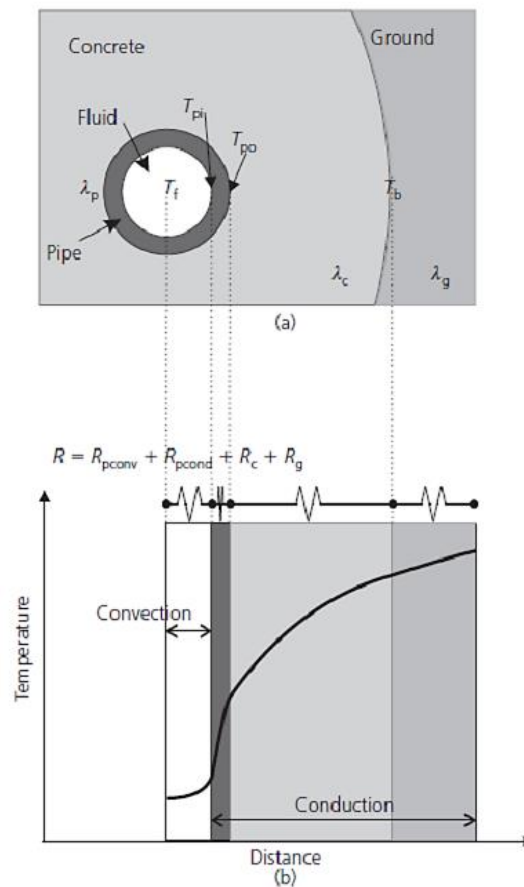
Figure 1-4 Heat transfer mechanisms in energy piles: (a) plane view of the energy pile and the surrounding soil, (b) lateral view of the energy pile and the surrounding soil (Loveridge and Powrie 2012).

According to Lee et al. (2009) the total usable heat extracted using energy piles can be calculated using Eq. 1-11:

$$Q_{tot} = Q_{in} - Q_{out} = mc_{fluid}(T_{in} - T_{tot}) \qquad \textit{Eq. 1-11}$$

where: m is the mass flux density of the circulating fluid, c_{fluid} is the heat capacity of the circulating fluid, Q is the total heat extracted, T_{in} is the inlet temperature and T_{out} is the outlet temperature.

Conventionally, in the design of energy piles, instantaneous steady state is assumed as far as internal heat transfer between the thermal fluid and the exterior surface of the concrete is concerned. The temperature change between the fluid in the pipes and the edge of the heat exchanger (ΔT) can then be calculated on the basis of the resistance of the heat exchanger, R_b as in Eq. 1-12:

$$R_b = \frac{T_s - T_f}{q}$$

<div align="right">Eq. 1-12</div>

where: T_s is the soil-pile interface temperature, T_f is the heat carrier fluid temperature and q is the induced heat flow per meter of GSHP exchanger.

As it can be noticed from Eq. 1-12, the greater the value of R_b, the greater the temperature difference between the heat carrier fluid and the soil and consequently the lower the efficiency of the system.

The value of the thermal resistance depends upon the number of pipes, their disposition, the concrete cover thickness, as well as the thermal conductivity of the concrete and the thermal properties of the heat carrier fluid. A general decomposition of R_b (Eq. 1-13) is based on resistances in series (Loveridge et al. 2014) as follows:

$$R_b = R_{pconv} + R_{pcond} + R_c$$

<div align="right">Eq. 1-13</div>

where: R_{pconv} (Eq. 1-14) accounts for the forced convection transfer between the pipe wall and the heat carrier fluid, R_{pcond} (Eq. 1-15) for the thermal resistance of the pipe wall and R_c (Eq. 1-16) for the thermal resistance of the concrete and the cross-section geometry. They can be calculated as follows:

$$R_{pcond} = \frac{ln(r_{out}/r_{in})}{2N\pi\lambda_p}$$

<div align="right">Eq. 1-14</div>

$$R_{pconv} = \frac{1}{2N\pi r_{in}h_i}$$

<div align="right">Eq. 1-15</div>

$$R_c = \frac{1}{\lambda_c S_c}$$

<div align="right">Eq. 1-16</div>

where: r_{out} is the outer radius of the pipe, r_{in} is the inner diameter of the pipe, N is the number of pipes per cross-section of GSHP system, λ_p is the thermal conductivity of the pipe wall material, h_i is the heat transfer coefficient, λ_c is the thermal conductivity of the concrete and S_c is the shape factor accounting for the number of pipes and their position in the pile's cross-section.

It should be noted that the concrete cover is usually dictated by the structural design (i.e. reinforcement cages design) and because it is important to avoid thermal interactions between the cold and hot pipes, the value of the shape factor can only be partially optimized.

Loveridge et al. (2014) have provided charts of thermal resistance for piles. These charts suggest that the larger the pile diameter, the lower its thermal resistance, the thinner the concrete cover, the better the thermal contact between the pipes and the soil and that an optimum number of pipes with respect to the pile diameter exists (increasing too much the number of pipes will yield more thermal interactions between the cold and hot pipes thus reducing the efficiency of the system). Although these charts may offer a first insight in the characteristic configurations appropriate for an energy pile, more advanced tools are required for the design of a whole system and for assessing its long term behaviour.

1.3 Geotechnical challenges involved in the exploitation of energy piles

1.3.1 Temperature induced changes in soil

Safely transferring the loads from the structure to the ground remains the main role of energy geostructures thus for safety reasons the temperature induced changes in the soil must be considered.

Thermal process in the ground induces water migration towards the colder regions (Brandl 2006). In fine grained soils this may cause shrinkage in the warm zones and expansion in the cold ones. Also, the thermal expansion of pore water increases the pore water pressure and consequently decreases the effective stress of the soil. Furthermore, increasing the temperature reduces the internal viscosity and hence the shear resistance. The presence of organic constituents increases the temperature sensitivity of the soils (especially of clay's). Field tests show that properly designed and operated energy foundations don't affect the load transfer (Bourne-Webb et al. 2009; Murphy and McCartney 2015; Faizal et al. 2018). Commonly the interactions are negligible but they need to be considered for buildings extremely sensitive to differential settlements.

Lowering the groundwater temperature translates in the increase of its viscosity and a decrease of its hydraulic conductivity, which leads to lower flow velocities and to smaller flow gradients of the groundwater (Brandl 2006). However, for the range of temperatures used for geothermal exploitation in the case of energy geostructures (5°C-

30°C), these effects are negligible (SIA 2005). A more important factor to be considered in this regard is related to the conservation of the thermal balance of the soil for the cases where the hydraulic gradient is smaller than 1m/day and the heat transport when the hydraulic gradient is superior to this value (SIA 2005).

Excessive cooling of the groundwater (due to excessive energy extraction) may increase the pH value and reduce the calcium solubility, which favours the clogging of pores. On the other hand the solubility of gaseous substances such as CO_2 increases increasing the hardness of the groundwater (Brandl 2006).

The temperature is a very important environmental factor for the microorganisms in the groundwater (Brandl 2006). Many of them can exist only within a temperature range. In particular, the activity of bacteria-consuming microorganisms drops significantly below 10°C and the proliferation of certain bacteria increases above 35 °C (Fakharian and Evgin 1997; Brandl 2006).

1.3.2 Temperature induced changes in the pile

During heating/cooling cycles, thermal changes produce volume changes in the pile and in the soil around it. Amatya et al. (2012) show that thermal expansion induces changes in the static behaviour of the energy foundations after applying several cyclic loads. In order to avoid problems due the temperature induced changes in energy geostructures, it is thus very important to understand the response mechanism.

Assuming the simplified case of a homogenous, linear elastic, unrestrained pile, it is expected to expand during heating and contract during cooling causing additional axial tensile stress and changing the pile soil-interaction. The axial strain of an unconstrained pile (Eq. 1-17) depends only on the thermal expansion coefficient of each material and the temperature variation (Figure 1-5 (a)):

$$\varepsilon_{obs} = \varepsilon_{Free} = \alpha_c \Delta T \qquad\qquad\qquad Eq.\ 1\text{-}17$$

where ε_{obs} is the observed (measured) axial strain, ε_{Free} is the free axial strain of the pile under thermal loading, α_c is the coefficient of thermal expansion of concrete , ΔT is the temperature change.

The stresses in the pile should always remain under the allowable limit. An extreme case for the evaluation of the additional stress that may develop in an energy pile consists in considering a fully restrained pile (Figure 1-5 (b), Eq. 1-18):

$$\sigma_T = \varepsilon_b E \qquad\qquad\qquad Eq.\ 1\text{-}18$$

where σ_T is the additional thermal stress due to thermal loading for a fully constrained pile, ε_b is the blocked axial strain and E is Young modulus.

In reality the boundary conditions may be somewhere in between fully restrained and unrestrained thus the axial strain due to thermal loading does not occur under free expansion conditions and thermally induced stresses arise along the foundation. This translates into the fact that although free expansion condition represents an upper limit for the magnitude of the pile deformation, the observed deformation may be significantly smaller and the remaining blocked deformation converts into thermal axial stress (Eq. 1-19).
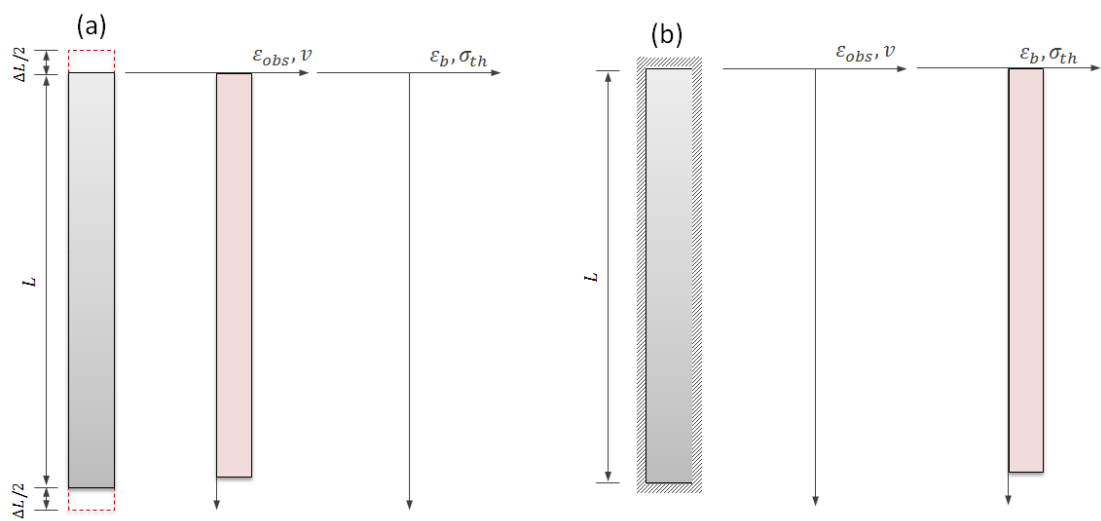
Figure 1-5 Thermal response of a free and a completely restrained pile: (a) heating, free pile, (b) heating, restrained pile (after Bourne-Webb et al. 2013).
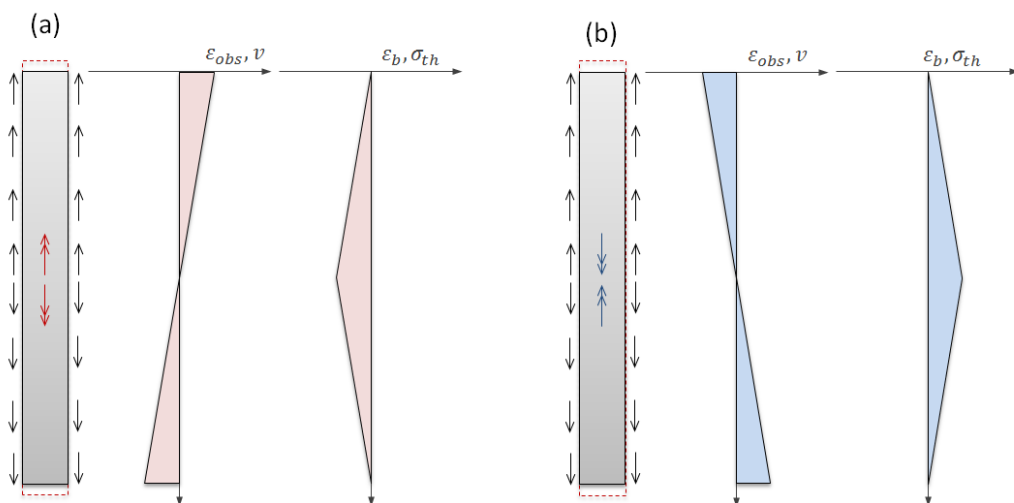
Figure 1-6 Effect of soil restraint on the response of energy piles during thermal loading: (a) heating, (b) cooling (after Bourne-Webb et al. 2013).

To illustrate this, the response to heating and cooling of a floating pile without mechanical loading is considered (Figure 1-6). As the soil strength and stiffness increase the restraint mobilised at the pile-soil interface increases. During heating, expansive strains at the mid –length of the pile will be more restrained than towards its extremities resulting in the development of compressive axial stress (Figure 1-6 (a)). Soil restraint during cooling leads to suppressed contractive strain, and thus tensile load will develop as soil resistance increases (Figure 1-6 (a), Eq. 1-19).

$$\varepsilon_{Free} = \varepsilon_{obs} + \varepsilon_b$$ <div align="right">*Eq. 1-19*</div>

where ε_{Free} is the free axial strain of an energy pile, ε_{obs} is the observed (measured) axial strain of the pile under thermal loading and ε_b is the blocked axial strain (due to restraints) of the pile under thermal loading.

1.4 Design and execution of energy piles

1.4.1 Short pile foundations overview

Foundations provide support for structures, transferring their load to layers of soil or rock that have sufficient bearing capacity and suitable settlement characteristics. There are a very wide range of foundation types available, suitable for different applications, depending on considerations, such as the supported load, ground conditions, cost, proximity to other structures etc. Very broadly foundations can be set in two categories: shallow and deep foundations respectively. Shallow foundations are commonly used when the structure loads are relatively low compared to the soil's bearing capacity. Deep foundations on the other hand are used when the soil surface's bearing capacity is insufficient to support the loads transferred by the superstructure and thus they are transferred to deeper layers with better mechanical properties.

Pile foundations are a type of deep foundations, formed by long slender columnar elements typically made from steel or reinforced concrete, or sometimes timber, having the distinct property of its depth being at least three times larger than its breath (Atkinson, 2007). This type of deep foundations are principally used to transfer the loads from superstructures, through weak, compressible strata or water onto stronger, more compact, less compressible and stiffer soil or rock at depth, increasing the effective size of a foundation and resisting horizontal loads.

Piles may be classified by their basic design function as end-bearing, friction or a combination. End-bearing piles (Figure 1-7 a) develop most of their capacity at the toe of the pile, bearing on a hard layer. The pile transmits load direct to firm strata, and also

receives lateral restraint from subsoil. Friction (or floating, Figure 1-7 b) piles develop most of the pile-bearing capacity by shear stresses along the sides of the pile, and are suitable where harder layers are too deep. The pile transmits the load to surrounding soil by friction between the surface of the pile and soil , which in effect lowers the bulb of pressure. Many piles exhibit though a combination of the two load transfer mechanisms (Figure 1-7 c).

By their method of construction piles may be divided into displacement (driven) or replacement (bored) piles. Driven piles are normally made from pre-cast concrete which is then hammered into the ground once on site. Bored piles are cast in situ; the soil is bored out of the ground and then the concrete is poured into the hole. Alternatively, boring of the soil and pouring of the concrete can take place simultaneously, in which case the piles are called continuous fight auger piles (O'Sullivan, 2010).
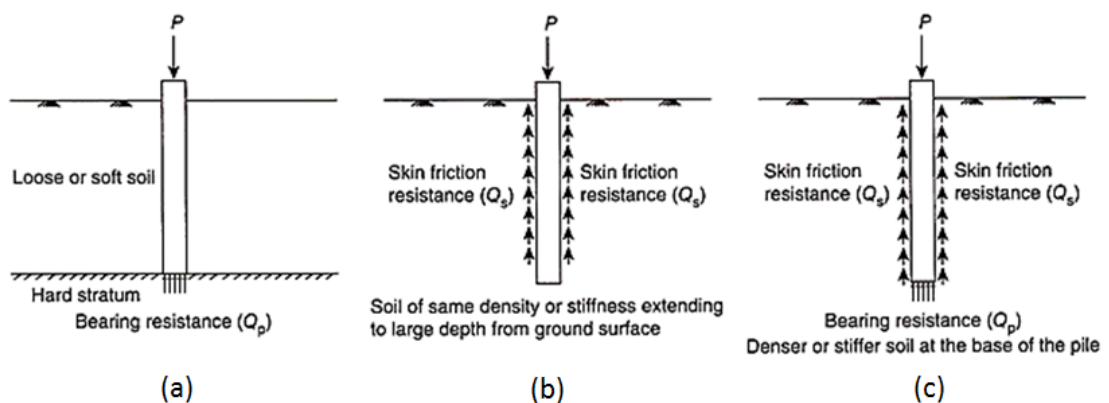
Figure 1-7 Types of piles based on the method of load transfer: (a) end-bearing pile, (b) friction (floating) pile and (c) bearing-cum-friction pile.

The choice of pile used depends on the location and type of structure, the ground conditions, durability of the materials in the environment and cost. Most piles use some end bearing and some friction, in order to resist the action of loads. Driven piles are useful in offshore applications, are stable in soft squeezing soils, and can densify loose soil. However, bored piles are more popular in urban areas as there is minimal vibration, they can be used where headroom is limited, there is no risk of heave, and it is easy to vary their length (O'Sullivan, 2010).

Geothermal piles are a relatively new type of pile foundations combined with closed-loop ground source heat pump systems. Their purpose is to provide support to the building, as well as acting as a heat source and a heat sink. In effect, the thermal mass of the ground enables the building to store unwanted heat from cooling systems and allows heat pumps to warm the building in winter (Brandl 2006).

1.4.2 Energy piles design

In recent years, design and execution recommendations have been proposed in some European countries (SIA 2005; GHSP 2012; CFMS-SYNTEC-SOFFONS-FNTP 2017) but an unified framework for the thermomechanical design of such foundations is still pending (Rotta Loria 2018). In any design scheme, though, two main issues need to be systematically considered: behaviour when in service and failure scenarios.

None of the existing standards and guidance documents offer any indication on how the thermal performance of an operating system should be measured and what failure criteria may be appropriate. In order to tackle this problem, Bourne-Webb et al. (2016) suggest a number of parameters to be accounted for in such a performance evaluation, listed in Table 1-2.

Regardless of the heat exchanger role of energy piles, their primary function remains to safely transfer loads without unacceptable movement or damage to the superstructure or neighbouring structures. In other words, the geotechnical energy pile design should follow the same reasoning as a classical pile design (i.e. SLS and ULS conditions) while incorporating an additional type of load, namely the thermal loading.

Energy delivered	An EGS scheme will be designed to deliver a certain proportion of the overlying buildings heating and cooling requirements and if this is not achieved then it may be considered to have failed. The consequences of failure will be greatest when no backup system is available. A suggested recommended approach would be to consider a 10% margin between required and expected energy supply as a starting value and then to revise it on a project-by-project basis depending on the specific conditions that occur.
Efficiency of system	The seasonal performance factor (SPF) gives the measured efficiency of an installed heat pump system. It is the ratio of the heat delivered for space heating and hot water and the electricity used to run the system. Under the EU Renewable Energy Sources Directive [122], heat pumps are considered renewable if their SPF is greater than 2.5. This could also be a convenient measure of acceptable serviceability performance of EGS.
System temperatures	More work is required to establish guidance on operational temperature limits for EGS. Current practice tends to recommend that the lower limit on the heat transfer fluid temperature in BHE & EGS should be kept above freezing with a 2 °C margin of error [117,118,123]. This is to ensure the ground does not freeze. It has been shown both theoretically and in practice, that for large diameter piles, temperatures lower than 0 °C can be sustained within the heat transfer fluid for short periods and have no detrimental effects on the ground [71,124]. Similar conclusions were reached by [6] but do not seem to have been acted upon in general practice. Due to the impact of high temperatures on pump efficiency and thus SPF, the circulating fluid is usually kept below 40 °C, although values as high as 60 °C are used [117].
Environmental	The development of SGE and EGS systems in the future will increasingly need to consider interactions with adjacent systems and/or the potential for heat to propagate outside site boundaries and thus, compromise future developments. Currently, there is no guidance or regulation relating to this issue.

Table 1-2 Thermal performance criteria (after Bourne-Webb et al. 2016)

1.4.2.1 Classical pile design

Foundation design consists of selecting and proportioning foundations in such a way that limit states (Ultimate Limit State (ULS), Serviceability Limit State (SLS)) are prevented. The design must satisfy the requirements of the building code being in effect, specifically the Eurocode 7 and its National Annexes in European Union countries.

EN 1997-1 states that the design of piles shall be based on one of the following approaches:

- The results of static load tests, which have been demonstrated, by means of calculations or otherwise, to be consistent with other relevant experience

- Empirical or analytical calculation methods whose validity has been demonstrated by static load tests in comparable situations

- The results of dynamic load tests whose validity has been demonstrated by static load tests in comparable situations

- The observed performance of a comparable pile foundation, provided that this approach is supported by the results of site investigation and ground testing

  The pile foundations need to be guaranteed with respect to:

- ULS for a single pile and for the foundation as a whole, which means that an adequate safty margin against both structura and geotechnical failure must be ensured;

- SLS which means that the absolute differential foundation settlement under working conditions must be within acceptable limits so that the comfort of the building is preserved.

The equilibrium equation to be satisfied in the ultimate limit state design of axially loaded piles in compression is presented in Eq. 1-20:

$$F_{c;d} \leq R_{c;d} \qquad \qquad \text{Eq. 1-20}$$

where $F_{c;d}$ is the design axial compression load and $R_{c;d}$ is the pile compressive design resistance.

The design axial compressive load $F_{c;d}$ is obtained by multiplying the representative permanent and variable loads, G and Q by their corresponding safety factors γ_G and γ_Q, as in Eq. 1-21:

$$F_{c;d} = \gamma_f F_{rep} = \gamma_G G_{rep} + \gamma_Q Q_{rep} \qquad \qquad \text{Eq. 1-21}$$

The two sets of recommended partial factors on actions and the effects of actions provided in Annex A of EN 1997-1, reproduced in Table 1-3.

Action		Symbole	Ensemble	
			A1	A2
Permanent	Unfavorable	γ_G	1.35	1.0
	Favorable		1.0	1.0
Variable	Unfavorable	γ_Q	1.5	1.3
	Favorable		0	0

Table 1-3 Recommended safety factors on actions (EN 1997-1)

$$F_{rep} = \psi F_k \qquad\qquad Eq.\ 1\text{-}22$$

where F_{rep} is the relevant representative value of the action, F_k is the characteristic value of the action, γ_f is the partial factor for the action which takes account of the possibility of unfavourable deviations of the action values from the representative value and ψ is equal to 1.00 or ψ_0 the factor for combination value of a variable action or ψ_1 the factor for frequent value of a variable action or ψ_2 the factor for quasi-permanent value of a variable action.

For a specific load case the design values of the effects of actions (E_d) can be expressed in general terms as in Eq. 1-23:

$$E_d = \gamma_{Sd} E\{\gamma_{f,i} F_{rep,i}; a_d\} \qquad\qquad Eq.\ 1\text{-}23$$

where γ_{Sd} is a partial factor considering uncertainties in modelling the effect of actions and in some cases, modelling the actions, a_d is the design value of the geometrical data.

Combination	Permanent actions G_d		Prestress	Variable actions Q_d	
	Unfavourable	Favourable		Leading	Others
Characteristic	$G_{k,j,sup}$	$G_{k,j,inf}$	P	$Q_{k,1}$	$\Psi_{0,i} Q_{k,i}$
Frequent	$G_{k,j,sup}$	$G_{k,j,inf}$	P	$\Psi_{1,1} Q_{k,1}$	$\Psi_{2,i} Q_{k,i}$
Quasi-permanent	$G_{k,j,sup}$	$G_{k,j,inf}$	P	$\Psi_{2,1} Q_{k,1}$	$\Psi_{2,i} Q_{k,i}$

Table 1-4 Recommended safety factors on actions (EN 1997-1).

The design axial compressive load shall be determined for all the following design situations:

- Persistent design situations, which refer to the conditions of normal use
- Transient design situations, which refer to temporary conditions applicable to the structure
- Accidental design situations which refer to the exceptional conditions applicable to the structure or to its exposure
- Seismic design situations, which refer to conditions applicable to the structure when subjected to seismic events.

The pile characteristic compressive resistance $R_{c;k}$ may be determined according to the Eurocode 7 either directly from static load tests, by calculation from profiles of ground test results or by calculation from ground parameters.

The design compressive resistance of a pile $R_{c;d}$ may be obtained either by treating the pile resistance as a total resistance (Eq. 1-24) or by separating it into base and shaft resistance (Eq. 1-25).

$$R_{c;d} = R_{c;k}/\gamma_t \qquad\qquad\qquad\qquad\qquad Eq. \ 1\text{-}24$$

$$R_{c;d} = R_{b;k}/\gamma_b + R_{s;k}/\gamma_s \qquad\qquad\qquad\qquad\qquad Eq. \ 1\text{-}25$$

For the serviceability limit state, the foundation displacements shall be assessed and checked against the rudiments given. This involves absolute settlements, tilt movements, and differential displacements.

There exist four approaches which can be adopted to predict the displacement of a single pile (Di Donna 2014):

- Load settlement curves determined through in-situ load tests at the reak scale
- Finite element analysis
- Load transfer curves method
- Analytical approximated solutions

Action	Ψ_0	Ψ_1	Ψ_2
Imposed loads in buildings, category (EN 1991-1-1):			
Category A: domestic, residential areas	0.7	0.5	0.3
Category B: office areas	0.7	0.5	0.3
Category C: congregation areas	0.7	0.7	0.6
Category D: shopping areas	0.7	0.7	0.6
Category E: storage areas	1.0	0.9	0.8
Category F: traffic areas (vehicle weight ≤30kN)	0.7	0.7	0.6
Category G: traffic area (30kN< vehicle weight≤160kN)	0.7	0.5	0.3
Category H: roofs	0.0	0.0	0.0
Snow loads on buildings (EN 1991-1-4)*			
Finland, Iceland, Norway, Sweden	0.7	0.5	0.2
Remainder of CEN Member States, for sites located at altitude H>1000m a.s.l.	0.7	0.5	0.2
Remainder of CEN Member States, for sites located at altitude H≤1000m a.s.l.	0.5	0.2	0.0
Wind loads on buildings (EN 1991-1-4)	0.6	0.2	0.0
Temperature (non-fire) in buildings (EN 1991-1-5)	0.6	0.5	0.0
NOTE: The Ψ values may be set by the National Annex * For countries not mentioned above, see relevant local conditions			

Table 1-5 Recommended safety factors on actions (EN 1997-1).

Resistance	γ_R	Driven Piles				Bored piles				CFA Piles			
		R1	R2	R3	R4	R1	R2	R3	R4	R1	R2	R3	R4
Base	γ_b	1.0	1.1	1.0	1.3	1.25	1.1	1.0	1.6	1.1	1.1	1.0	1.45
Shaft	γ_s	1.0	1.1	1.0	1.3	1.0	1.1	1.0	1.3	1.0	1.1	1.0	1.3
Total	γ_t	1.0	1.1	1.0	1.3	1.15	1.1	1.0	1.5	1.1	1.1	1.0	1.4
Shaft in tension	γ_{st}	1.25	1.15	1.1	1.6	1.25	1.15	1.1	1.6	1.25	1.15	1.1	1.6

Table 1-6Partial safety factors on resistance (EN 1997-1).

1.4.2.2 Energy pile design

Thermal loads due to the geothermal activation of a pile foundation can be considered variable static loads. The temperature change applied to energy piles can defined with reference to the temperature inputs involved in the building energy design, the associated thermal power for heating and cooling, the operation time and the thermal properties of the soil and of the ground. The resulting temperature changes are nominal values ΔT_k (Rotta Loria 2018). These values are likely between $\pm 10°C$ (Vasilescu et al. 2019).

To appropriately consider the influence of thermal loads in the loads combinations, the factor for combination value of a variable action ψ_0, the factor for frequent value of a variable action ψ_1 and the factor for quasi-permanent value of a variable action ψ_2 were chosen equal to 0.6, 0.5 and 0.2 respectively according to the recommendations provided by CFMS-SYNTEC-SOFFONS-FNTP (2017).
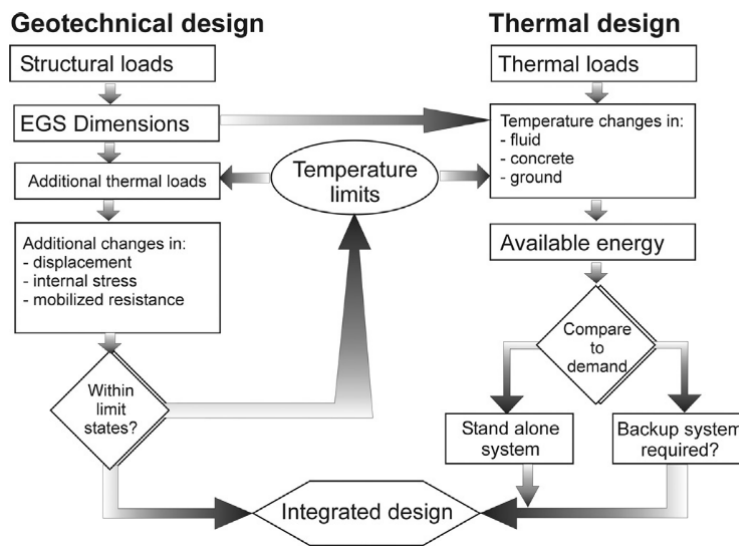
Figure 1-8 The interactions between the geotechnical and thermal design processes (Bourne-Webb et al. 2016).

When considering the combinations of loads it should be accounted for the fact that for heating, it is not known a priori whether the involved effects make them the dominant load with respect to the other variable loads (Rotta Loria 2018). In consequence both cases when the thermal load is dominant and when one of the other variable loads is dominant should be considered

Any design also needs to consider the interactions between the geotechnical and thermal analysis as suggested by Bourne-Webb et al. (2016) and illustrated in Figure 1-8. In the simplest case, temperature limits are applied to both the geotechnical and

thermal design streams. However, these limits must first be agreed upon and may also require refinement during the design process.

1.4.2.3 Energy piles execution

Structural piles are turned into heat exchangers by adding one or more loops of high-density polyethylene plastic pipes down their length. The geothermal loops are fixed on the reinforcement cages and then fitted with a locking valve and the manometer at the inlet and outlet ends. The pipes are filled with a fluid (gas or water) and pressurized for a first integrity test and to prevent collapse due to the fluid concrete. This pressure is ideally maintained during the entire construction period or at least during the concrete hardening.
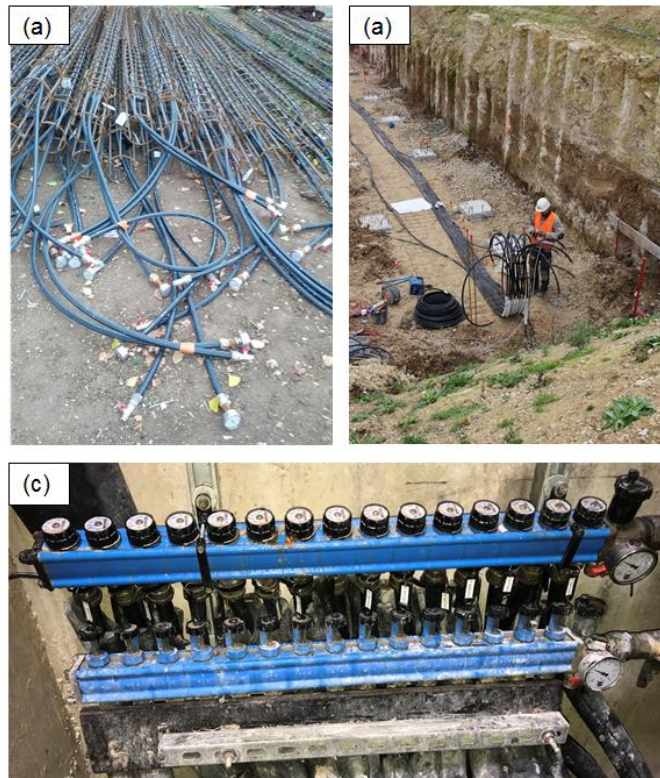
Figure 1-9 Geothermal loops installation: (a) geothermal loops fixed on reinforcement cages, (b) Horizontal connections installation, (c) The manifold connecting all the geothermal loops to the GSHP.

The loops are then lowered in the bored hole and concrete is poured using a tremie pipe for drilled piles or they are directly inserted in the fresh concrete in the case of CFA piles (Figure 1-9). Another integrity test is performed after concreting, after the installation of the horizontal connections to the heat pump and before starting the geothermal exploitation of the foundation.

2. IN SITU STUDY OF THERMOMECHANICAL BEHAVIOUR OF ENERGY PILES

2.1 Introduction

The objective of this chapter is to identify and quantify the principal parameters involved in the design of energy pile foundations that are impacted by the changes in temperature associated with the geothermal activation of the foundation. For this purpose, the results from two full scale experimental campaigns are analysed hereafter.

In the first case, an academic setup, with controlled loading conditions was studied. Two 12-m long concrete piles with a nominal diameter of 0.42 m were installed in a site including layers of clay and marl on the grounds of Ecole de Ponts Paris Tech, close to Paris. Several years after their installation, one of the two piles was first loaded to a pile head axial force of 600 kN, which corresponds to the assumed serviceability capacity. Afterward, while the pile head load was maintained constant, three thermal cycles were applied to the pile to simulate the seasonal thermal loading, using a refrigerated and heating circulator. The pile temperature, from its initial value (12.5 °C), varied between 4 °C and 25 °C.

Although the imposed temperature gradient for this test is similar to the annual heating/cooling average temperature variation observed in energy foundations of a typical building operation (McCartney and Murphy 2017), the functioning of a refrigerated and heating circulator is different from that of a heat pump commonly used in energy geostructures. Therefore, a second case study focusses on understanding the behaviour of energy piles in real exploitation conditions. Two energy piles and a conventional pile with the length of 9m and the diameter of 0.42m, were instrumented with vibrating wire sensors equipped with thermistors during the construction of the pre-treatment building of the Sept Sorts water treatment plant in Seine-et-Marne department, in France. Their behaviour under exploitation conditions was recorded for both conventional conditions and after the geothermal activation of the foundation.

2.2 Background

The knowledge on energy piles is progressively growing thanks to the increasing number of full-scale experiments (Laloui et al. 2003; Brandl 2006; Bourne-Webb et al. 2009; Martin et al. 2010; Singh et al. 2011; McCartney and Murphy 2012a; Akrouch et al. 2014; McCartney et al. 2015; Sutman et al. 2015; You et al. 2016; Sung et al. 2018). These studies point out the fact that using piles as heat exchangers induces additional deformations and stresses in the foundation, depending on the amplitude of the thermal load, the boundary conditions, and hydro-mechanical soil behaviour.
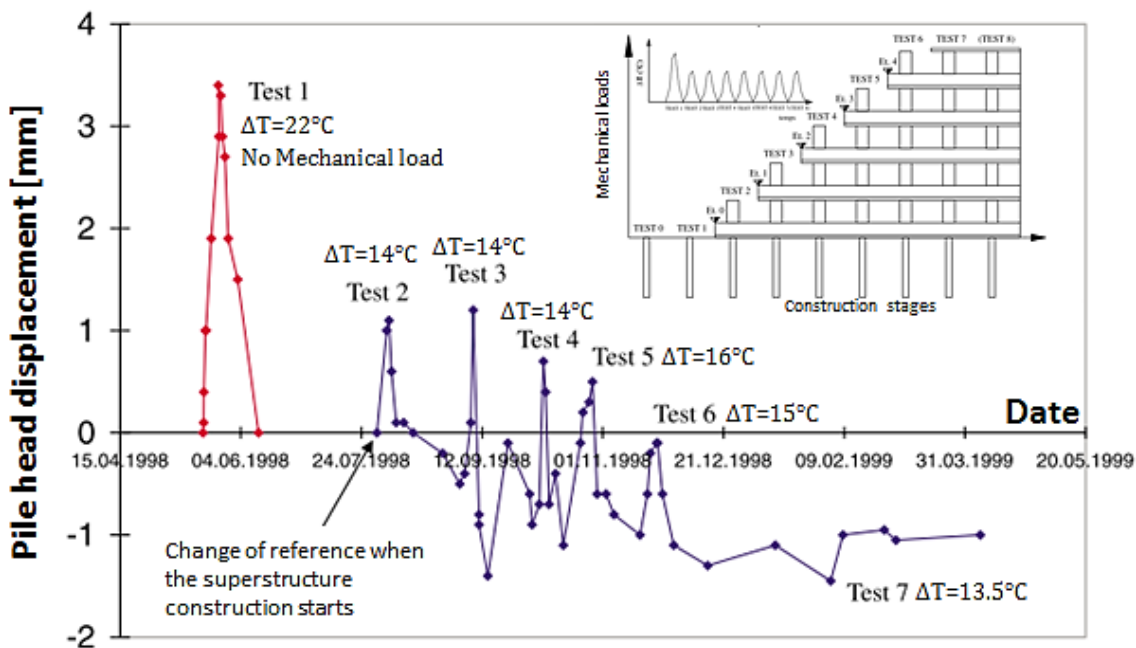
Figure 2-1 Pile head displacement due to imposed temperature changes during the construction of a four story building at the Swiss Federal Institute of Technology in Lausanne, Switzerland (Laloui et al. 2003).

Based on experimental results Amatya et al. (2012) proposed a descriptive framework for explaining the response of thermomechanically loaded piles. When a pile is heated, it expands, but it is not able to expand freely due to the mobilization of side restraint at pile-soil interface and any end restraints either at the pile head or toe (Figure 2-1). As shown by the evolution of the strain profiles during heating and cooling tests performed at Lambeth College (Bourne-Webb et al. 2009) a floating pile exhibits no axial stress at the pile toe (Figure 2-2). On the other hand all the instrumented energy piles fixed in a stiff soil layer (Laloui et al. 2003; McCartney and Murphy 2012a; McCartney et al. 2015; Sutman et al. 2015; You et al. 2016) indicate an increase in the pile axial stress depending on the amplitude of the temperature change and the degree of ground resistance. Additionally, monitoring results reveal that additional pile head

displacement varies with the thermal loading (Laloui et al. 2003; Bourne-Webb et al. 2009; Akrouch et al. 2014) and a special attention should be paid during the design phase in order to avoid any impact on the structural integrity of the building.
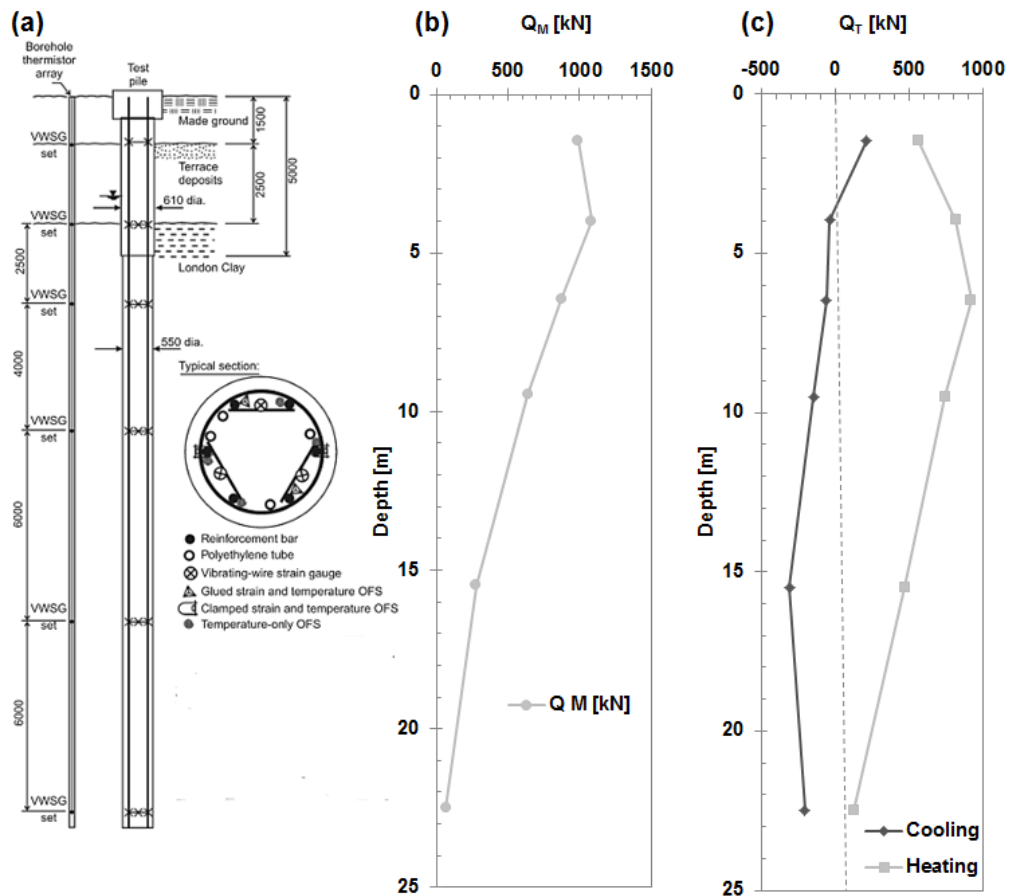
Figure 2-2 Example of the effect of less stiffer pile toe and pile head boundary conditions: Clapham Centre of Lambeth College in London, England (Bourne-Webb et al. 2009) (a) The soil profile and the instrumentation of the tested pile, (b) The loads in the pile due to the mechanical loading, (c) The loads in the pile due to the thermal loading.

Although no examples of foundation failure due to these temperature changes have been identified in the literature, the additional temperature-induced axial stress in the pile may be important, especially at the pile toe where the thermal effects may produce much larger axial stress (Figure 2-2 b and c) than those produced by mechanical loading (Laloui et al. 2006; McCartney and Murphy 2012a; Sutman et al. 2015; You et al. 2016)

Several short (from 1 day to several weeks) cyclic thermo-mechanical tests (Laloui et al. 2003; Laloui et al. 2006; McCartney and Murphy 2012a; McCartney et al. 2015; Olgun and Bowers 2016) indicate that the thermal loads dissipate as the

temperatures recover and regain their initial value, but that over several heating-cooling cycles the pile head settlement increases slightly.

Less information is available in the literature concerning the effects of long-term operation of energy geostructures, namely the effect of long-term cyclic thermomechanical behaviour of energy piles (Brandl 2006; McCartney and Murphy 2012a; Murphy and McCartney 2015; McCartney and Murphy 2017). The long-term monitoring (5 years) of an 8 story building in Denver, Colorado (Figure 2-3 a, b, c) equipped with energy piles (Murphy and McCartney 2015), confirms the fact that, although daily temperature variations may be significant, the temperature profile evolution over the years follows a constant sinusoidal trend (Figure 2-3 b).
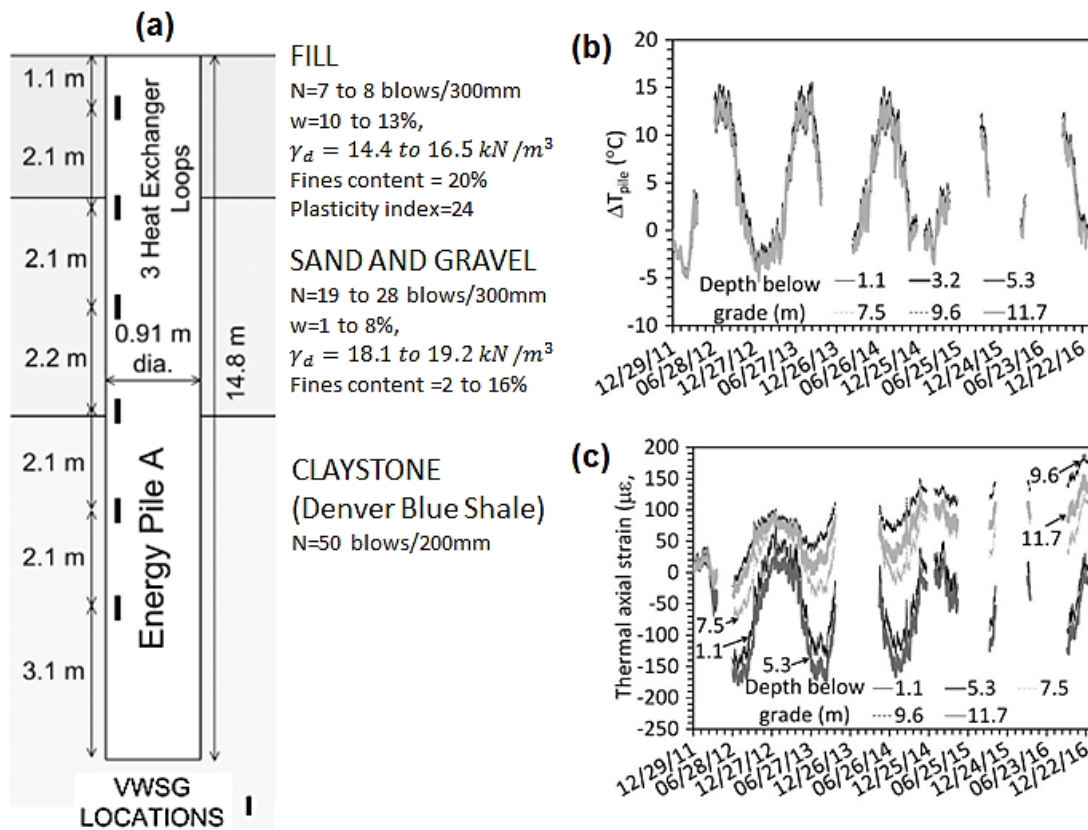
Figure 2-3 Long term therm-o mechanical behaviour of a energy pile under exploitation conditions (McCartney and Murphy 2017) (a) The soil profile and the instrumentation of the tested pile, (b) The evolution of the temperature in the pile, (c) The evolution of deformations in the pile.

Physical models performed in small-scale energy pile showed irreversible settlement of the pile head when the number of thermal cycles increases (Figure 2-4 a, b, c, Ng et al. 2014; Yavari et al. 2014; Nguyen et al. 2017). Numerical studies investigating the thermo-mechanical behaviour of energy piles under several thermal cycles also confirmed the irreversible settlement related to thermal cycles (Laloui and Cekerevac 2008; Suryatriyastuti et al. 2012; Di Donna and Laloui 2015; Olgun et al.

2015; Yavari et al. 2016b; Vieira and Maranha 2017; Fang et al. 2018; Rammal et al. 2018).The above studies showed that the irreversible settlement was negligible at low pile head load and becomes more important at higher pile head load. In addition, the most important irreversible settlement was induced during the first cycle, the effect of the thermal cycles on the irreversible settlement decreases progressively when the number of cycles increases.
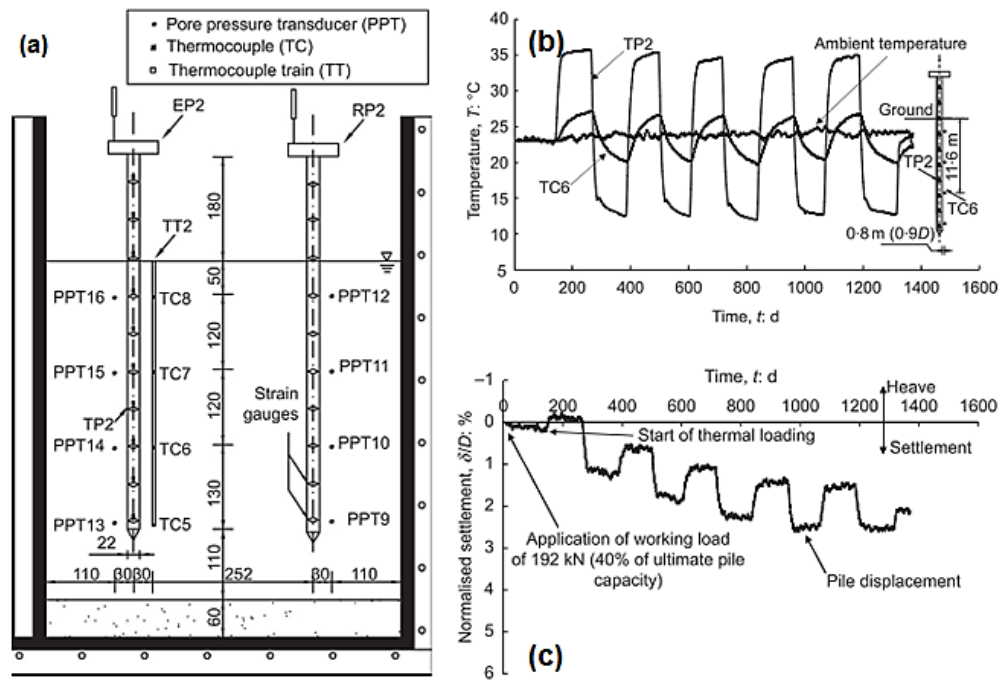
Figure 2-4 Pile settlement due to temperature cycles – Centrifuge test (Ng et al. 2014a) (a) Schematic illustration of the plan view of the centrifuge model, (b) Schematic illustration of the elevation view of the centrifuge model, (c) Measured temeprature hystory o the EP2 pile and the surrounding heavily overconsolidated clay, (d) Measured net displacement of EP2 in heavily overconsolidated clay.

2.3 Ecole des Ponts Paris Tech case study: controlled loading conditions

2.3.1 Project overview

In this section, the results from mechanical and then thermo-mechanical tests of a full-scale experimental energy pile are presented. A 12-m long pile with a nominal diameter of 0.42 m was installed in a site including layers of clay and marl. From the geological profile and soil parameters obtained from the site investigation, the ultimate compression bearing capacity of the pile was estimated at 1800 kN. This value was *a posteriori* confirmed by the ultimate load test performed at the end of the experimental campaign performed on this pile. Several years after its installation, the pile was first loaded to a pile head axial force of 600 kN, which corresponds to the assumed

serviceability capacity. Afterward, while the pile head load was maintained constant, three thermal cycles were applied to the pile to simulate the seasonal thermal loading. The pile temperature, from its initial value (12.5 °C), varied between 4 °C and 25 °C. Each thermal cycle includes one-week heating and one-week cooling periods. The behaviour of the pile under thermal cycles while loaded at its serviceability limit state and the effect of these cycles on its ultimate resistance limit are presented.

2.3.2 Field test details

2.3.2.1 Subsurface conditions

An experimental full-scale energy pile was installed in 2010 (Figure 2-5 a) next to the Coriolis building at the Ecole des Ponts ParisTech, Marne-la-Vallée, France. This pile was built at the same time with the foundation system of the building. The geotechnical profile and soil properties were obtained from the site investigation campaign done prior to the design of the building.
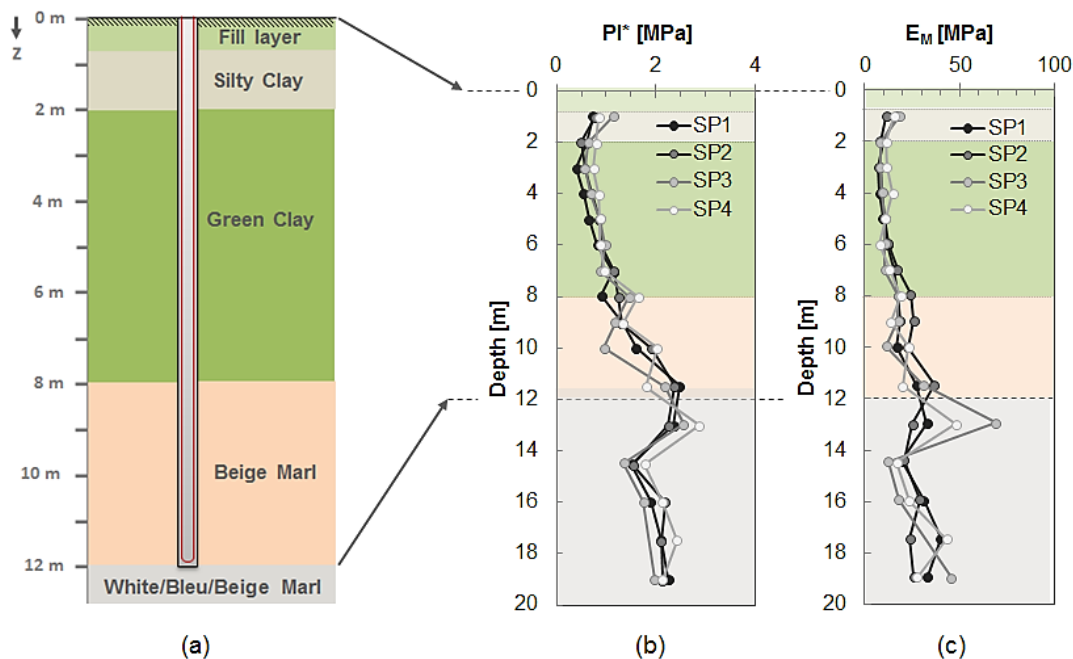
Figure 2-5 (a) Geotechnical profile of the site, (b) Net limit pressure values (in MPa) obtained from pressuremeter tests, (c) Ménard pressuremeter modulus EM obtained from pressuremeter tests.

Four pressuremeter tests (PMT), following the French standard (NF P 94-110), were carried out on the site and up to 20-m deep. The results of all the tests are plotted in Figure 2-5 b and c. Based on the pressuremeter tests and several core samples taken from the field, the geotechnical profile of the site was established as shown in Table 2-1 and Figure 2-5 a. The pile is embedded in various soil layers: Fill, Silty clay, Green clay, Beige marl, White/blue/beige marl, from the surface to the bottom successively.

The pile toe touches the top of the White/blue/beige marl layer situated at 12 m deep. Soil strength parameters (cohesion, c', and internal friction angle φ') were measured from Isotropically Consolidated Undrained (CIU) triaxial tests and Direct shear tests.
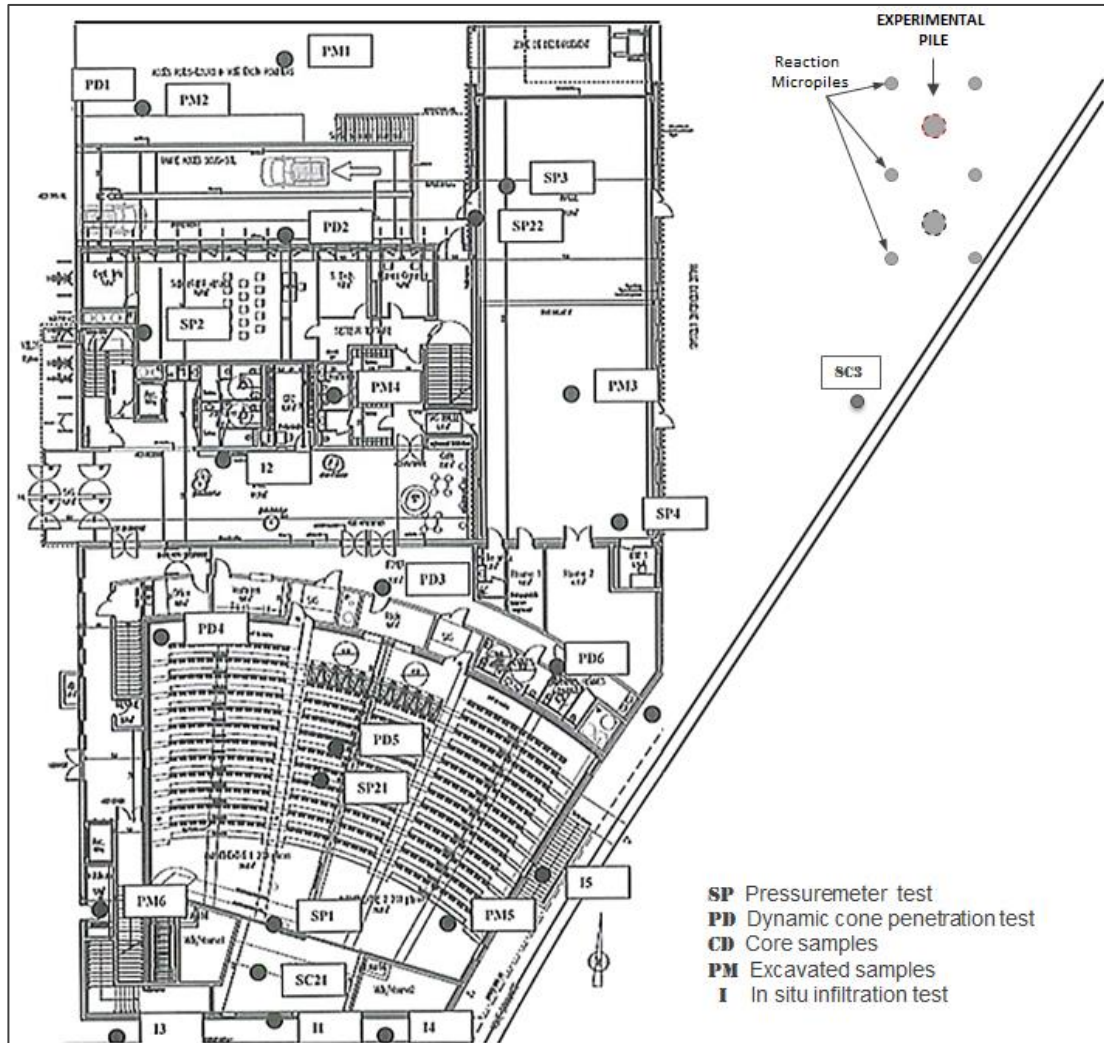
Figure 2-6 The position of the field tests used for determining the soil parameters.

Profile	γ (kN/m3)	Pl* (MPa)	EM (MPa)	c' (kPa)	φ' (°)	ν	qd (MPa)	λ (W/m/°C)	cs (J/kg/°C)	k (m/s)
Fill 0.0-m ÷ 0.7-m	17	0.74÷1.14	11.5÷18.2	5	25	0.33	7÷15	1.0	1200	3E-5
Silty clay 0.7-m ÷ 2.0-m	18	0.74÷1.14	11.5÷18.2	5	25	0.33	7÷15	1.1	1150	1E-7
Green clay 2.0-m ÷ 8.0-m	18	0.5÷1.4	8.0÷18.8	30	22	0.33	3÷20	1.1	1150	4E-8
Beige marl 8.0-m ÷ 12.0-m	20	1.3÷2.4	18.0÷36.0	32	35	0.33	-	1.2	1000	1E-9
White/blue/beige marl 12.0-m ÷ 20.0-m	20	1.3÷2.8	12.0÷68.0	32	35	0.33	-	1.2	1000	1E-9

Table 2-1 Geotechnical profile and soil parameters (Nguyen 2017).

The thermal properties of soil (thermal conductivity, λ, and specific heat capacity, c_s) were measured on core samples taken from the field. The soil hydraulic conductivity, k, was obtained by in situ infiltration test. The tip resistance (q_d) of soil was measured by Dynamic Cone Penetration Test (DCPT) up to 9.0-m deep on site. The water table was identified at 4.0-m with respect to the ground level (Nguyen 2017).
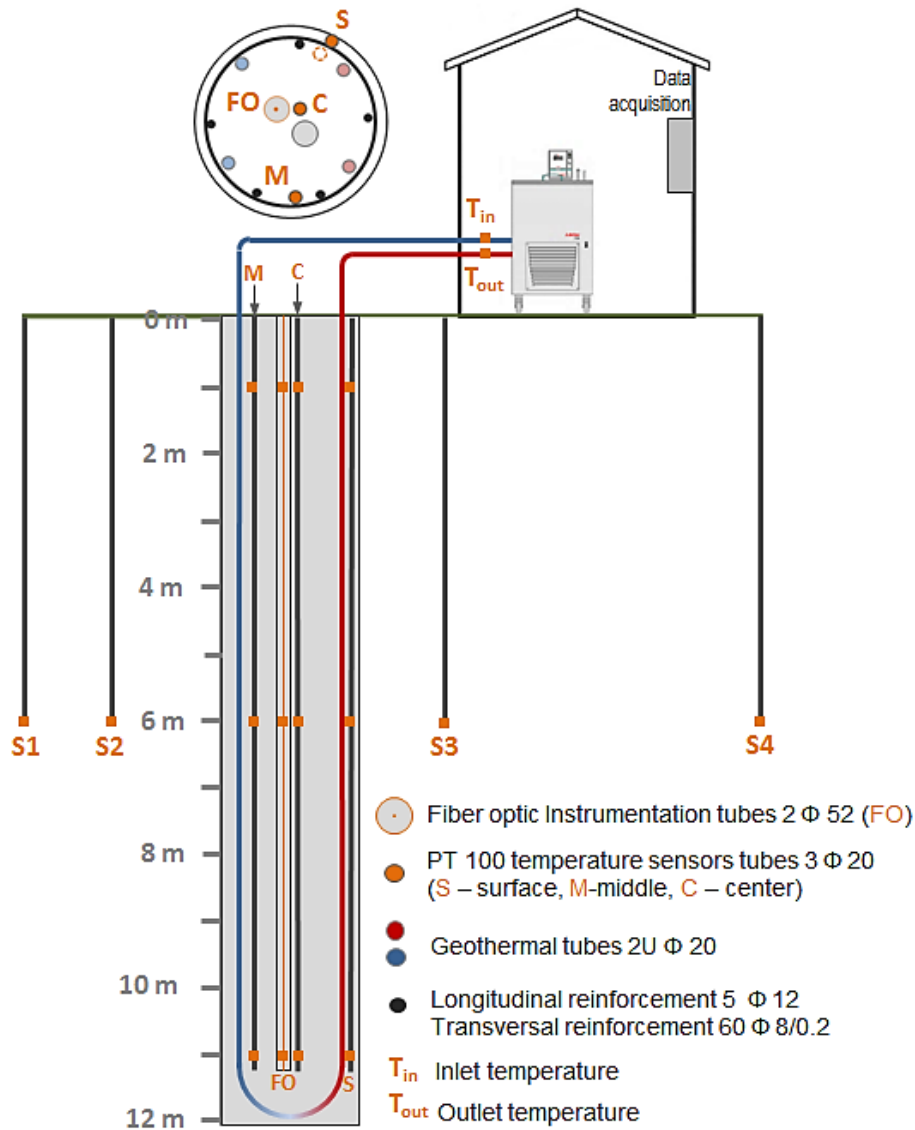
Figure 2-7 Thermal loading system and monitoring.

2.3.2.2 Pile installation

The test pile is 12m long, has a nominal diameter of 0.42m and it was installed by continuous flight auger technique. A full depth reinforcement cage composed of 5 longitudinal rebars Φ12mm and 60 rings of spiral bar Φ8mm was inserted in the fresh concrete (C30/37 (AFNOR 2015)) after the pile drilling. Heat exchanger tubes composed of 2U PEHD loops were attached to the interior of the reinforcing cage in order to ensure the geothermal activation of the pile. Two auscultation tubes of diameter

Φ52mm and 3 additional PEHD tubes Φ20mm were added in the pile in order to facilitate the installation of the instrumentation (Figure 2-7).
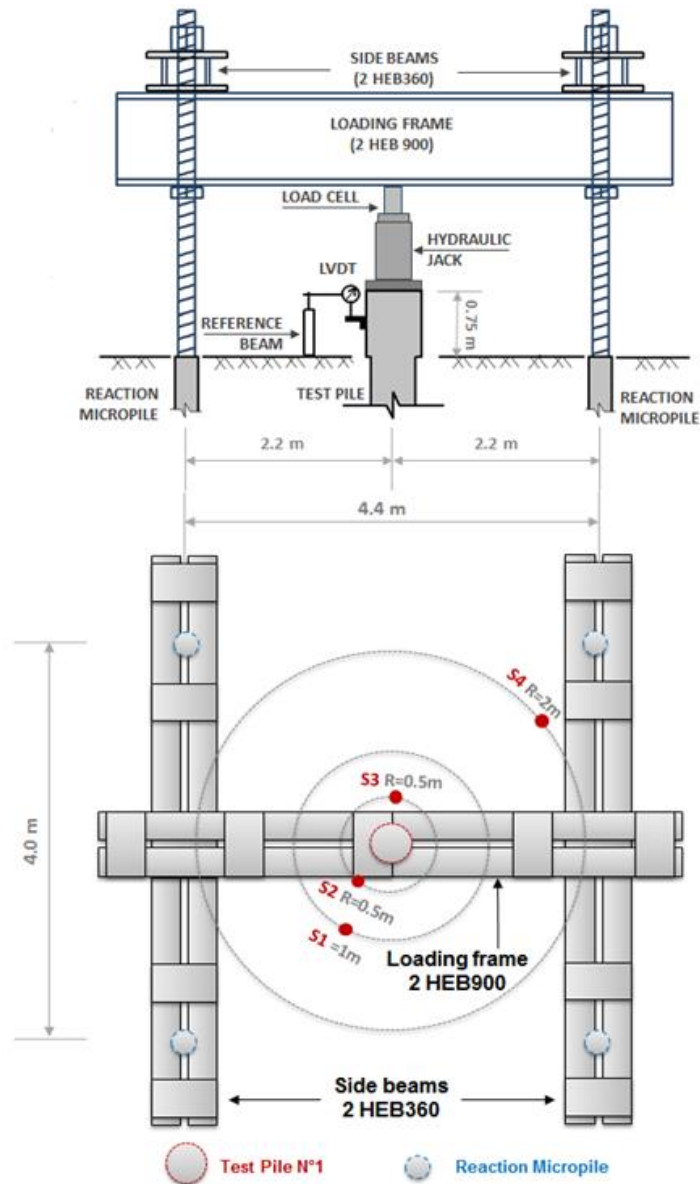
Figure 2-8 The test pile and the mechanical loading system.

2.3.2.3 Loading system

In order to impose an axial load on the experimental pile, a reaction system composed of four anchor piles with dimensions of 0.25-m diameter and 13.5-m length was used (Figure 2-8). The anchor piles were designed to support tensile force up to 700 kN per pile. The loading frame system was used to support the hydraulic jack that allows the application of static load up to 3000 kN.

The thermal loading system consists in a *Refrigerated and heating circulator* connected to the 2U geothermal tubes embedded in the piles (Figure 2-7). The

temperature control is performed by imposing a constant temperature in the water bath. The circulating fluid is a mixture of 66% water and 34% glycol to avoid freezing when temperature is negative.

2.3.2.4 Piles instrumentation

The temperature during experiments was measured at various locations. For the pile temperature, three pipes were embedded inside the pile to host nine PT100 temperature sensors at three depths, 1 m, 6 m and 11 m (Figure 2-7). That allows measuring at each depth the temperature at the pile's centre (C), pile/soil interface (S) and the middle (M) point close to the steel cage, with a precision of ±0.2°C. In addition, three temperature sensors (PT100) were installed at the same depths in the central auscultation tube next to an optic fibre cable (FO) used for measuring both temperature and axial strain along the pile length. The inflow and outflow temperatures of the fluid are also measured by the two PT100 (T_{in} and T_{out} in Figure 2-7) sensors.

The mechanical behaviour of the pile was monitored by various sensors. Two hybrid linear potentiometers with a measurement range of 150 mm (precision ±0.2% of the full-scale range; i.e. ±0.3 mm) were used to monitor the pile head displacement. A load cell was installed on the top of the hydraulic jack in order to monitor the pile head load (Figure 2-8). The pile axial strain was measured by Brillouin optical time-domain reflectometer (BOTDR) sensors installed in one of the two central auscultation tubes (FO).
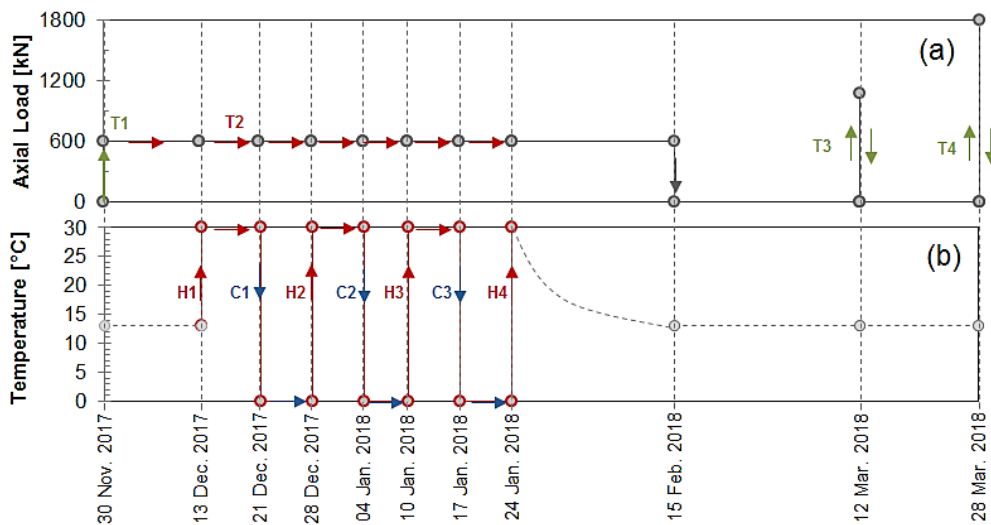
2.3.2.5 Experimental program

Figure 2-9 Test program: (a) Pile head axial load, (b) Temperature of the circulator.

The experimental program is summarized in Figure 2-9. Eight years after the construction of the pile (in November 2009), the pile was first mechanically loaded to its estimated serviceability limit state capacity (T1). A series of heating-cooling cycles were then applied over the duration of eight weeks (T2). For each cycle, the temperature of the refrigerated and heating circulator fluid was increased to 28°C and kept constant for one week and then decreased to 0°C and kept constant for another week. The thermal loading test was stopped after three cycles due to a heat pump malfunction.

After three weeks of thermal recovery, during which the ground cooled back to its initial undisturbed temperature (from 24 Jan. 2018 to 15 Feb. 2018), the pile was unloaded. Due to a power supply cut off the static load test had to be stopped before reaching the pile bearing capacity and the pile was unloaded (T3). A second static load test was carried out and the pile bearing capacity was determined (T4).

2.3.3 Results

2.3.3.1 Mechanical loading (Test T1)

The pile was first mechanically loaded (test T1) to its estimated serviceability limit state following the guidelines provided by the French Standard (AFNOR 1999). The load was increased by six successive steps of 100 kN as shown in Figure 2-10 (a). The load application is considered instantaneous. Although the standard recommends 60-min loading steps, due to the very slow settlement rate (Figure 2-10 (b), (c)) the duration of each step was reduced. Figure 2-10 (b) presents the pile head settlement versus logarithm of elapsed time for each loading step during this first loading test. Applying an axial load up to 600 kN induced an instantaneous settlement followed by an increase of settlement with elapsed time.

The relationship between the settlement and logarithm of elapsed time can be fitted by a linear function. The pile's creep rate can be evaluated from this curve:

$$\alpha_i = (s_{t_f} - s_{t_i})/log(t_f/t_i)$$

Eq. 2-1

where α_i is the creep rate at the loading step i, s_{t_f} is the pile head settlement at the final considered time t_f and s_{t_i} is the pile head settlement at the initial considered time t_i.

As it can be noted in Figure 2-10 (c) the creep rate for each loading step is under 0.3 mm. A linear regression line can be assumed to represent the average creep value for all loading steps. The fact that no important slope change can be identified is a

good indicator of the fact that the maximum applied load lies under the yielding limit. The total pile head settlement recorded is of 2.57 mm (Figure 2-10 (d)).
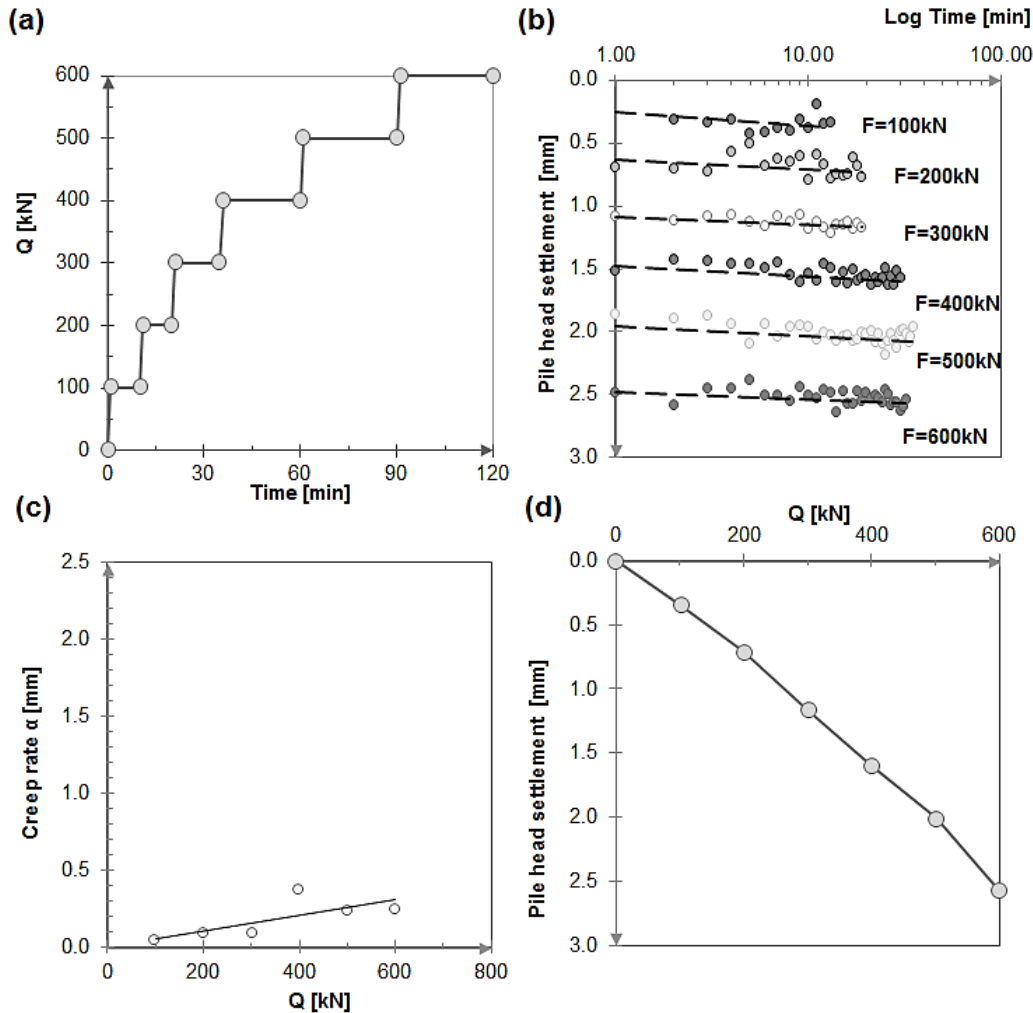
Figure 2-10 Test T1: (a) Pile head axial load versus elapsed time; (b) Pile head settlement versus elapsed time for each loading steps; (c) Creep rate versus pile head load; (d) Pile head settlement versus pile head axial load.
*(Positive force – Compression, Positive displacement – Compression).

The axial strain values (Figure 2-11 (a)) recorded at the end of each loading step, all along the pile using the fibre optic sensors, are smaller than 100 μm/m, indicating that the pile behaviour rests in the elastic domain The elastic domain limit, in this case, was calculated using the method proposed in Eurocode 2 (AFNOR 2015) for C30/35 concrete which is equal to 460 μm/m. Starting from the axial strain records, the axial load along the pile was deduced (Figure 2-11 (b)) assuming a constant pile elastic modulus E = 33 GPa (AFNOR 2015). These results suggest that most of the pile head load is transferred to the soil via mobilized friction on the pile shaft while a small amount of the load is supported by the pile toe.
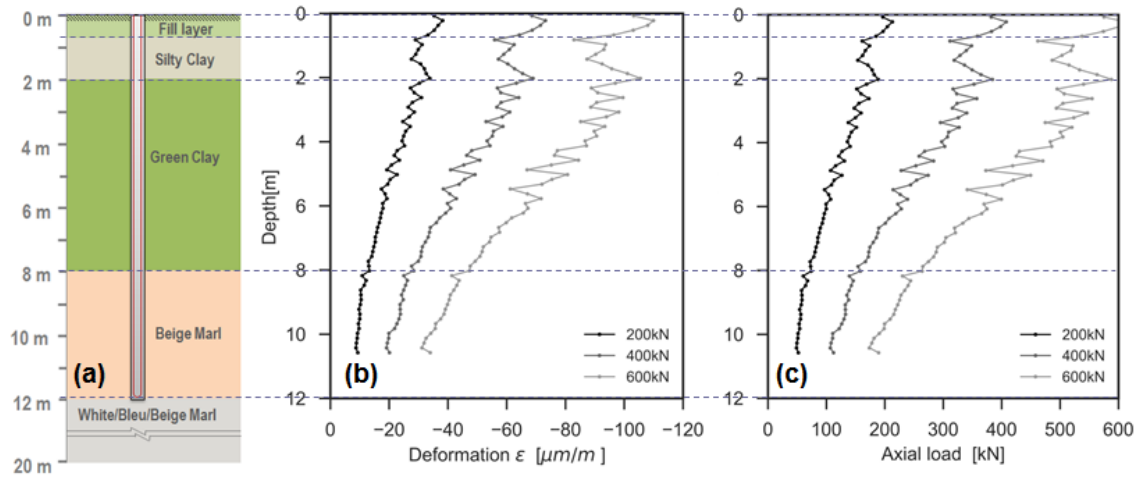
Figure 2-11 Test T1: (a) Strain profiles; (b) Pile axial load profiles.
*(Positive force – Compression, Negative axial strain – Compression).

2.3.3.2 Thermo-mechanical loading (test T2)

Following the mechanical loading, the mechanical load (600 kN) was kept constant for the entire duration of the thermal loading (T2). In order to be able to easily dissociate the effects of the mechanical axial loading from the temperature cycles impact on the pile behaviour, the first temperature cycle was started two weeks after the mechanical loading, on 13 Dec. 2017.

Figure 2-12 shows the evolution of the pile temperature at different depths (b) and the soil temperature at 6 m deep and at 0.5 m, 1 m and 2 m (sensors S1- S4 shown in Figures 2 & 4) away from the pile centre during the thermal cycles as well as the evolution of the air temperature (a). The air temperature was more monitored by the fibre optic cable part that was in direct contact with air (above the pile head). As this experiment was performed from December to February, it can be seen from Figure 2-12 (a) that the air temperature follows the typical Parisian region winter trend with temperatures ranging between -3°C and 12°C (Meteo France).

Unfortunately, due to a power supply issue, the temperature data supplied by the PT100 sensors between 2017-12-13 and 2017-12-15 was lost hence in Figure 2-12 (b) and (c) only the information obtained after 2017-12-15 is presented. It should be noted that the pile temperature (before and during the thermal cycles) is not homogenous (see also Figure 2-15). Actually, the initial pile temperature measured at 1-m deep is 4°C lower than that measured at 6-m and 11-m deep as well as the temperature measured by the soil sensors. This can be explained by the impact of the air temperature on the first five meters of soil (Williams and Gold 1977).
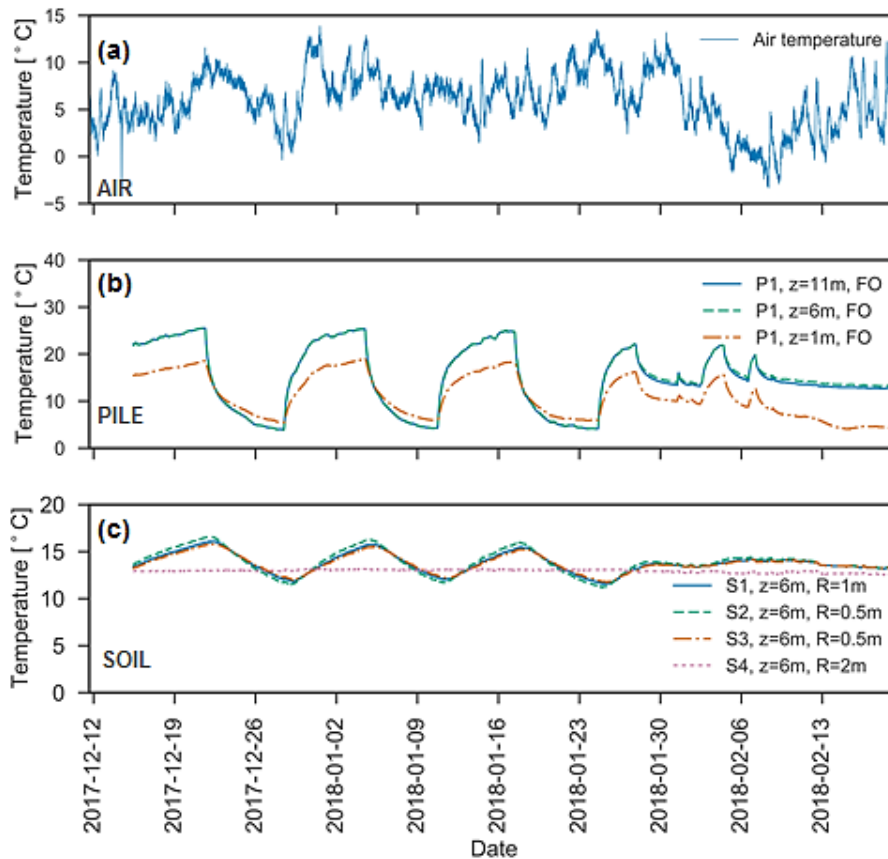
Figure 2-12 Test T2: (a) Air temperature (BOTDR) (b) Temperature evolution in the pile at 1m, 6m and 11m (c) Temperature evolution in the soil (6-m) at 0.5 m, 1 m, and 2 m away from the pile axis.

The temperature of the pile (corresponding to z = 6 m and 11 m in Figure 2-12 (b)) increases from 13°C to 25°C at the end of the first heating step and then varies by 21 °C after each subsequent cooling and heating step. During each thermal cycle, heating increases the pile temperature up to 25°C and cooling decreases the pile temperature to 4°C (Figure 2-15). The temperature values recorded by the fibre optic sensor (Figure 2-15) are slightly different from the ones recorded by the PT 100 sensors due to its proximity to the outlet pipes (Figure 2-7). The undisturbed soil temperature is equal to the initial pile temperature at 6 m and only varies during the thermal cycles at a distance lower than 2 m away from the center of the pile (Figure 2-12 (c)). This small influence zone may be explained by the relatively short time application of the thermal load.

The evolution of the inlet and outlet temperatures (Figure 2-7) is presented in Figure 2-13 (a). Although the temperature of the bath was set equal to 30 °C, the maximum inlet temperature reaches for every cycle, after 7 days, only 28°C. This may be due to the low air temperature and insufficient thermal insulation of the pipes going into the pile.
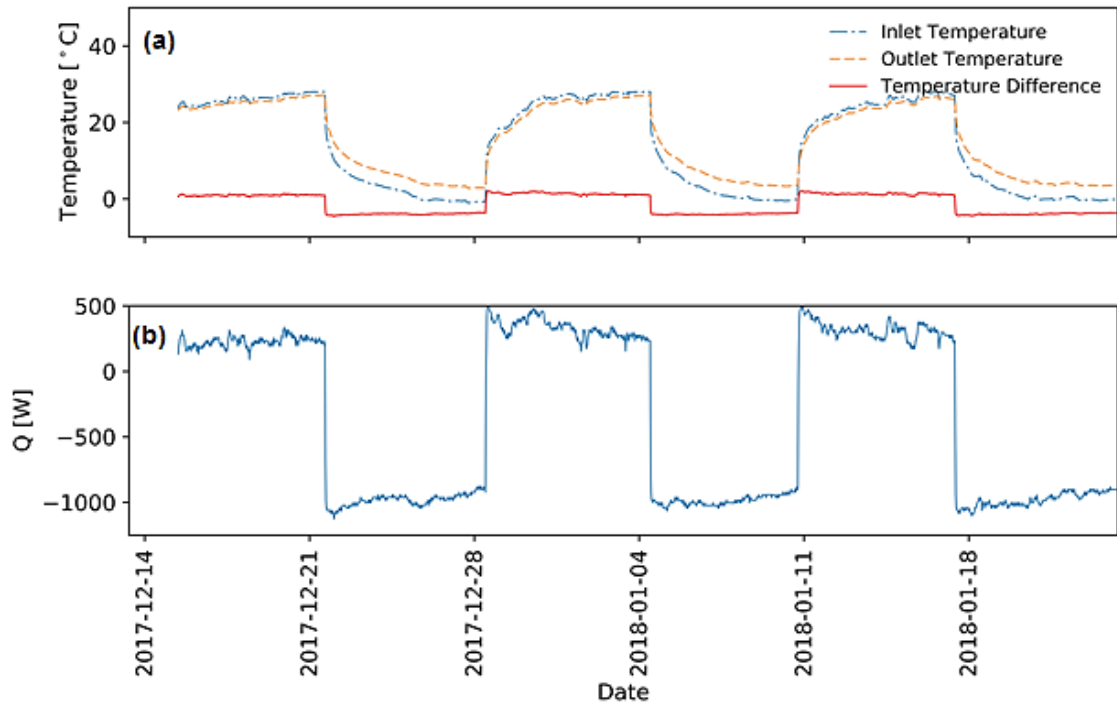
Figure 2-13 Inlet, outlet and the difference between the inlet and outlet temperature during the thermal cycles, (b) Power input during the thermal cycles.
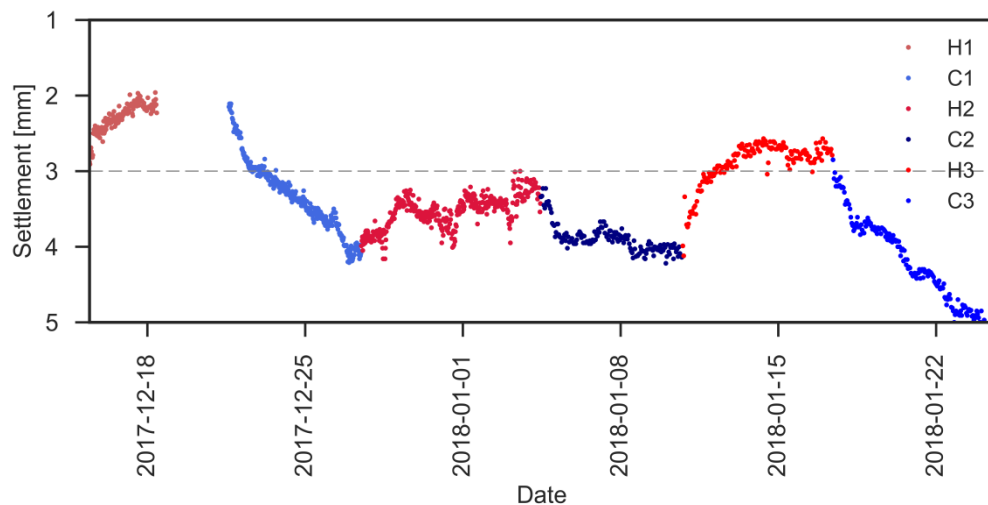
Figure 2-14 Pile head settlement.

These results also show an average temperature difference between the inlet and outlet temperature of 1 °C during heating and of 4 °C during cooling. Considering a constant flowrate equal to 3.4 l/min (measured by the flowmeter) the heat flow injected to the pile during each heating and cooling phase can be then estimated using the following equation:

$$Q = \rho \, c_p \, \Delta T \, v$$

Eq. 2-2

51

Where ρ is the density of the fluid expressed in kg/m^3, c_p is the specific heat capacity, expressed in J/kg °C, ΔT is the difference between the inlet and the outlet temperature expressed in in °C and v is the water flow rate expressed in in m^3/s.

The specific heat capacity of the 66% water 34% glycol fluid mix is calculated from the specific heat capacities of water ($c_{pw} = 4185\,J/kg\,°C$) and glycol ($c_{pg} = 2460\,J/kg\,°C$). In the same way the density of the heat transfer fluid is determined from the densities of its two constituents ($\rho_w = 1000\,kg/m^3$, $\rho_g = 1097\,kg/m^3$). Thus, it results that the average injected heat flow during the heating phase equals to 290 W and the average heat flow extracted during the cooling phase equals to 975 W (Figure 2-13 (b)). In the present work, even if the heat exchanger pipe connecting the pile and the refrigerated and heating circulator was covered with a thermal insulation tube, heat exchange between the ambient air and the pipe (10-m length in total) cannot be negligible. For this reason, the heat exchange rates calculated from Figure 10 correspond to heat exchange between the pile and the surrounding soil plus that between the connecting pipe and the ambient air.
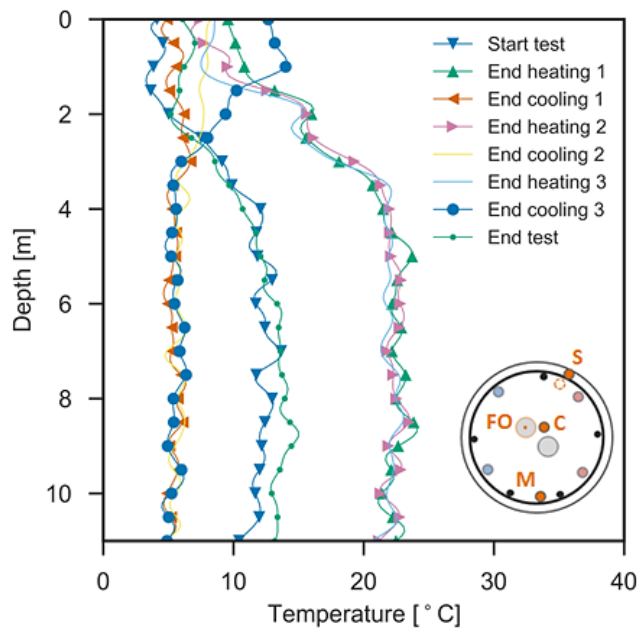
Figure 2-15 Temperature evolution in the pile, measured using the fiber optic sensor.

In Figure 2-15, the pile head settlement was plotted versus pile temperature measured at 6-m deep. The results confirm the trends that have been observed previously: heating induced pile head heave and cooling induced pile head settlement. In addition, this figure shows that the irreversible settlement mainly occurred during the first thermal cycle. That agrees with the findings mentioned by Suryatriyastuti et al. (2014).
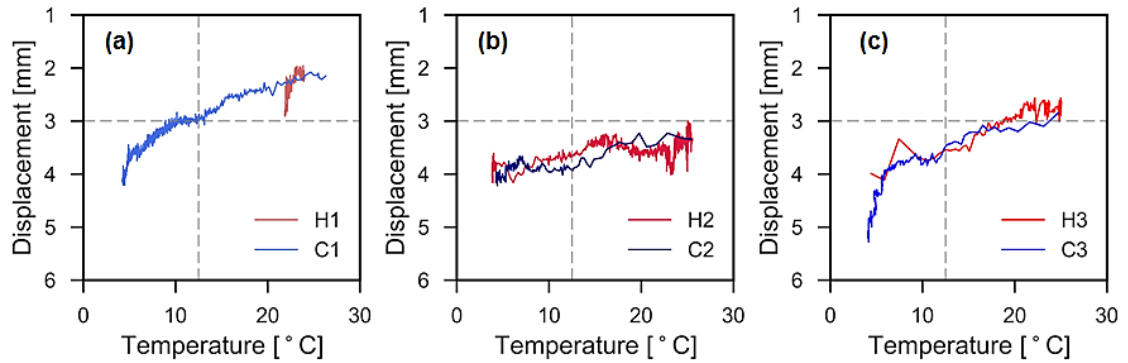
Figure 2-16 The pile head settlement vs the temperature evolution for: (a) the first heating (H1) – cooling (C1) cycle, (b) the second heating (H2) – cooling (C2) cycle, (c) the third heating (H3) – cooling (C3) cycle.

2.3.3.3 Mechanical loading to pile bearing capacity (tests T3 and T4)

Following the end of the thermo-mechanical test T2, the pile was unloaded on 15 Feb. 2018. In order to determine the pile's ultimate capacity, defined as the pile head settlement equivalent to 10% of the pile diameter, a first static load test (T3) was performed on 12 Mar. 2018. This test had to be stopped during the 6th loading step, corresponding to an applied axial load equal to 1080 kN, due to a power cut off. The pile was again unloaded and the test was rescheduled on 28 Mar. 2018 (T4). For the test T4, the load was increased by 360 kN in three successive steps until the maximal load reached in the previous loading test (T3), 1080 kN. Afterward, steps of 180 kN were performed until failure.

The pile head settlement versus elapsed time is plotted in Figure 2-17 (b) only for the test T4. As in the case of test T1, although the standard recommends 60 min loading steps, due to the very slow settlement rate the duration of the first steps was reduced (Figure 2-17 (a)). The creep rate of all the tests (T1, T3, T4) are plotted together in Figure 2-17 (c). The results show that the creep rate was generally lower than 0.4 mm for pile axial load lower or equal to 1080 kN. At higher load, the rate increased quickly. Figure 2-17 (d) plots the pile head settlement versus pile head axial load for the tests T3 and T4. The results confirm the reversible behaviour of the pile when the axial load is lower than 1080 kN. In addition, the results of the two tests are similar in this zone confirming the good repeatability of the experimental procedure. For the test T4, the pile head settlement reached 35 mm (close to 10% of the pile diameter) at 1800 kN of pile head load. For this reason, the pile was unloaded from this step.
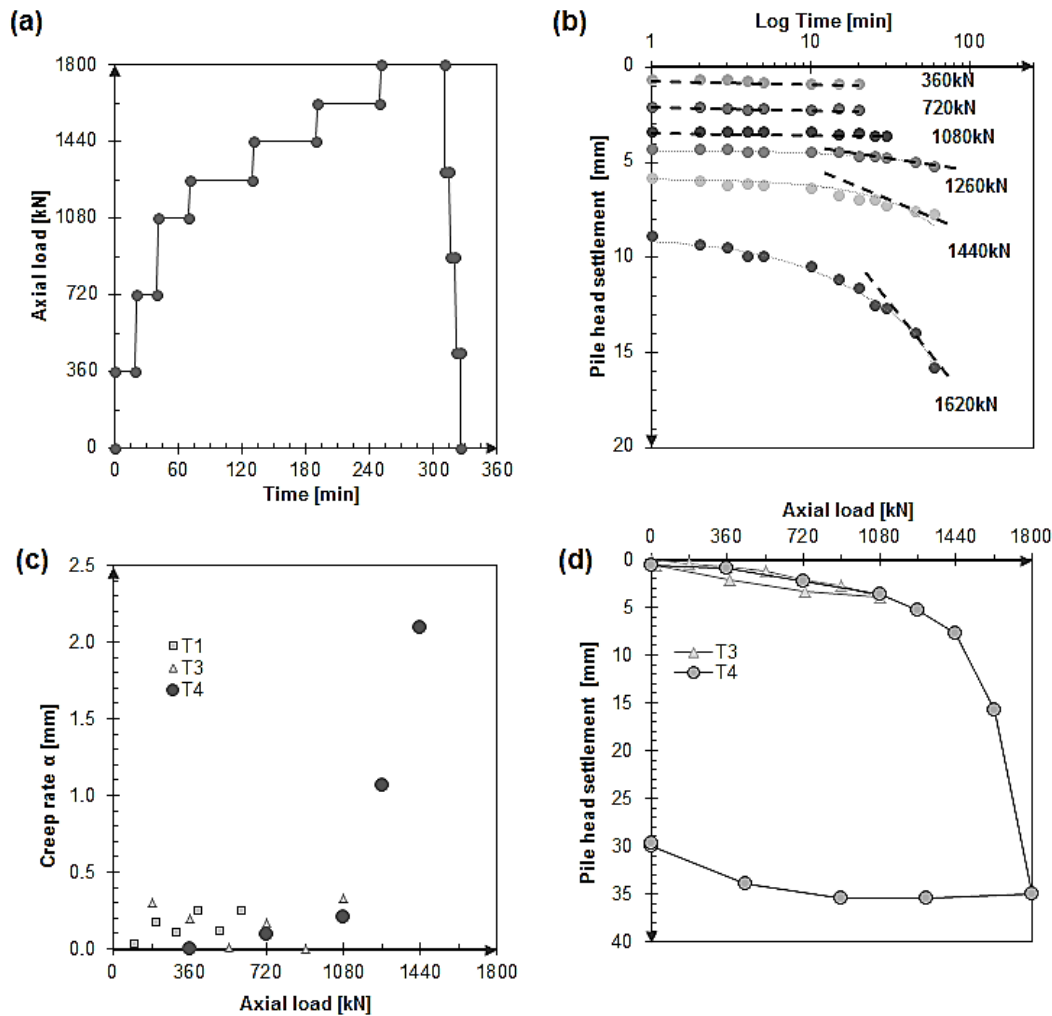
Figure 2-17 Tests T3 and T4: (a) Pile head load versus elapsed time for T4; (b) Pile head settlement versus elapsed time for each T4 loading step; (c) Creep rate versus pile head load; (d) Pile head settlement versus pile head axial load.
*(Positive force – Compression, Positive displacement – Compression).
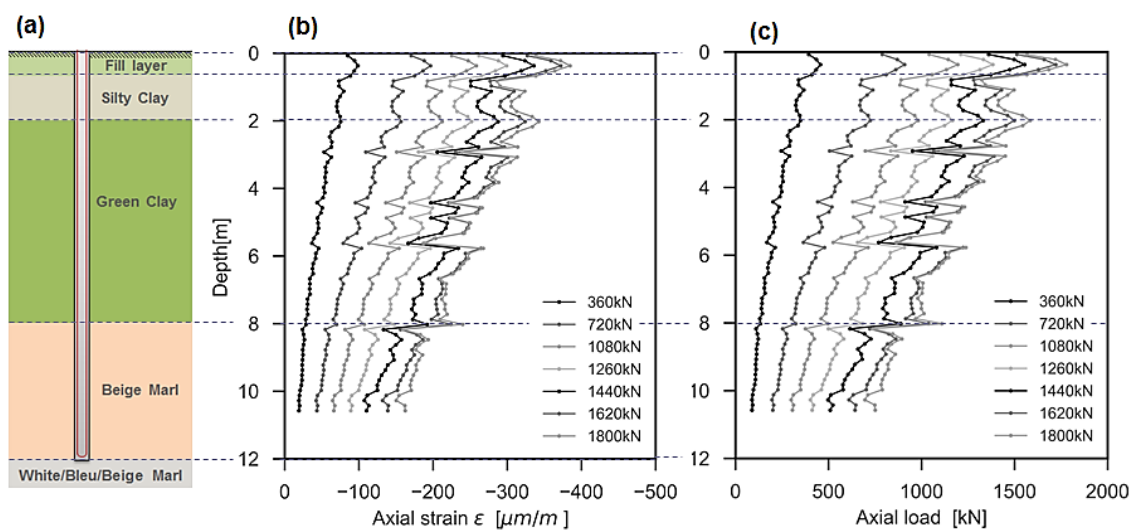
Figure 2-18 (a) Geotechnical profile (b) Axial strain profiles; (c) Axial load profiles.
*(Positive force – Compression, Negative axial strain – Compression).

The axial strain values recorded at the end of each loading step, all along the pile using the fibre optic sensors, are plotted in Figure 2-18 (b). It can be noted from this figure that even after loading the pile to its ultimate capacity, the maximum strain stays within the concrete elastic limit (AFNOR 2015). As for the test T1, starting from the axial strain records, the axial load along the pile was deduced (Figure 2-18 (c)). These results suggest that increasing the pile head load increases the contribution of the pile tip resistance in the load transfer mechanism.

2.3.4 Discussion

The results obtained on the mechanical loading part (Figure 2-10, Figure 2-11, Figure 2-17, Figure 2-18) show good repeatability between the tests. The same trend may be observed in the strain profiles in all the mechanical loading tests. The variation of the strain profiles, for a constant load, may be explained by heterogeneities in the geotechnical profiles, which are confirmed by the soil sampling and by the results obtained in the pressuremeter tests performed in-situ (Figure 2-5). Regardless of the identified soil heterogeneity, the average soil characteristics assumed in the pile design (Table 2-1), proved to be consistent, as good agreement was found between the theoretical method and the experimental results (See Figure 3). These results indicate a mixed load transfer mechanism: most of the load is transferred through the mobilization of the side friction, but depending on the intensity of the load, between 25 and 40% of this load is supported by the tip resistance. As expected, the higher the axial load, the higher the participation of the tip resistance (Figure 2-11, Figure 2-18).

In the present work the pile's temperature variation was imposed at 21°C, except for the first heating phase where the imposed temperature was of +12°C (from an initial temperature of 13°C). Although the functioning of a refrigerated and heating circulator is different from that of a heat pump, which is commonly used in energy geostructure applications, the imposed temperature gradient for this test is similar to annual heating /cooling average temperature variation observed in energy foundations under typical building operation (McCartney and Murphy 2017). Another important remark concerns the relatively short time of thermal load application. While under typical building operation an average temperature gradient of about 30°C is observed (Murphy and McCartney 2015; McCartney and Murphy 2017) over an entire heating/cooling season (6 months), for practical reasons, the temperature gradient was imposed over a duration of only one week in this study. Nonetheless, these shorter

heating/cooling cycles may give a good estimation of the cyclic thermo-mechanical behaviour of an energy foundation.

Observations, after three heating/cooling cycles show that the average temperature within the pile is uniform with the exception of the uppermost few meters (Figure 2-15) due to seasonal climatic variations at the surface, given the fact that the pile head is not insulated.

When a pile undergoes heating/cooling cycles the pile section contracts or expands proportionally to the temperature gradient. This thermally induced movement is however restrained by the side friction at the soil pile interface and at the pile base and pile head, depending on the stiffness of the ground and of the superstructure respectively (Amatya et al. 2012; Bourne-Webb 2013). An irreversible evolution of the pile head settlement with thermal cycles was observed in the present work (Figure 2-14, Figure 2-16), similar to previous observations reported in the literature (Laloui et al. 2003; Bourne-Webb et al. 2009; Murphy and McCartney 2015; You et al. 2016; McCartney and Murphy 2017). Even so, for the same temperature gradient, different pile head displacement amplitudes were recorded for each cycle (Figure 2-16). Although the reference system for the pile head displacement measurement was placed according to the French standard for pile testing (AFNOR 1999), it should be kept in mind that the pile is installed over 6 m of green clay, which is an expansive soil.

2.3.5 Conclusions

The long-term performance of energy foundations was investigated using a full-scale pile. The pile was initially loaded to its estimated SLS capacity and then a series of three heating / cooling cycles were performed. At the end of the thermal cycles the pile was unloaded and then loaded again in order to determine its full mechanical loading capacity. The following conclusions can be drawn:

- Thermal cycles with a temperature gradient of 21°C can well represent annual thermal cycles (McCartney and Murphy 2017); hence each of the three performed cycles can be associated to one year of geothermal exploitation
- The temperature within the pile is uniform with the exception of the first few meters that are exposed to seasonal temperature variations
- The thermal cycles under a constant head load induced small irreversible pile settlement, indicating the influence of the pile-soil interface and the soil behaviour. The most important irreversible settlement occurred after the first thermal cycle.

- Good agreement was found between the theoretical method and the experimental results for the mechanical loading

The results obtained in the present work could help to predict the long-term behaviour of buildings equipped with energy geostructures. A similar test program is being currently conducted on a second pile installed next to the one presented in this study, but for a pile head load equal to 50% of the pile's full capacity, in order to determine the impact of the magnitude of the axial load on the thermo-mechanical behaviour of the pile.

2.4 Sept Sorts case study: geothermal exploitation conditions

2.4.1 Project overview

To better understand the behaviour of energy piles during building operation, three piles (two energy piles and a conventional pile) were instrumented during the construction of a new pretreatment building in a water treatment plant at Sept Sorts, in the NE of Paris. The energy foundation was designed to cover 100% of the heating and cooling needs of the nearby 340 m^2 office building (Figure 2-20). The position of the two instrumented energy piles was chosen in order to highlight the effect of the end restraints: one instrumented energy pile is placed under the foundation slab (P29, Figure 2-19), while the second one is placed under a lateral wall (P18, Figure 2-19), thus providing a much stiffer head restraint. A conventional pile (P15, Figure 2-19) was instrumented to be used as reference as well as to assess the eventual impact of the geothermal activation of the foundation on the conventional piles.

This section is set to emphasize the behaviour of the abovementioned energy foundation a first year before its geothermal activation (from pile installation) and one year after the geothermal activation.

2.4.2 Field test details

2.4.2.1 Subsurface conditions

The energy foundation presented in this section is part of the reconstruction of the Sept Sorts Water Treatment plant project. This project includes the construction of new facilities for the above mentioned Water Treatment Plant in order to increase its capacity. The new facilities were built in different stages while the initial ones were still running and were programmed to be replaced progressively over several years.
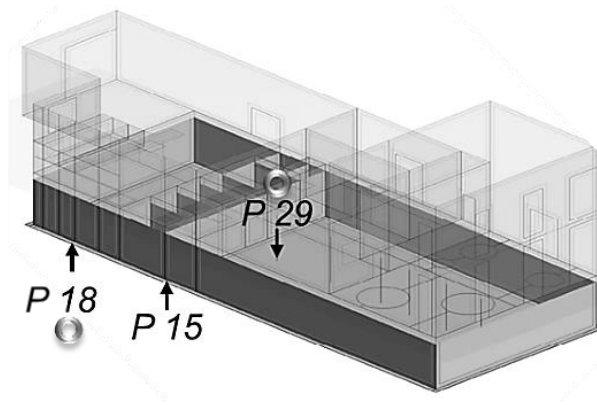
Figure 2-19. Location of the instrumented conventional pile P15 and energy piles P18 and P29 on the 3D plot of the pretreatment building in the Sept Sorts water treatment plant.
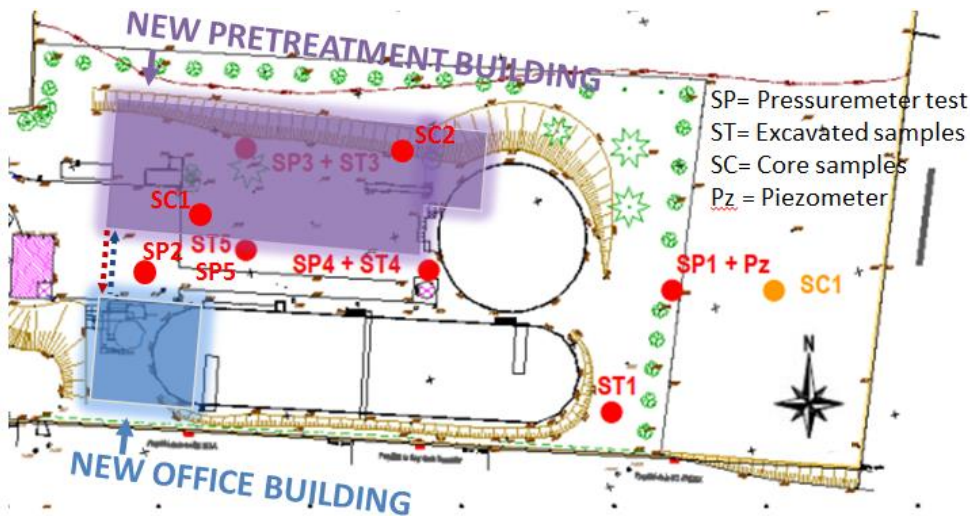
Figure 2-20. The position of the field tests used in determining the soil parameters with respect to the pretreatment building.

Two preliminary geotechnical investigation campaigns (G11: Ginger CEBTP, G11+G12: Semofi) revealed the existence of layers of modern colluvial soil, marl and gravel and coarse limestone, over different inclined planes going from the south to the north limit of the property as depicted in Figure 1 21 a. The physical and mechanical properties of the soils under the pre-treatment building, presented in Table 1 2, were determined starting from several pressuremeter tests (NF- P94-110) and core samples (Volumetric weight - NF P94 051; Water content: NF P94-050). Soil strength parameters (cohesion c', internal friction angle φ' and Poisson's ratio ν) were provided in the Foundations and Retaining Structures Geotechnical Study (G3). The soil thermal properties (thermal conductivity, λ, and specific heat capacity, C_s) were provided in the thermal design documentation. The water level, determined from a piezometer, was found at 50m NGF (General Levelling of France).

Profile	ρ (kg/m3)	w (-)	Pl* (MPa)	EM (MPa)	c' (kPa)	φ' (°)	ν (-)	λ (W/m/°C)	Cs (J/kg/°C)
Modern colluvial soil	2030	0.16	0.5	5	0	30	0.33	0.6-1.8	1.8-2.0
Marl and altered gravel	1960	0.27	1	11	5	25	0.33	1.5-2.5	2.2
Marl and gravel	1960	0.27	2	30	10	25	0.33	1.5-2.5	2.2
Coarse limestone	1780	0.23	5	100	50	30	0.33	1.2-2.5	2.1-2.4

Table 2-2 Geotechnical profile and soil parameters
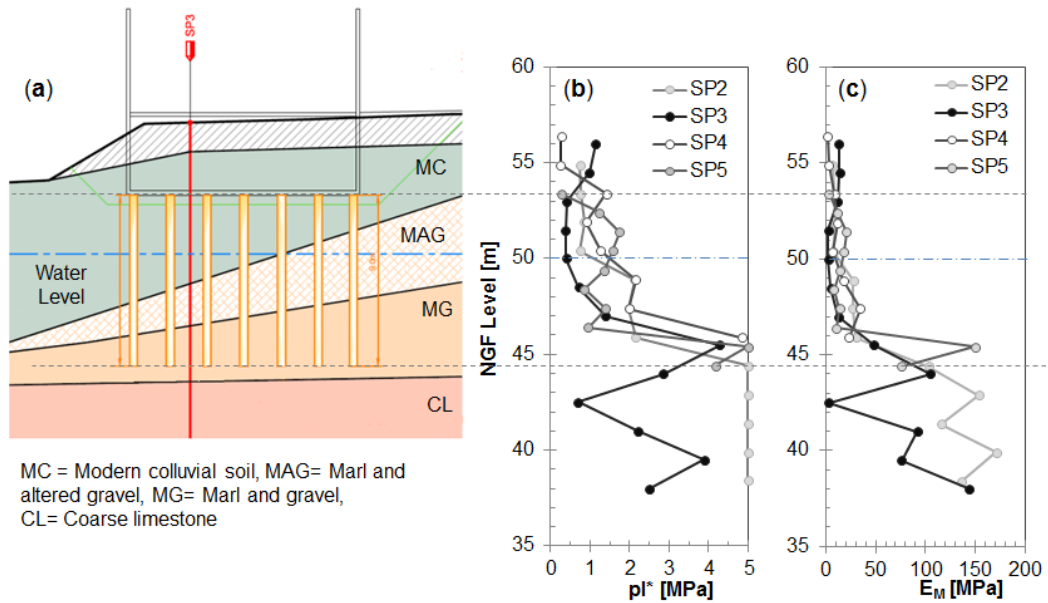
Figure 2-21 (a) Geotechnical profile of the site, (b) Net limit pressure values (in MPa) obtained from pressuremeter tests, (c) Ménard pressuremeter modulus E_M obtained from pressuremeter tests, represented against the NGF (General Levelling of France) system of reference.

2.4.2.2 Pile installation

The pretreatment building is supported by 100 concrete piles, out of which 45 are energy piles, 9 meters long with a nominal diameter of 0.42m. All energy piles are equipped with full depth reinforcement steel cages composed of 6 longitudinal rebars Φ14mm and 36 spiral bar Φ10mm which were inserted in the fresh concrete (C30/37 (AFNOR 2015)) after the pile drilling. Heat exchanger tubes composed of 2U polyethylene high-density (PEHD) loops were attached to the interior of the reinforcing cage in order to ensure the geothermal activation of the pile (Figure 2-27 a).

All the piles were executed by continuous flight auger technique: a hollow steam auger with continuous flights is drilled into the soil to the design depth. The auger is then slowly removed with the drilled soil as concrete is pumped through the hollow steam. The reinforcement cage is then lowered into the wet column. Once the concrete hardens, the top 40 cm of the pile are carefully being trimmed in order to expose the

reinforcement for incorporation into the pile cap. Different stages of the piles' construction phases are illustrated in Figure 2-22.

Parameter	Value
Cement CEM III/A 42.5 N	$320 \ kg/m^3$
Sand 0/4 Morgagny Perigny	$693 \ kg/m^3$
Sand 0/1 Samin Butte du Moullin	$132 \ kg/m^3$
Gravel 4/10 Morgagny Matignicourt	$942 \ kg/m^3$
MasterGlenium SKY 537 (Superplastifiant)	$1.92 \ kg/m^3$
Water	$175 \ kg/m^3$

Table 2.3 Concrete mix design.

Property	Value
Density	$2350 \ kg/m^3$
Compressive strength	$44 \ MPa$
Tensile strength	$2.9 \ MPa$
Young Modulus	$33 \ GPa$
Poison's coefficient	0.2

Table 2.4 Concrete - Mechanical properties.
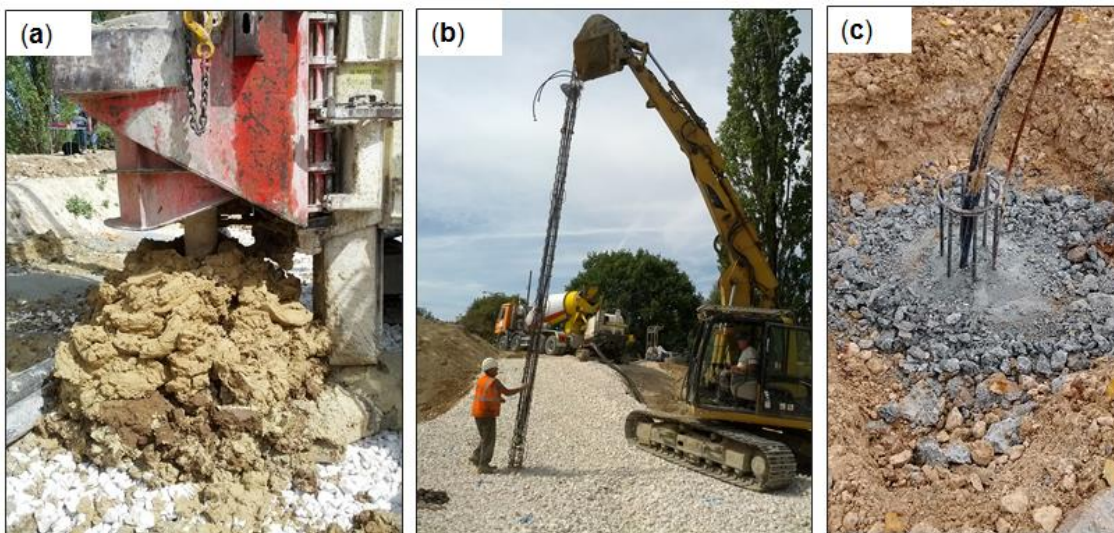
Figure 2-22 Pile installation by continuous flight auger (CFA) method: (a) Drilling, (b)The reinforcement cage is being prepared before being lowered in the fresh concrete column (c) The pile head after teaming.

Figure 2-23, Figure 2-24 and Figure 2-25 show the data recorded during the pile installation. The diameter of the pile, for each profile, is estimated from the volume

of concrete injected at each depth. Except small differences in the pile toe and pile head, the three piles have an almost constant diameter over their respective lengths. The auger torque varies between 7.5 and 22.5 MPa during drilling, its variations being related to the geological profiles of the soil. The auger torque profiles are similar between the 3 piles, illustrating the similarity of the soil profiles identified from the pressuremeter tests (Figure 2-21 b).
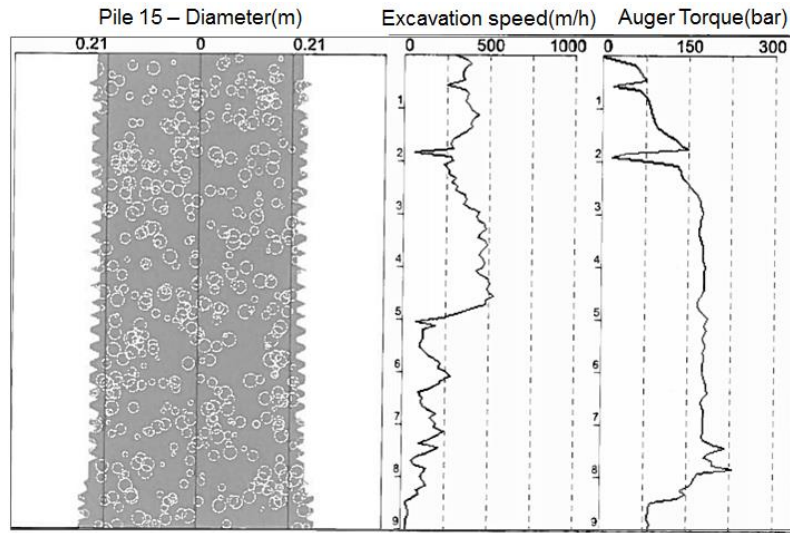
Figure 2-23 Pile 15 – Pile diameter, excavation speed and auger torque recorded during pile installation.
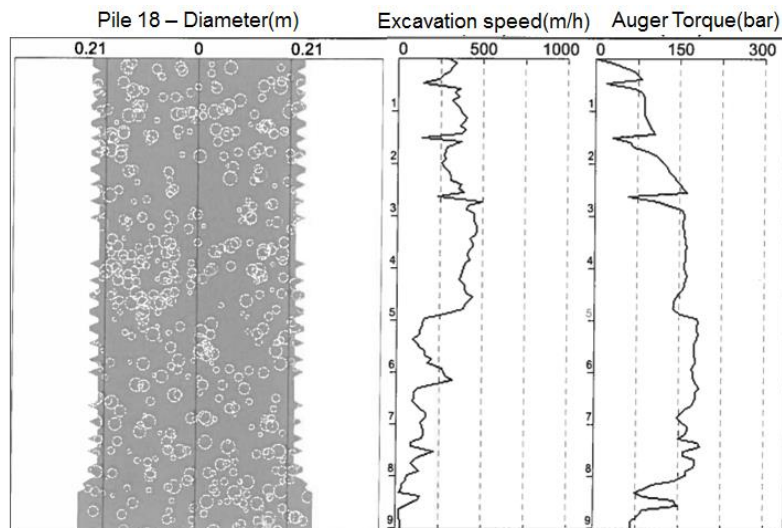
Figure 2-24 Pile 18 – Pile diameter, excavation speed and auger torque recorded during pile installation.
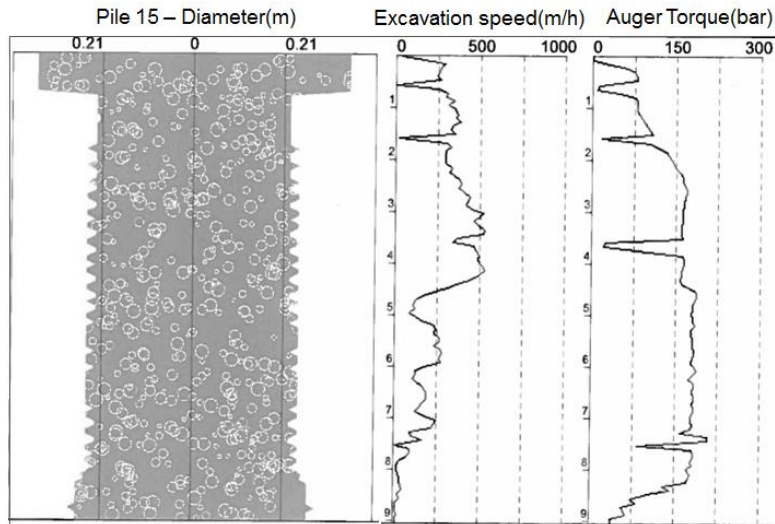
Figure 2-25 Pile 29 – Pile diameter, excavation speed and auger torque recorded during pile installation.

2.4.2.3 Ground source heat pump system

In order to meet the heating and cooling needs of the new 340 m^2 office building from the Sept Sort Water Treatment Plant, 45 out of the total 100 piles (Figure 2-20), were equipped with geothermal loops. Each geothermal loop is composed of 2U PEHD pipes (W configuration), attached to the interior of the reinforcement cage.
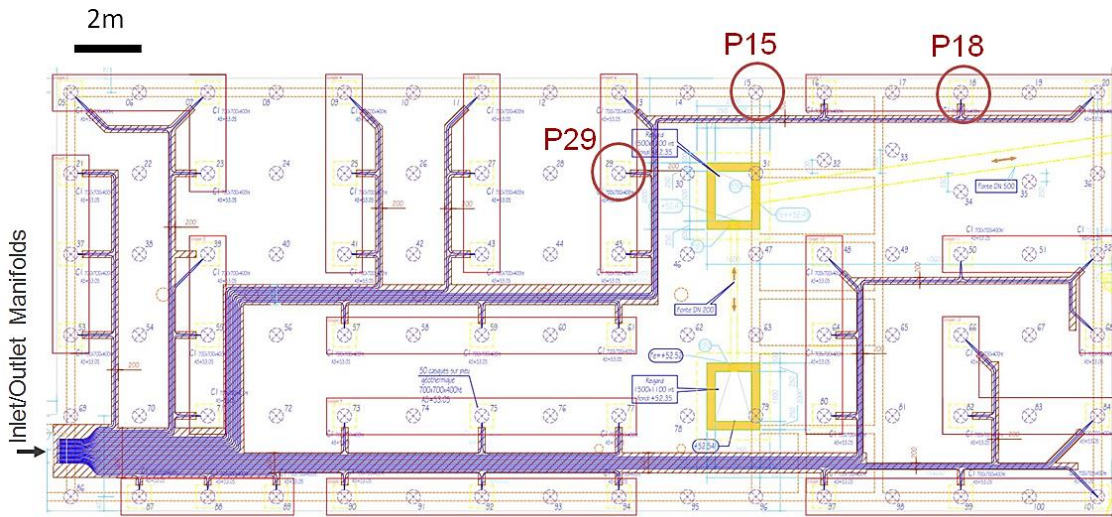
Figure 2-26 The position of the three instrumented piles P15, P18 and P29 on the geothermal network plan.

Horizontal connections were installed in order to form 15 parallel groups, each containing 3 piles in series, linked to a the inlet/outlet manifolds installed in a manhole in the east part of the building . The fluid (10% glycol, 90% water) circulating in the energy foundation is then collected through an insulated Φ40mm PEHD pipe connected

to the heat pump system installed in the mechanical room from the office building (Figure 2-20).

The heat pump (RWEYQ8T from Daikin), is able to supply a heating capacity of up to 25kW and cooling capacity of up to 22.4kW and guarantees a COP of up to 5.8. A list resuming the parameters used in the design of the ground source heat pump system can be found in Table 2.5.

	Property	Value
Pile	Number of equiped piles	45
	Average length of the tubes installed in a pile (4 tubes in W configuration)	$28\ m$
	Tubes diameter	$PEHD\ 25x3mm$
	Number of piles connected in series in a single geothermal network	3
	Pile thermal resistance (Rb)	$0.069\ K/(W/m)$
	Internal thermal resistance (Ra)	$0.236\ K/(W/m)$
Soil	Undisturbed temperature	$13°C$
	Average volumetric heat capacity	$2000\ kJ/m^3K$
	Average heat conductivity	$1.4\ W/mK$
Geothermal System	Fluid type	Water / monopropylene glycol 10%
	Minimum/Maximum temeprature	$0°C/30°C$
	Number of geothermal networks	15
	Maximum debit	$6.75\ m^3/h$
Heat Pump	Power heating/cooling	$25\ kW/22.4\ kW$
	Cooling inlet water temperature range	$10\ °C/45°C$
	Heating inlet water temperature range	$-10°C/45°C$
	COP	5.8

Table 2.5 Ground source heat pump system.

2.4.2.4 Pile instrumentation

Seven vibrating wire strain gauges (VWSG, Glotzl ECV150) were incorporated inside each instrumented energy pile: P18 and P29 (Figure 2-27 a) in order to monitor the distribution of axial strain as a function of depth. The sensors were oriented longitudinally and attached to the transversal reinforcement bars then cast in fresh concrete during pile installation. Each vibrating wire sensor is equipped with a thermistor to monitor the temperature variations at each sensor location (Figure 2-27 a).

Five vibrating wire sensors (Glotzl ECV150) were installed in the conventional pile P15 to quantify the effect of geothermal activation of the foundation on non-

geothermal piles (Figure 2-27 b). The conventional pile P15 is therefore considered as the reference pile.

Cables from each sensor were routed from the foundation to the manhole where the manifolds for the 15 energy piles groups are installed, before casting the slab. Two Geokon Inc. data logger (Model 8002) were used to record data hourly before the geothermal activation and for every 15 min for the period afterwards, with a precision of ±1.5microstrain for the VWSG and ±1°C for the thermistors. Each data logger is also equipped with a thermistor, recording the temperature in the manhole (foundation level, 3 meters below the ground level).

During pile installation a VWSG located at 7.7m below ground level in Pile P15 and one located at 7.7 m below grade in energy pile P29 were damaged. However the corresponding thermistors remained operational.

In addition to the instrumentation in the foundation, a set of two PT 100 temperature sensors were installed in April 2018 on the inlet/outlet circuit close to the manifolds , in order to assess the inlet-outlet temperature from the foundation. Another couple of PT100 sensors were installed on the inlet/ outlet pipes from the mechanical room to account for the thermal loss between the manifolds and the GSHP system. A PT100 sensor was installed in front of the office building to account for the variation of the air temperature. The PT100 sensors have a precision of ±0.3°C.

2.4.2.5 Calibration of the field test data

As mentioned in the previous sections, throughout the field test strain data was recorded by vibrating wire strain gauges (VWSG). The principle of functioning of VWSG sensors consists in a length of steel wire being tensioned between two end blocks that are firmly in contact with the mass of concrete. Deformations in the concrete cause the two end blocks to move in relation to each other, altering the tension in the steel wire. This change is measured as a change in the resonant frequency of the wire. The strain $\varepsilon = \Delta l/l$ expressed in $\mu m/m$ is obtained as follows:

$$\boldsymbol{\varepsilon = k(F^2 - F_0{}^2)} \hspace{4cm} \textbf{Eq. 2-3}$$

where $k = 4.065$ is the gauge factor, provided by the sensor manufacturer, F^2 and $F_0{}^2$ are the current and initial resonant frequency values.

Positive strain values denote sensor extension and negative strain values correspond to sensor compression.

Temperature variations can affect the strain gauge recordings, since increasing temperatures leads the vibrating wire to elongate slightly and thus provides a lower frequency reading than the external stress field may actually be exerting on the VWSG instrument. This gives a false indication that the concrete is undergoing compressive strain (Marshall and Hunter 1980). A correction for temperature accounting for the change in temperature is therefore necessary:

$$\varepsilon_{obs} = \varepsilon + \alpha_s \Delta T \qquad \text{Eq. 2-4}$$

where ε_{obs} is the observed strain, ε is the strain obtained from the variation of the resonant frequency of the VWSG recorded by the data logger, $\alpha_s = 11.83 \mu m/m°C$ is the coefficient of the steel thermal expansion and ΔT is the temperature change.

The observed strain is the change in unit length of the pile that would be measured by a dial gauge at the surface; hence it is a measure of the pile deformation. However to investigate the thermally induced axial stress along the piles, the effect of the mechanical loading (loads from the superstructure or soil pressure) should be separated from the thermal loading. The total strain recorded in a pile can be defined as follows:

$$\varepsilon_{Total} = \varepsilon_M + \varepsilon_{obs} \qquad \text{Eq. 2-5}$$

where ε_M is the strain due to mechanical loading and ε_{obs} is the strain due to temperature variation .

If the pile is not restrained, it would deform freely and its thermal strain could be determined as follows:

$$\varepsilon_{Free} = \alpha_c \Delta T \qquad \text{Eq. 2-6}$$

where ε_{free} is the free deformation of an unconstrained pile $\alpha_c = 10 \mu m/m°C$, is the coefficient of thermal expansion of concrete , ΔT is the temperature change.

If the pile were completely restrained, the observed deformation would be equal to zero which would result in thermally induced axial stress along the pile.

The behaviour of an energy pile is however between these two cases (free boundary conditions and completely restrained boundary conditions). The superstructure and the soil provide boundary restrains but cannot completely prevent thermal deformation. The blocked strain along the energy pile can be determined as follows:

$$\varepsilon_b = \alpha_c \Delta T - \varepsilon_{obs} \qquad \text{Eq. 2-7}$$

where ε_{Th} is the observed thermal strain, $\alpha_c = 10 \mu m/m°C$ is the coefficient of thermal expansion of concrete and ΔT is the temperature change.
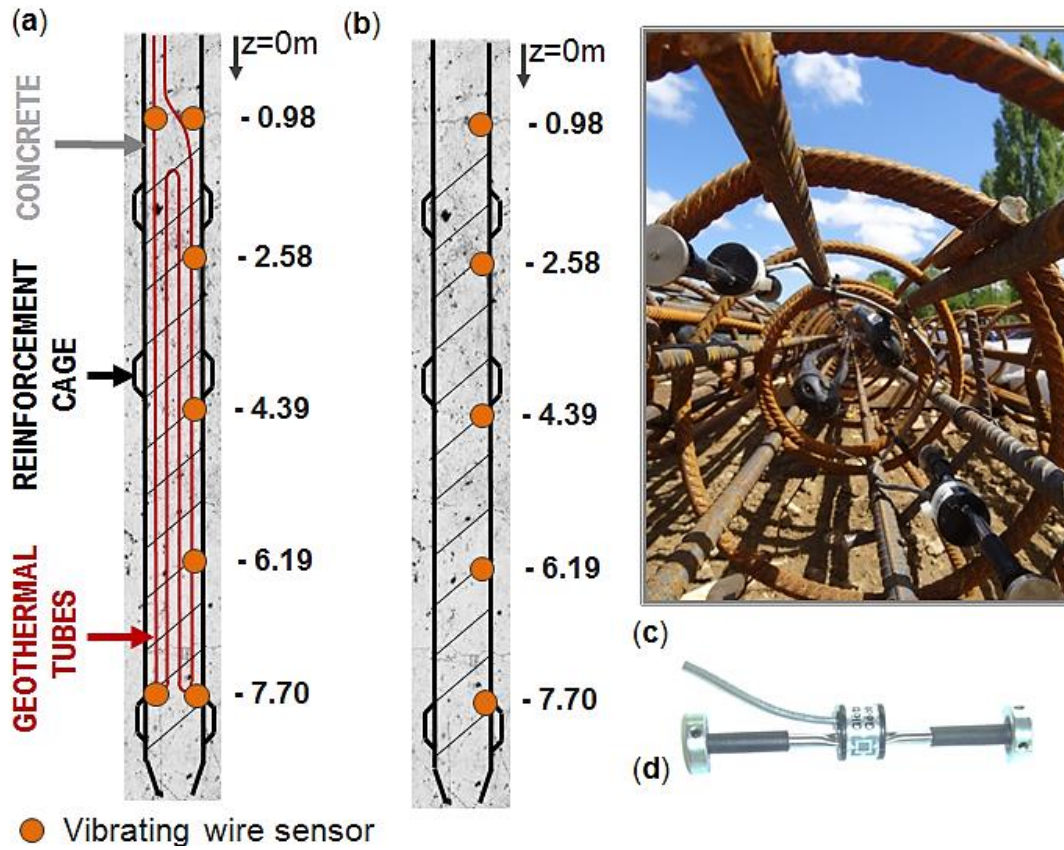
Figure 2-27 (a) Energy Piles P29 and P18 profile and sensors positions, (b) Pile P15 profile and sensors position, (c) Pile P29 reinforcement cage before pile installation, (d) Glotzl vibrating wire sensor

2.4.3 Results

2.4.3.1 Pile installation

When the constituents of concrete (Table 2.3) are mixed the cement and water chemically react resulting in a fluid cement paste. The first reactions are very intense and a high amount of heat is released in a short period of time. In the following hours the chemical reactions slow down and the hydration process ceases resulting in a "dormant period" (Soroka 2013). During this time, the fresh concrete is transported from the concrete station to the construction site and it is poured into the piles. The cast concrete exchanges heat with the surrounding soil usually resulting in a decrease of temperature. After the dormant period, a period of intensive hydration starts. The most important consequence of hydration process is the transformation of concrete from a multiphase fluid mixture to a solid multiphase composite (Glisic 2000). Setting starts

once the hydrated cement particles begin to be in mutual contact (initial set) and ends when the cement paste becomes solid (final set). An exothermic reaction occurs during this phase. This phenomenon may lead to very early onset of thermal cracks in the absence of any mechanical load. Temperature rise varies by many parameters including cement composition, fineness and content, aggregate content, coefficient of thermal expansion, section geometry, placement, and ambient temperatures. The final set is followed by a period of slow hydration at low heat release (Mehta and Monteiro 2006).
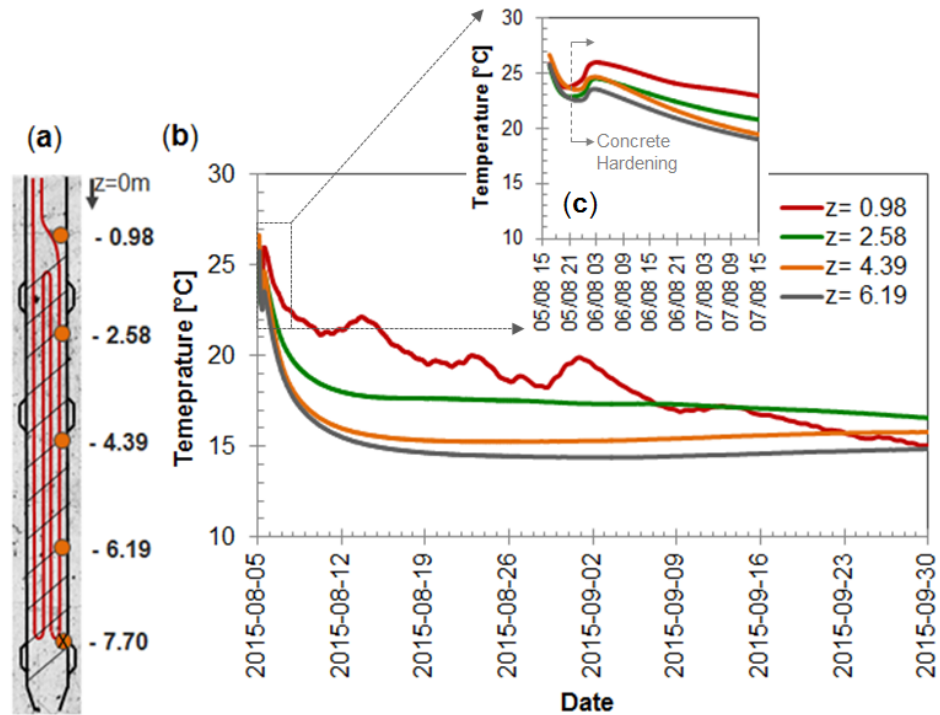
Figure 2-28 (a) Position of the thermistors in pile P29 (b) Hydration temperature of the pile P29 (c) The hydration temperature during the first two days after concrete pouring

In order to account for the temperature and the strain changes in the pile during the concrete hardening, pile P29 was monitored for 56 days (8 weeks) after its installation. Figure 2-28 a presents the evolution of the concrete temperature during the strength gain and the steady state phases. Once placed, the concrete starts to harden and gain strength. The heat generated in this phase lasts in this case, about six hours (Figure 2-28 (c)) and is caused mainly by the reaction of the calcium silicate which creates "second-stage" calcium silicate hydrate (C-S-H), the main reaction product that provides strength to the cement paste. Only a small increase in temperature of $\Delta T=3°C$ was recorded during concrete setting. This may be explained by the cement content (high blast furnace slag content). After this phase ends, the concrete temperature decreases approaching the soil temperature over the next eight weeks. The temperature

variation recorded at 0.98m below the foundation level can be explained by the influence of the atmospheric temperature. Past this depth, the concrete's temperature decreases progressively with depth. Unfortunately the temperature sensor located at 7.7 m below the foundation level, malfunctioned during this stage of the test, and no data is available.
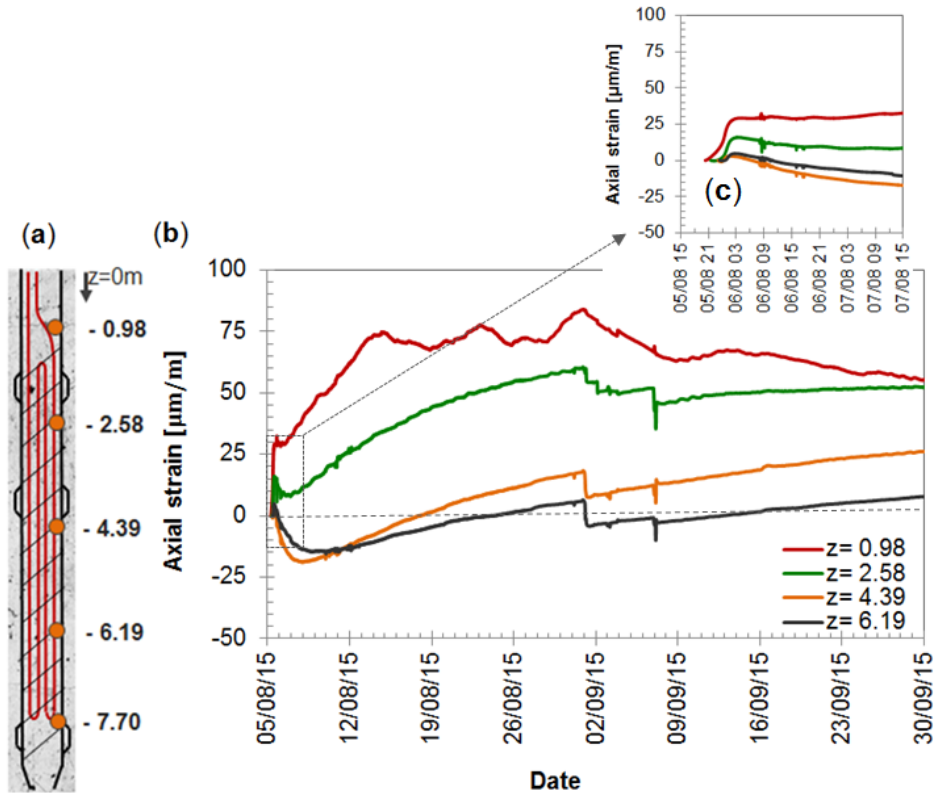
Figure 2-29 (a) Position of the thermistors in pile P29 (b) Strain of the pile P29 during hardening (c) Strain of the pile P29 during the first two days after concrete pouring.

The variation of total strain (thermal and mechanical, for free pile head) after the initial set is presented in Figure 2-29. During concrete setting, positive axial strain (extension) ranging between $5 - 30\ \mu m/m$ was observed, the highest value being recorded close to the pile head. These values are consistent with the temperature variation. After the final set, all but the top sensor indicate development of compressive strains during the following two days, after which the axial strain values begin to increase again. After 28 days (standard time for concrete hardening) the axial strain in the sensors below 4 m deep are close to zero while the sensor at 2.58 m and 0.98m present positive deformation (extension) values amounting to $50\ \mu m/m$ and $\sim 75\ \mu m/m$ respectively. These values continue to increase for the following 4 weeks. The variation in the top sensor deformation may be attributed to variable atmospheric

conditions (temperature, humidity) while the local peaks in data acquisition (02/09 for example, or 09/09) are attributed to perturbations due to work on the site.
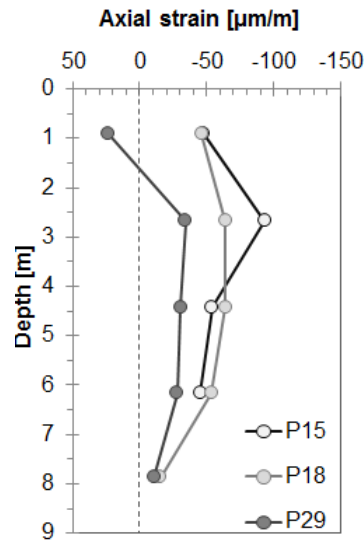
Figure 2-30 Axial strain profile when the pretreatment building was completed

It was expected that the maximum axial strain (Figure 2-30) would be observed near the top of the foundation and that this value would decrease with depth, as the load is transferred to the soil through side friction. However, for all three piles, the strain at 0.89 m is smaller than expected. This may be due either to residual loads from pile curing (Figure 2-25) or due to the effect of head restraints on the final load distribution at the pile head.

The axial strain values recorded at the end of each loading step, all along the pile are smaller than 100 µm/m, indicating that the pile behaviour rests in the elastic domain The elastic domain limit, in this case, was deduced using the method proposed in Eurocode 2 (AFNOR 2015) for C30/35 concrete which is equal to 460 µm/m (the elastic domain limit is set at $0.4 f_{cm}$ which in this case is equal to $0.4 \cdot 38 MPa = 15.2 MPa$ and elastic modulus E_{cm} is equal to $33 GPa$). The axial strain values variation along the pile as well as the fact that close to the pile toe the strain is close to zero suggest that most of the pile head load is transferred to the soil via mobilized friction on the pile shaft while a small amount of the load (less than 10% of the load) is supported by the pile toe.

2.4.3.2 The foundation behaviour before the geothermal activation

Seasonal variations in ground temperature and axial strain changes were recorded for a year prior to the operation of the GSHP system, as the office building designed to be heated/cooled using geothermal energy was completed and its exploitation started one year after the pre-treatment building. The pre-treatment building's construction ended in September 2016 and it was commissioned in November 2016.

The thermistors at different depths within each of the foundations were used to monitor temperatures in the foundations on an hourly basis, as shown in Figure 2-31 (a), Figure 2-32 (a) and Figure 2-33 (a) for piles P15, P18 and P29 respectively. The 12 months of non-geothermal monitoring from November 2016 to November 2017, reveal typical seasonal fluctuations with relatively large amplitudes of maximum and minimum pile temperature between summer and winter for all three instrumented piles. The recorded data indicate nonetheless a decrease in seasonal variability with depth and relatively constant temperature, of about 13°C below 5m with respect to the foundation level (about 8m with respect to ground level), similarly to previous observations found in literature (Laloui et al. 2003; Brandl 2006; McCartney and Murphy 2012b; Loveridge et al. 2016; Minh Tang et al. 2017). This temperature is higher than the recorded winter and spring atmospheric temperatures and lower than the summer and autumn atmospheric temperatures, confirming thus that ground can be used as a source of heat during winter and conversely a heat sink during summer. The temperature recorded at 0.89m with respect to the foundation level in pile P29 shows more variability compared to piles P15 and P18, which display very similar values. This may be due to the fact that pile P29 is situated under the storm tank; the temperature of the water temporarily stored in this tank may impacted the pile head's temperature.

The observed axial strains in this period were calculated from the total axial strain, by subtracting the axial strain due to the self-weigh of the structure, assumed to be equal to the observed strain at the moment of the pre-treatment building commissioning. Next, the zeroed strain values were corrected to account for the effect of the temperature on the VWSG (Eq. 2-4).

The resulting axial strain values evolution with time at different depths are presented in Figure 2-31 (b), Figure 2-32 (b) and Figure 2-33 (b) for piles P15, P18 and P29 respectively. In these figures positive strains indicate expansion while negative strains indicate compression.
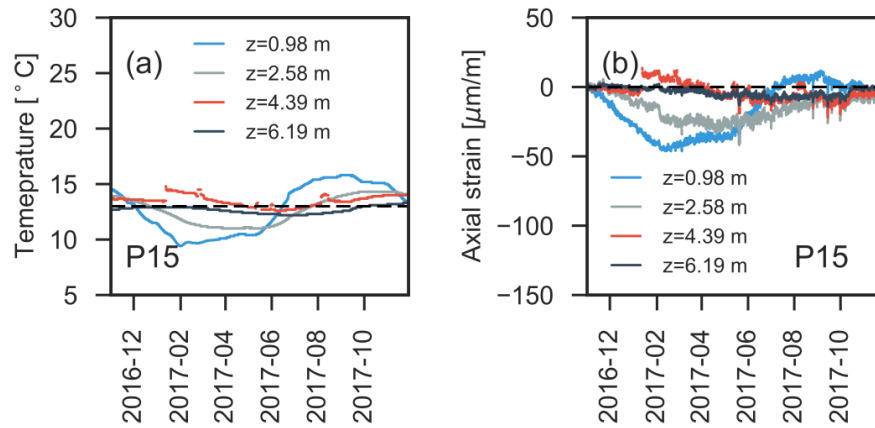
Figure 2-31 Pile P15: (a) Temperature evolution before the geothermal activation of the foundation, (b) Axial strain evolution before the geothermal activation of the foundation.

Figure 2-32 Pile P15: (a) Temperature evolution before the geothermal activation of the foundation, (b) Axial strain evolution before the geothermal activation of the foundation.

Figure 2-33 Pile P15: (a) Temperature evolution before the geothermal activation of the foundation, (b) Axial strain evolution before the geothermal activation of the foundation

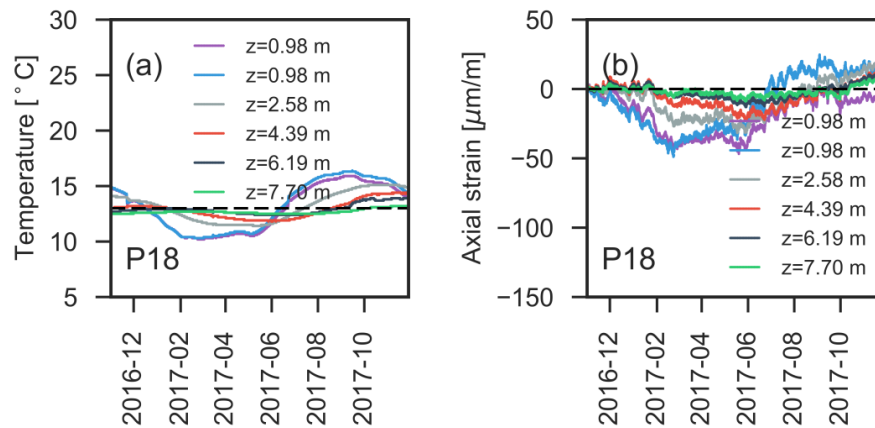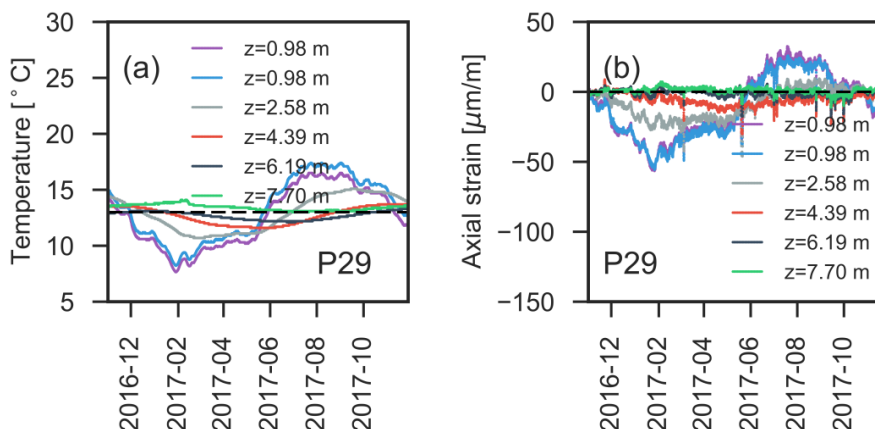It should be noted that the pre-treatment building is an industrial structure and some of the variable mechanical loads are non-negligible (such as the volume of water stored in the storm tank). Nevertheless, the impact of the variable mechanical loads is punctual

and it does not appear to influence the seasonal average strain values that visibly correspond to temperature variations. A decrease in temperature during the winter is followed by a decrease of axial strains (compression) while the increase in temperature in the piles during the summer corresponds to an increase of axial strains (extension). Only small, but non-negligible values of axial strains, ranging between $-56.5 \mu m/m$ to $32,5 \mu m/m$ were observed, indicated that the pile remains in the elastic domain.

The axial strain values decrease with depth for all three piles settling on average at $-1.5 \ \mu m/m$. While Piles P15 and P18, exhibit almost identical axial strain values, Pile P29 displays slightly higher axial strains, notably close to the pile head (sensor situated at 0.98m). This may be explained by the higher temperature variation or by the pile head boundary conditions. While the Pile 29 is situated under the slab (Figure 2-26), piles P15 and P18 are both under a lateral wall, providing a stiffer head constraint.

The thermal axial strains are presented as a function of temperature for all three instrumented piles in Figure 2-34, Figure 2-35 and Figure 2-36, for the different depth levels where instruments were installed. A linear correlation can be found between the axial strain and the change in temperature for each sensor. The variations around the slope correlating the temperature and the axial strain can be explained by the pile's response due to variable mechanical loads such as the variable water level in the tank. The slopes of the thermal axial strains versus the corresponding temperature change can be used to evaluate the mobilized Coefficient of Thermal Expansion (CTE) for the reinforced concrete at the depth of each of the VWSG, as summarized in Figure 2-34 (e), Figure 2-35 (f) and Figure 2-36 (f). If the building and the soil would not provide any restraint to movement, then the mobilized CTE would be equal to $10 \mu m/m/°C$ (AFNOR 2015). However, the results clearly show that all the strain gauges have a CTE smaller then this value, confirming the hypothesis presented in (Chapter 1.3.1). The CTE is closer to the free expansion at the top of pile P29 and decreases gradually along the pile's length indicating the increase of pile restraint. Piles P15 and P18 present the highest value of CTE close to their mid sections and smaller CTE values close to their ends reflecting both stiffer head restraint (the two piles support lateral walls, which may provide stiffer head restraint) and toe restraint. For all three piles though, the lowest level of mobilized CTE was found close to the pile tip, reflecting the fact that the piles are fixed in a stiff stratum.
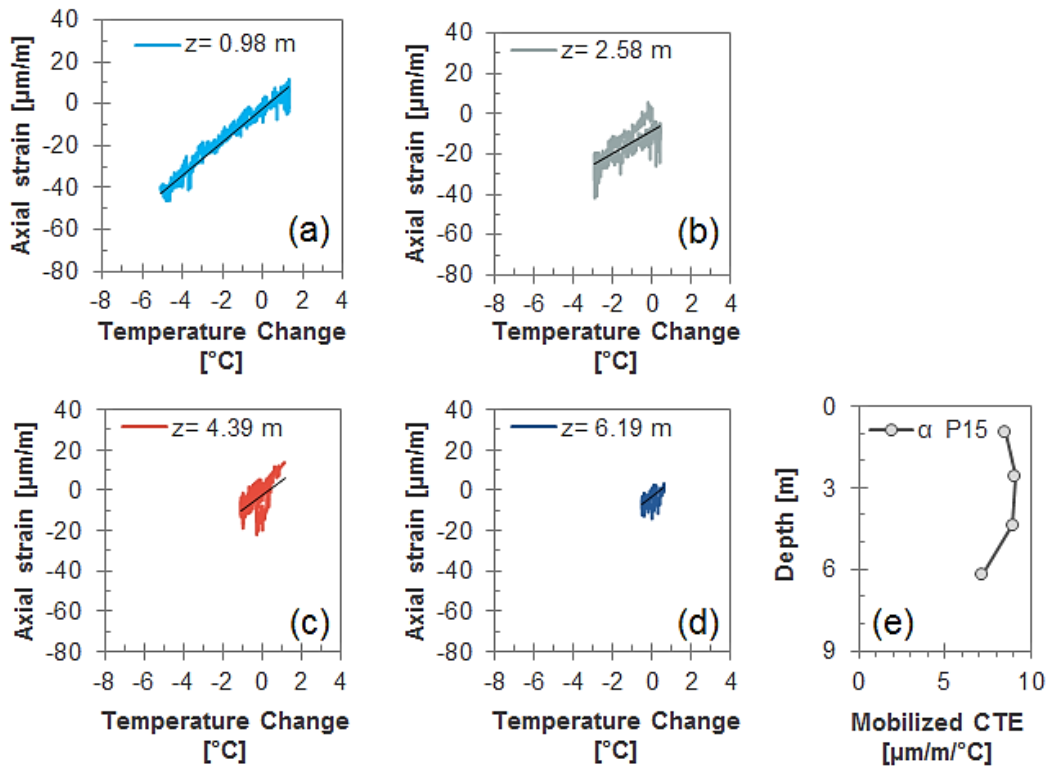
Figure 2-34 Evolution of CTE, Pile P15. Axial strain versus change in temperature for the VWSG situated at (a) 0.98m, (b) 5.58m, (c) 4.39m, (d) 6.19m. (e) Mobilized CTE with depth.
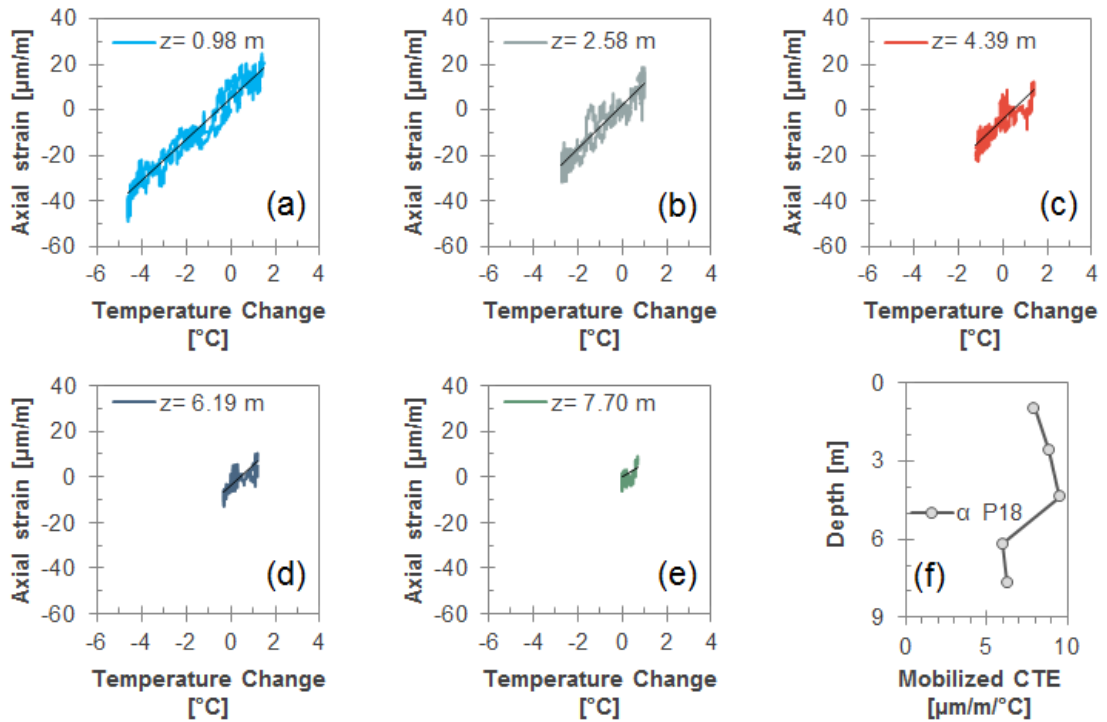
Figure 2-35 Evolution of the CTE, Pile P18. Axial strain versus change in temperature for the VWSG situated at (a) 0.98m, (b) 5.58m, (c) 4.39m, (d) 6.19m. (e) Mobilized CTE with depth.
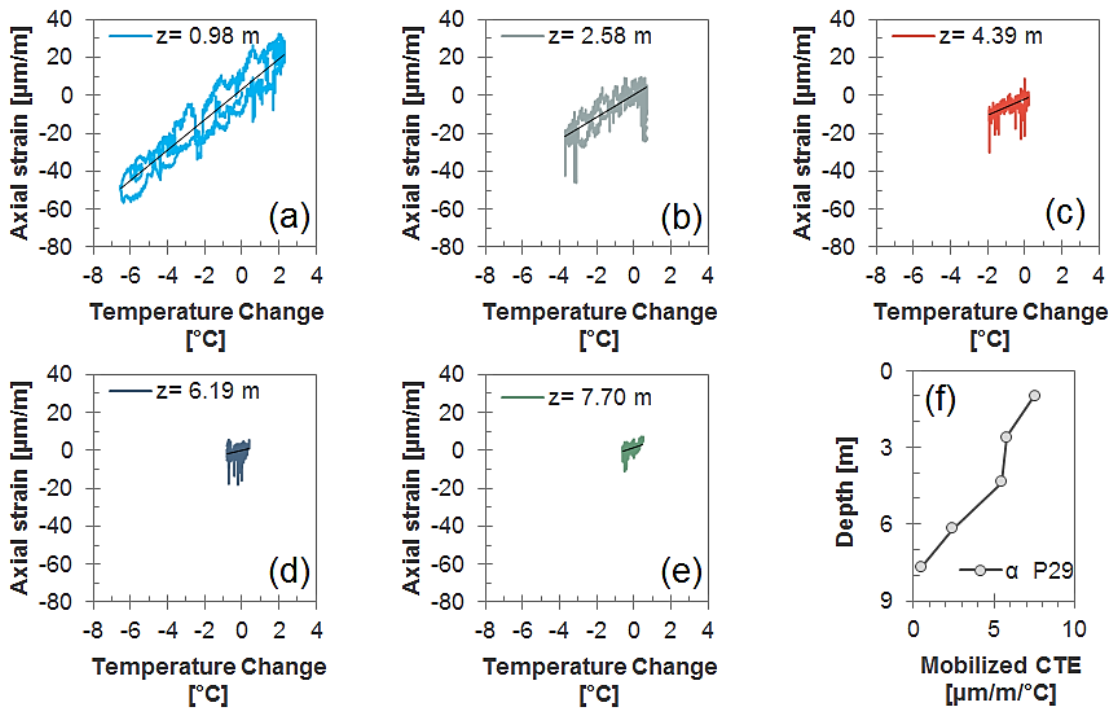
Figure 2-36 Evolution of the CTE, Pile P29. Axial strain versus change in temperature for the VWSG situated at (a) 0.98m, (b) 5.58m, (c) 4.39m, (d) 6.19m. (e) Mobilized CTE with depth.

2.4.3.3 Geothermal activation

The Water Treatment Plant's office building was completed and commissioned in the end of November 2017. The GSHP functioned from the 28th of November until the 10th of December and then it was stopped due to reparations being performed on the connection pipes. The GSHP also had to be stopped several times until the beginning of July 2018 due to the malfunction of one of the circulation pumps. From this point on the ground source heat pump system was used to cover 100% of the building's needs in heating and cooling. The temperature of the heat exchange fluid entering and exiting the foundation during the heat pump operation was monitored starting from April 2018 using PT100 temperature sensors. Due to a programming issue, data from the 13th of June until the 30th of August were lost.

The heat exchanger fluid temperatures as a function of time are presented in Figure 2-37 for the entire foundation (15 parallel groups each containing 3 energy piles connected in series). The heat exchange capacity of the foundation can be evaluated based on the temperature difference between the inlet and outlet fluid temperature (Figure 2-37 (c)). Thermal energy is extracted from the ground in order to heat the building during low temperature periods, by pumping a low temperature fluid in the heat exchange loops, which extracts heat from the ground and results in a higher outlet

temperature. Larger temperature difference between the inlet and outlet temperature reflect a higher amount of extracted geothermal energy.
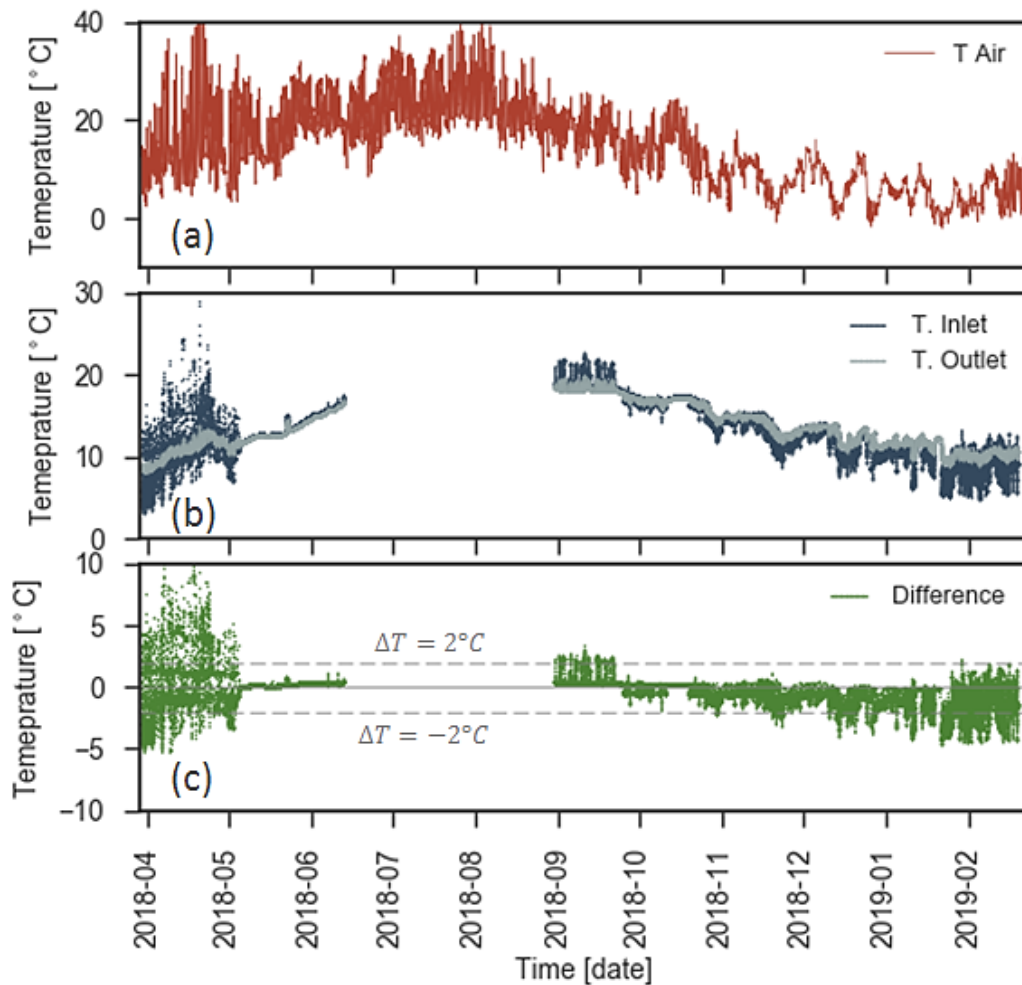
Figure 2-37 (a) Air temperature (b) Inlet and outlet heat exchanger temperature at the manifold level, (c) Temperature difference between the inlet and outlet temperature at the manifold level.

According to (Brandl 2006) a temperature difference greater than 2°C between inlet and outlet fluid temperature is sufficient for normal operation of the heat pump, as long as the ground temperature doesn't change significantly. Figure 2-37 (c) indicates an average temperature difference extracted of ~5°C, reflecting potential for good heat exchange. This difference is higher during extreme temperature periods. Figure 2-37 (a) indicates the air temperature evolution between the 29th of March and the 22nd of February. At first the air temperature sensor was placed on the West face of the building, directly exposed to the sun radiation, which may explain the very high temperature values recorded in April and May. The sensor was then protected from direct sun exposer and the recorded temperature corresponds to the average temperatures reported by Meteo France.
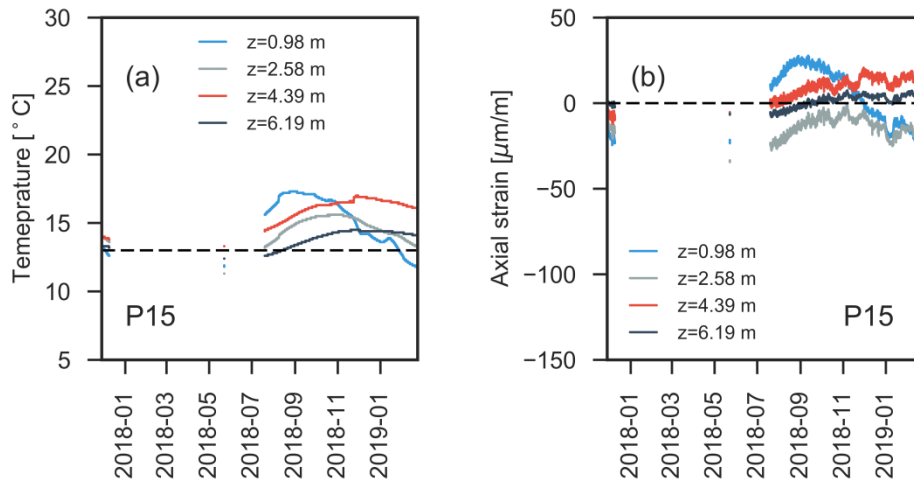
Figure 2-38 Pile P15: (a) Temperature evolution after the geothermal activation of the foundation, (b) Axial strain evolution after the geothermal activation of the foundation.
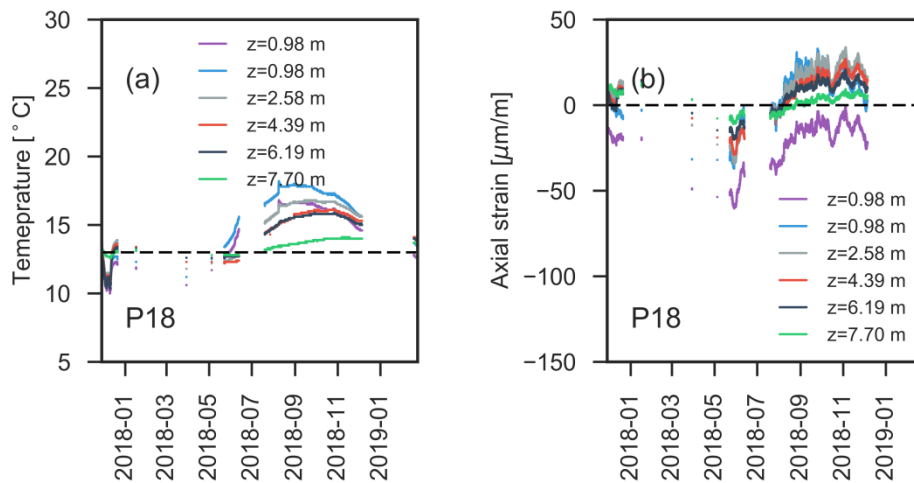
Figure 2-39 Pile P18: (a) Temperature evolution after the geothermal activation of the foundation, (b) Axial strain evolution after the geothermal activation of the foundation.
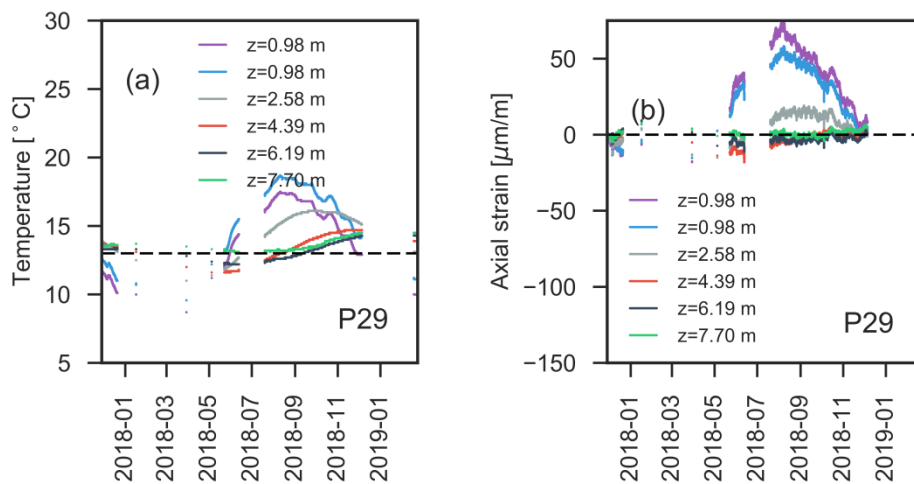
Figure 2-40 Pile P29: (a) Temperature evolution after the geothermal activation of the foundation, (b) Axial strain evolution after the geothermal activation of the foundation .

High temperature gradients were recorded in April and May 2018 which translate also in the GSHP system frequently transitioning between heating and cooling mode. In May and June 2018 the system was temporarily shut down in order to solve a malfunction of one of the circulating pumps, which explains the inlet, outlet temperature difference equal to zero during this period.

The thermistors and VWSG installed at different depths in each instrumented pile were used to record the temperature and axial strain evolution after the geothermal activation of the foundation with a frequency of 15 minutes. The results are presented in Figure 2-38, Figure 2-39 and Figure 2-40 for the classical pile P15 and for the geothermal piles P18 and P29 respectively. Once the heat pump operation started on the 28th of November 2017, the temperature distribution through the length of the Pile P18 became relatively uniform (Figure 2-39, Figure 2-41). The temperature sensor situated at 7.7m below the foundation level is placed under the level of the geothermal loops that measure only 7m, which explains why its temperature variation with time reveal only slight changes. The temperature sensor situated at 0.98m also exhibits some differences compared to the other sensors due to the impact of the ambient temperature. The temperature evolution in the pile P29 presents a variation with depth similar to the period before the geothermal activation. Moreover, its temperature variation is closer to the temperature variation observed in the pile P15 which is a classical pile (not equipped with geothermal loops). These observations led us to the conclusion that a problem occurred during the installation of the horizontal connections for this pile. The manifold for the entire group containing the pile P29 was closed in order to avoid fluid loss. Regardless of this group being closed, as can be observed from Figure 2-37, the ground source heat pump system operates within design parameters. Although rare, these incidents can occur and they have been foreseen in the design phase. In fact, a factor of safety of 0.25 was taken into account in the thermal design, resulting in adding 3 energy pile groups (9 equipped piles) more than strictly required by the design energy needs of the office building.

In order to decouple the behaviour of the foundation before the geothermal activation from its behaviour after the geothermal activation, all the strain values were zeroed at the moment when the geothermal heat pump was started. In these figures positive axial strains indicate expansion and negative axial strains indicate compression. Only small, but non-negligible values of axial strains, ranging between $-42.5 \mu m/m$ and $28.0 \mu m/m$ were observed, indicating that the pile remains in the elastic domain. These values are

comparable with the axial strain observed in the pile before the geothermal activation, the main difference after the geothermal activation being the axial strain profile. While before the geothermal activation the axial strains decreased with depth, after the start of the heat pump the axial strain distribution through the length of the energy pile P18 is relatively uniform. These values are consistent with the pile temperature evolution and are much lower than the concrete's elastic limit.
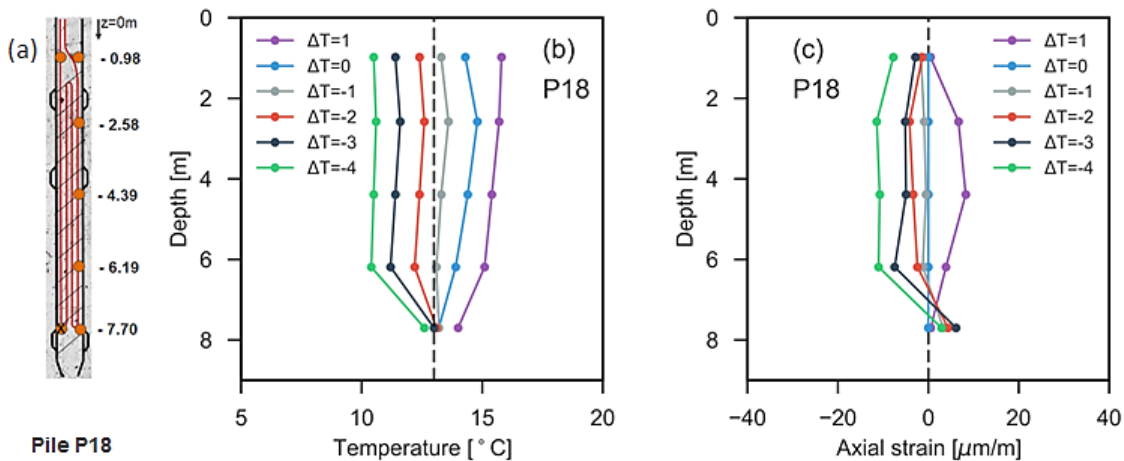
Figure 2-41 Pile P18: (a) Sensors Position, (b) Temperature profiles for different average changes in foundation temperature, (c) Axial strain profiles for different changes in average foundation temperature.

In order to better understand the effect of the temperature on the foundation response, instances on time when the energy foundation experienced average changes in temperature of 1°C increments were identified ($\Delta T = 1°C, 0°C, -1°C, -2°C, -3°C, -4°C$). The temperature at these instances is presented in fig Figure 2-41 (b). For the period of data collected in this study the maximum extent of temperature change corresponds to $\Delta T = -4°C$ during building heating and $\Delta T = 1°C$ during building cooling, with respect to the initial temperature (before starting the heat pump). As mentioned before, the temperature difference at the pile toe can be explained by the fact that the temperature sensor at 7.7m m is below the level of the geothermal loops, hence it is not impacted by the heat exchange. Its temperature remains therefore close to the undisturbed soil temperature. This value is also an evidence of the high concrete thermal inertia and suggests that the effect of thermal activation is limited to less than 1m below the geothermal loops.

The axial strain profiles corresponding to the abovementioned average changes in temperature are presented in Figure 2-41 (c). For the time instants corresponding to foundation cooling (building heating), axial contraction was observed as reflected by the

negative sign of the strain measurements. Conversely, during foundation heating (cooling of the building), positive values of axial strain were recorded, reflecting foundation extension. The shapes of these profiles reflect the pile's boundary conditions: the pile has stiff head and toe restraint which restricts its deformation during heating. During, cooling, the effect of the toe restraint is less important, since the pile is contracting. Another observation is that the thermal deformation is much smaller than predicted by academic in-situ tests (Laloui et al. 2006; Bourne-Webb et al. 2009; Sutman et al. 2018) and even by the Denver, CO, USA case study which presents long term behaviour of two energy piles under exploitation conditions (McCartney and Murphy 2012b; Murphy and McCartney 2015; McCartney and Murphy 2017). This may be explained by the lower heating/cooling requirements of the new office building, insulated according to the RT 2000 standards.
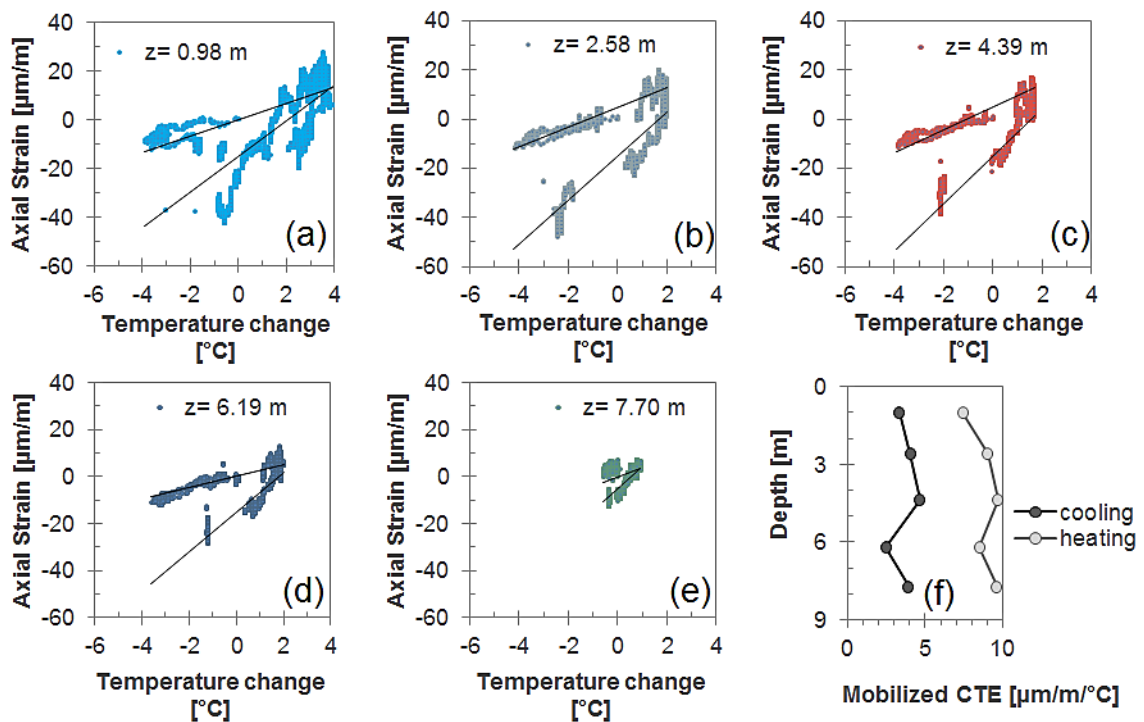
Figure 2-42 Evolution of the CTE after the geothermal activation of the foundation, Pile 18. Axial strain versus change in temperature for the VWSG situated at (a) 0.98m, (b) 5.58m, (c) 4.39m, (d) 6.19m. (d) Mmobilized CTE with depth.

The ground source heat pump system was active at the end of November 2017; hence the energy piles first underwent a cooling cycle (building heating) during the cold season, followed by a heating period (building cooling) during the summer and autumn of 2018. The thermal axial strain behaviour as a function of temperature change for the geothermal pile P18 is presented in Figure 2-42. Hysteresis is noted in the strain measurements during cooling and heating of the foundation. McCartney and Murphy

(2012b) mention that due to the rapid temperature fluctuations specific to energy geostructures the assumption that the temperature recorded by the thermistors is equal to the temperature of the mass of concrete may no longer be accurate (because of the insulating effect of the air surrounding the steel wire within the VWSG). Hence, the temperature change in the pile may be different. For pile P18 though, the pile's temperature change occurs over the duration of several days. Another possible explanation for the differences in the foundation's response to cooling and heating may be credited on the effect of temperature changes on the soil-pile interface.

2.4.4 Discussion

To better understand the behaviour of energy foundations during building operations, this study presents the results of an instrumented energy foundation designed to cover 100% of the heating and cooling needs of a 340m2 office building, in operation since the end of November 2017.

Data recorded during pile curing, from one of the three instrumented piles (Figure 2-28, Figure 2-29), indicate that the concrete hardening in saturated conditions may lead to positive (extension) axial strains over a period of time longer than four months (August –November), which in turn may lead to initial tensile axial strains in the foundation.

Figure 2-43 presents a comparison of average seasonal variations in temperature and axial strain values with depth. In order to facilitate the comparison, the same time intervals were selected for the geothermal and the non-geothermal exploitation of the foundation to calculate average temperature and axial strain values: End of Autumn 2016 and End of Autumn 2017 represent the period between the 28th of November and the 10th of December 2016 and 2017 respectively (the first period of geothermal activation); Summer 2017 and Summer 2018 represent the average values of temperature and axial strain in July 2017 and July 2018; Autumn 2017 and Autumn 2018 represent the average temperature and axial strain In November 2017 (before the start of the GSHP) and November 2018; Winter 2017 and Winter 2019 represent the average values from February 2017 and February 2019 respectively.

The results after one year of classical (non-geothermal) exploitation of the pre-treatment building foundation illustrate the fact that daily and seasonal thermal variations are present in the first 5m (Figure 2-43 (a)) of the piles (the foundation level is at -3m with respect to the ground level) due to air temperature variations. The amplitude as well as the temperature distribution in the piles is congruent with previous observations

reported in the literature (Brandl 2006; McCartney and Murphy 2012a). These temperature variations lead to small but not negligible cyclic strains in the foundation that may be of the same order of magnitude with the strains due to the structure's dead load (Figure 2-30, Figure 2-43 (a)). The total strain remain nonetheless well within the concrete's elastic range.
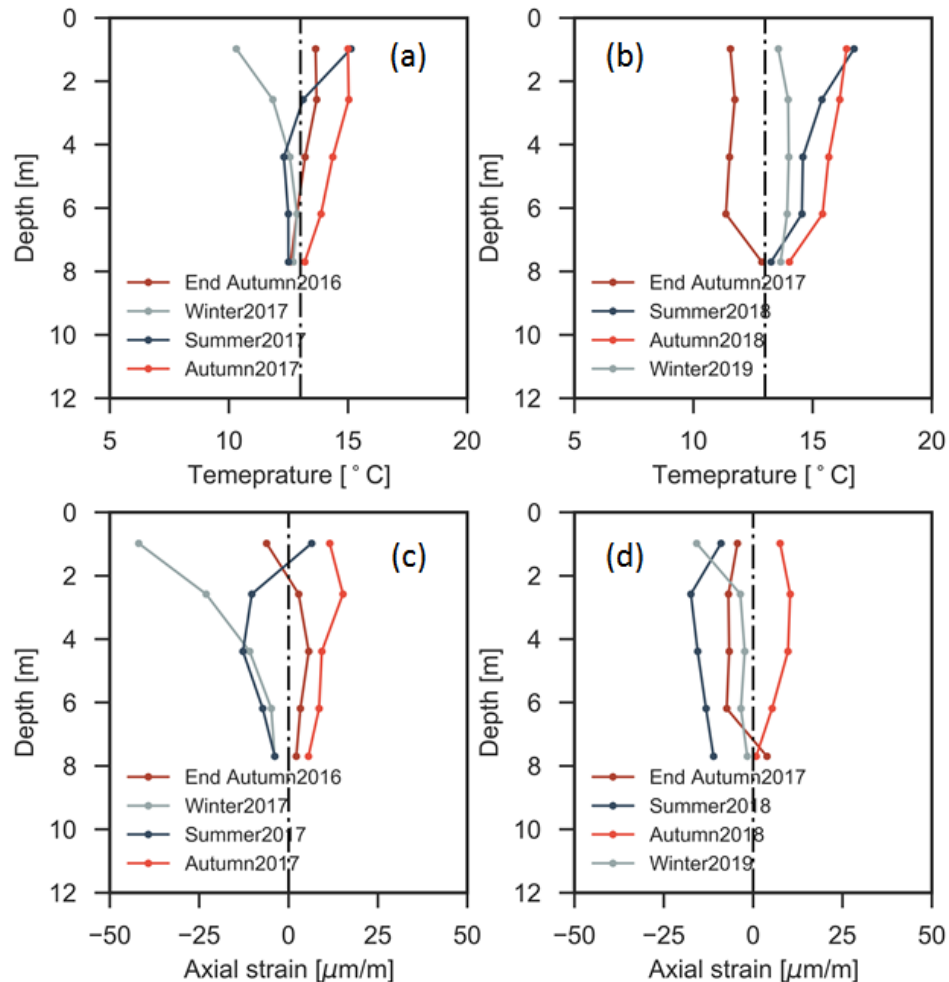
Figure 2-43 Comparison between the pile P18's behaviour before and after its geothermal activation: (a) Average temperature variation with depth for different seasons before the geothermal activation, (b) Average temperature variation with depth for different seasons after the geothermal activation, (c) Average axial strain variation with depth for different seasons before the geothermal activation, (d) Average axial strain variation with depth for different seasons after the geothermal activation.

The foundation geothermal activation leads to temperature variation over the entire equipped (with geothermal loops) foundation length (compared to the non-geothermal period where the temperatures decrease with depth to reach a constant value below 5m with respect to the foundation level, ~8m with respect to the ground level, of 13°C). The recorded temperature variation in the foundation was between -3.9°C and +1.9°C, a similar order of magnitude with the maximum and minimum temperature

variation recorded close to the pile head (at 0.98m) during the classical (non-geothermal) exploitation period (maximum heating of +1.5°C and minimum cooling of -4.6°C with respect to the beginning of November 2016 when the operation of the pre-treatment building started).

The temperature range recorded in the pile P18 after the geothermal activation reveals a smaller temperature variation in the pile than those described in the literature (Laloui et al. 2006; Bourne-Webb et al. 2009; McCartney and Murphy 2012b; Murphy and McCartney 2015; Sutman et al. 2015; Abdelaziz and Ozudogru 2016; McCartney and Murphy 2017). This may be explained by the pile and the soil's thermal inertia and by the fact that the ground source heat pump doesn't have a continuous operation but follows the building's energy demands, thus the imposed thermal loads have a relatively small application time (Figure 2-37 (b)).

The axial strains developed in the foundation after the geothermal activation are also small but non-negligible (Figure 2-43 (d)) and of a similar order of magnitude as the maximum strains detected before the geothermal activation. The axial strain values should however be interpreted with caution, keeping in mind that the pre-treatment building is an industrial facility and some of the axial strain variations may be explained by the variable mechanical loads such as changes of the water level in the storm tank. Nonetheless, a good correlation was found between the temperature variation and the axial strain, as illustrated in Figure 2-42.

2.4.5 Conclusions

The Sept Sorts case study is about the behaviour of an energy foundation for one year before and one year after its geothermal activation. The results obtained confirm the feasibility of this foundation method for meeting both the building's structural and heating/cooling needs. The main conclusions from the data analysis are:

- Daily and seasonal cyclic temperature variations were recorded up to 5m below the foundation level (~8m with respect to the ground level), after which the temperature of the soil is relatively constant and equal to 13°C
- The recorded dayly and seasonal temeprature variations lead to the development of small but not negligible axial strains along the instrumented piles. The values of the recorded axial strains remain nonetheless well within the concrete's elastic limit

- During the circulation of the fluid with temperatures ranging between 3.5°C and 30°C through the closed loop circuit within the foundation, the temeprature of the reinforced concrete ranged between 16.8°C and 12.3°C and was relatively uniform with depth, with the exception of the pile head sensor (0.98m) that was slightly impacted by the ambiant temperature variation and the pile toe sensor (7.70m) (0.7m below the lower limit of the geothermal loops, hence less impacted by the geothermal activation)

- The thermal axial strains due to the geothermal activation of the foundation are comparable in magnitude to the values recorded before the start of operation of the ground source heat pump. The axial strain profile within the length of the foundation is however more uniform. The recorded values are small and rest within the concrete's elastic limit

- A change in the mobilized coefficient of thermal expansion appears to occur after the first cooling phase. More data are however necessary in order to identify the reason why this happened

Overall, the results obtained after more than two years of observations (one year before and one year after the geothermal activation of the foundation), indicate that the magnitude of temperature and axial strain measured in energy piles are within acceptable limits.

3. LABORATORY STUDY OF THE EFFECT OF TEMPERATURE ON THE SOIL-PILE INTERFACE

The geothermal exploitation of a pile foundation leads to expansion-contraction cycles both in axial and radial directions influencing the soil-pile interactions. The knowledge of the axial pile displacements and strains is growing thanks to the increasing number of full-scale experiments (Laloui et al. 2003; Brandl 2006; Bourne-Webb et al. 2009; Martin et al. 2010; Singh et al. 2011; McCartney and Murphy 2012b; Sutman et al. 2015; Loveridge et al. 2016; Olgun and Bowers 2016; You et al. 2016). The effects of temperature variation on the soil–pile interface have been however less investigated up to now (Xiao et al. 2014; Di Donna et al. 2016; Yavari et al. 2016a; Xiao et al. 2017).

In the previous chapter, it was not possible to experimentally investigate the interface response of the two in-situ tests. This chapter investigates the soil-pile interface behavior due to temperature variations in the laboratory. Two of the most commonly encountered sand types (silica sand and carbonate sand) and a clay soil (Green Clay from Marne La Vallée) are used. Their thermomechanical behavior is investigated along a concrete plate to simulate a (simplified) soil-pile interface. Results concern mainly the sand-pile interface as only a preliminary investigation proved feasible for the Green Clay due to the high heterogeneity of the soil in the available boreholes.

After a short review of the state of the art, the new experimental campaign is presented focusing on a novel experimental device and the effect of temperature cycles on the soil-pile (concrete) interface.

3.1 Background

The term soil-structure interface refers to a thin soil zone, at the contact between a structure (i.e. the pile) and the surrounding soil, where strain localization occurs caused by the transmission of a tangential force from the structure to the soil (Boulon 1989). Its thickness is considered to vary between 5 and 20 times the average particle diameter, depending on the soil and structure's characteristics (Pra-Ai 2013). An extensive

amount of literature is available on this topic resulting both from laboratory and in-situ tests. These results point to the fact that the main factors to be considered in the evaluation of the soil-structure interface are: the initial state (normal stress and soil density), the particle characteristics, the soil gradation and the surface roughness (Desai et al. 1985; Uesugi and Kishida 1986; Kishida and Uesugi 1987; Boulon and Nova 1990; Al-Douri and Poulos 1992; Tsubakihara et al. 1993; Tabucanon et al. 1995; Mortara et al. 2007; DeJong et al. 2009).
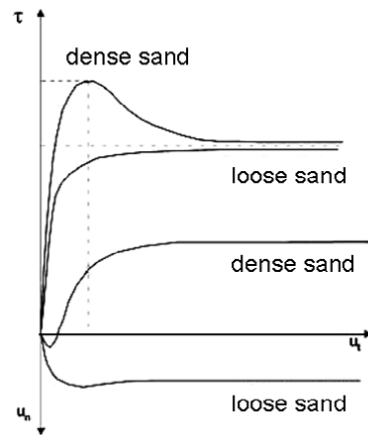
Figure 3-1: Typical constant normal loading interface direct shear test response (Said 2007).

*where τ represents the shear stress, u_t represents the horizontal (shear) displacement and u_n represents the vertical (normal) displacement

As in the case of soil testing, the soil-structure interface tests (Lerat; HASSAN 1995; Fakharian and Evgin 1997; DeGennaro and Frank 2002; Ghionna and Mortara 2002; Hu and Pu 2004) show that the higher the effective normal stresses to the interface, the higher the interface shear strength (Di Donna 2014, Eq. 1-1).

$$\boldsymbol{\tau = \sigma \, tan(\delta)}$$ **Eq. 3-1**

where τ is the interface shear stress, σ the stress normal to the surface and δ the interface friction angle.

For granular materials the soil density influences the soil-structure interface behaviour as it is responsible for the volumetric response of the soil. Dense sandy interfaces show dilatancy, while loose sandy interfaces present a contractive response (Pra-Ai 2013). In the case of clayey interfaces, the response is generally contractive, with the exception of highly overconsolidated conditions (Shakir and Zhu 2009; Di Donna 2014).

According to DeJong et al. (2009) the particle material properties that affect the interface behaviour can be separated in two categories : single particle properties and

particle assembly (i.e. soil grading). The single particle properties are the particle hardness and the particle angularity both derived from the particle mineralogy. Strong angular particles may undergo similar particle breakage during shear as weak rounded particles due to increased particle interlocking (Uesugi and Kishida 1986). Concerning the soil grading, the mean grain diameter determines if the particle interlocks, rotates or translates laterally along an interface surface (Uesugi and Kishida 1986). The potential of particle crushing increases with increasing mean particle size (DeJong et al. 2009) that also influences the thickness of the shear zone: the higher the D_{50} (the average particle diameter by mass) the higher the thickness (Uesugi and Kishida 1986; Fioravante et al. 1999; DeJong et al. 2006).
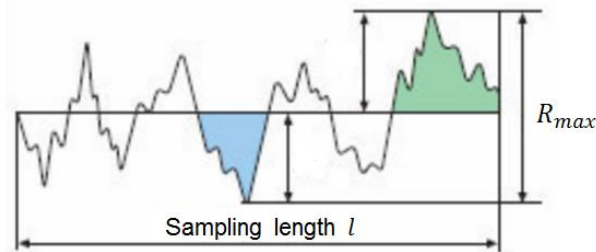
Figure 3-2: Evaluation of surface roughness

Previous experimental investigations (Kishida and Uesugi 1987; Boulon 1989; Tsubakihara et al. 1993; Mortara et al. 2007) found that surface roughness is a major factor affecting the soil-structure interface response. In order to correlate the surface roughness with the soil properties, a normalized roughness is defined as follows (Eq. 3-2):

$$R_n = R_{max}/D_{50} \hspace{3cm} \text{Eq. 3-2}$$

where: R_{max} is the relative height between the highest and the lowest peaks over a surface profile of defined length and D_{50} is the sieve diameters corresponding to 50% of material passing.

The normalized roughness is used to classify the surface as smooth or rough, based on a limit R_{crit} critical roughness value. Available investigations (Uesugi and Kishida 1986; Hu and Pu 2004) place critical surfaces roughness in the range of $0.1 - 0.13$, i.e. for $R_n < R_{crit}$ the surface is classified as smooth, whereas $R_n > R_{crit}$ indicate a rough interface (Pra-Ai 2013). As Hu and Pu (2004) among others (Uesugi and Kishida 1986; Kishida and Uesugi 1987; Tsubakihara et al. 1993; Tabucanon et al. 1995; Pra-Ai 2013; Di Donna 2014) point out, the interface shear resistance is higher

for rough than smooth interfaces (Figure 3-3). Porcino et al. (2003) , report that the interface friction is limited by the soil's internal friction angle, that the volumetric deformation of the soil-structure interface test samples is lower than that of sand-sand samples and that the dilative behaviour is less pronounced when the interface roughness decreases.
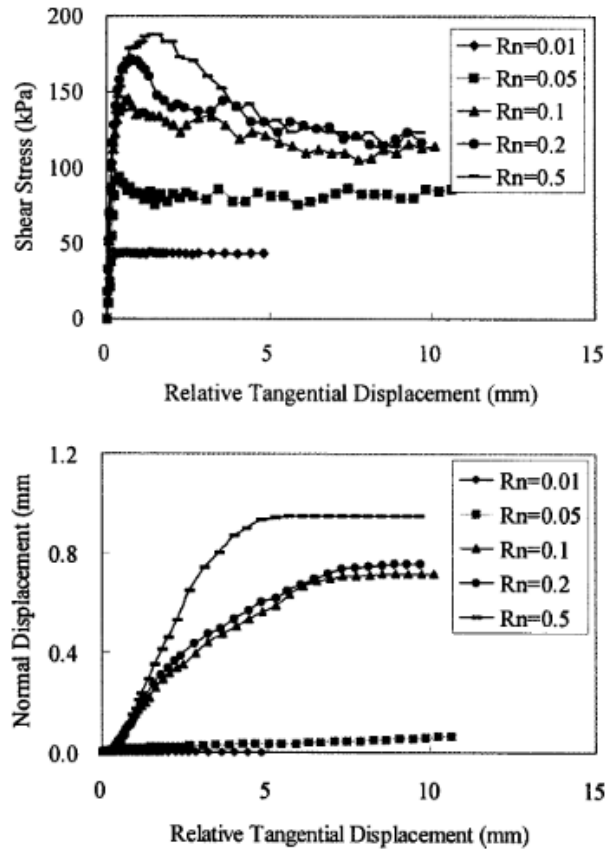
Figure 3-3: Influence of surface roughness on interface response: (a) shear stress development during CNL interface direct shear test, (b) normal displacement during CNL interface direct shear test (Hu and Pu 2004).

Starting from the observations regarding the surface roughness and its relation to the soil type, Tsubakihara et al. (1993) propose a classification of the sand-pile interface behaviour into three failure modes: (i) Mode 1 when the interface surface is rough and shear failure occurs in the soil, (ii) Mode 2 when the interface surface is smooth and full sliding occurs at the interface and (iii) Mode 3 when shear failure and sliding displacement occur simultaneously (Figure 3-4). These observations are also confirmed by (DeJong et al. 2006) by particle image velocimetry, an image based deformation measurement.

Although, as previously mentioned, a lot of research has been carried out in the past fifty years to study the soil-structure interface, most available results disregard the possible effect of the temperature or of the temperature variation. Several studies

however (Williams and Gold 1977; McCartney and Murphy 2012a; Vasilescu et al. 2019) prove that not only energy geostructures but also some conventional geostructures are subjected to some extent to temperature variations as a result of the daily and seasonal temperature variation that can be expected up to five meters deep.
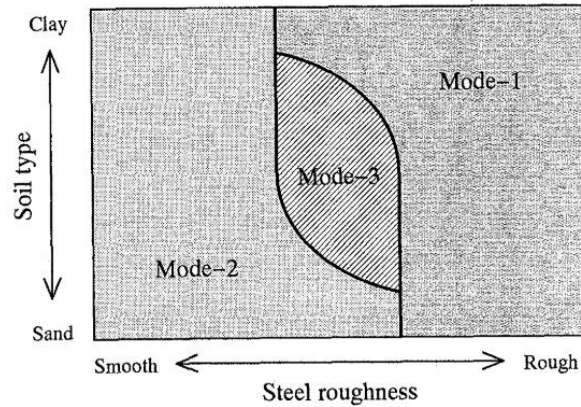
Figure 3-4: Idealized classification into three failure modes (Tsubakihara et al. 1993).

Focusing on the response of the soil-pile interface, Xiao et al. (2014), Di Donna et al. (2016), and Yavari et al. (2016) performed direct shear tests to explore the effect of the temperature changes and Xiao et al. (2017) investigated the effect of temperature cycles on a disturbed natural soil-concrete interface in unsaturated conditions. For a saturated clay-concrete interface, Di Donna et al. (2016) showed an increase of the interface shear strength due to heating, which may be explained by thermal consolidation. Yavari et al. (2016) showed that the temperature effects on the friction angle and adhesion are minor and the results of Xiao et al. (2014) showed a slight decrease of adhesion of the soil-concrete interface when subjected to cooling and negligible effects on the friction angle for unsaturated soil conditions. Xiao et al. (2017) also pointed out that after 10.5 temperature cycles an increase of the interface shear strength as well as an increase of adhesion (in the case of large heating cycles) was detected for sandy silty clay-concrete interface, mostly attributed to water migration due to the temperature changes.

Even though energy piles can be used regardless of the degree of the soil saturation, the geothermal activation of the foundation is more efficient when the soil is saturated (i.e. the entire pile or part of it rests below the ground water level). In this case saturated conditions, or at least submerged conditions, are required to investigate the behaviour of soil-pile interfaces at the laboratory scale.

The study presented in this thesis investigates the effect of temperature cycles on the soil-structure interface under submerged conditions in a large direct shear box of $100mm x 100\ mm$ adapted for thermomechanical loading.

3.2 Materials

3.2.1 The concrete plate

As indicated previously, C30/37 concrete with maximum aggregate size of 10 mm is recommended for curing energy piles. For the purpose of this study the most influential parameter is the surface roughness, while the material resistance is of secondary importance. For practical reasons, the concrete structure used in the interface shear tests was not prepared using the concrete mix used in-situ, but rather using materials available in the laboratory. The concrete was prepared in the laboratory by mixing CEM I 52.5 N CE CP2 NF-23-01-12 cement, limestone filler, sand (0 -4mm) and aggregates (6-10mm) according to a mix design based on Eurocode 2. The concrete mix is presented in Table 3-1.

Parameter	Value
Cement	$300\ kg/m^3$
Sand	$705\ kg/m^3$
Aggregates	$950\ kg/m^3$
Limestone filler	$210\ kg/m^3$
Water	$212\ kg/m^3$

Table 3-1: Concrete mix design.

Figure 3-5 (a) shows the centimeter-size aggregates within the cement on the concrete plate chosen for the experiment. A surface of 20x20mm² was mapped under a 3D microscope to have a macroscopic view of the plate's roughness (Figure 3-5 (b)). Several pieces of concrete with a thickness of $11\ mm$ were cut and fixed at the bottom of the shear box (Figure 3-8). The mechanical properties of this concrete are listed in Table 3-3.
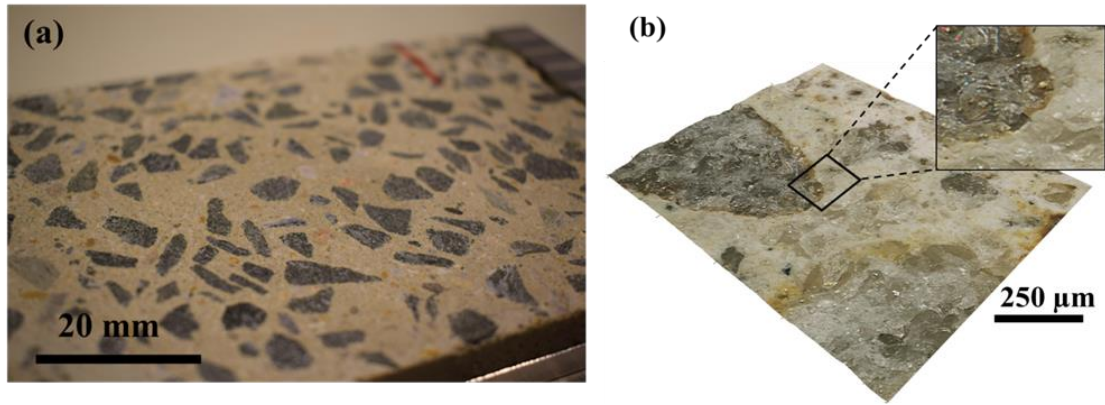
Figure 3-5: (a) Optical macro view of the concrete plate used in the experiment; (b) 3D microscope image of the surface of the concrete plate.

Roughness measurements performed with a superior surface roughness tester were acquired before and after the tests. The normalized roughness values employed for this study are presented in Table 3-2. The value of the maximum vertical distance between the highest and the lowest peaks of the structure's asperities over a fixed length (R_{max}) varied between $89 \mu m$ an $97 \mu m$ before and after the Fontainebleau sand tests. Since the roughness value did not change substantially after test, the same plate was used for the subsequent carbonate sand tests. The carbonate sand test did not alter to an important extent the plate's roughness either: R_{max} before test was found equal to $97 \mu m$ and $90 \mu m$ after test. A second plate having the same composition and R_{max} was used for the clay experiments.

	R_{max}	R_n	Roughness
Fontainebleau Sand Test	89 μm	0.42	Medium
Carbonate Sand Test	97 μm	0.07	Smooth
Green Clay Test	86 μm	$\gg 10$	High

Table 3-2 Normalised roughness.

It is difficult to measure the cast in place piles in-situ surface roughness but it is safe to assume an average value constant over the pile's entire length. The normalized roughness value (Eq. 3-2), which correlates the surface roughness with the soil properties, on the other hand, points to the fact that even if the pile has a constant R_{max} may exhibit different surface roughness depending on the different soil layers it is embedded in (Table 3-2). For this reason the R_{max} roughness of the concrete plates used for the interface direct shear tests in this study was set constant.

Property	Value
Density	$2500 \ kg/m^3$
Compressive strength	$33.9 \ MPa$
Tensile strength	$2.8 \ MPa$
Young Modulus	$44.4 \ GPa$
Shear Modulus	$17.9 \ GPa$
Poison's coefficient	0.24

Table 3-3: Mechanical properties of the concrete used for the plates.

3.2.2 The NE34 Fontainebleau sand

Fontainebleau sand NE34 (Sibelco company) was used in this study for its high quartz content (99% quartz) (Figure 3-6 (b)). The literature review (Di Donna et al. 2016; Yavari et al. 2016a) shows that the temperature effect on sand is negligible. However, this choice of soil was made in order to evaluate the performance of the testing device recently acquired in our laboratory and the repeatability of the testing procedure.
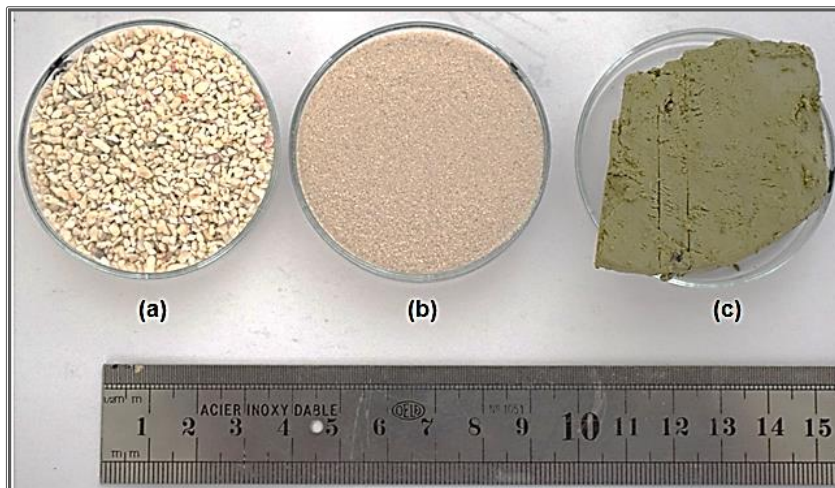
Figure 3-6: (a) Carbonate sand (b) Fontainebleau sand, (c) Green Clay.

The physical properties of Fontainebleau sand are presented in Table 3-4, where C_u is the coefficient of uniformity, D_{10} and D_{50} are the sieve diameters corresponding to 10 and 50% of material passing and ρ_s is the grain density. As it can be noticed from Figure 3-7 the grain size is mainly included in the range of 100 μm to 400 μm (Figure 3-7). The grain size distribution was determined by laser granulometry method. All the specimens (both for sand-sand and sand – concrete tests) were prepared by dry tamping, with an initial target dry density of about 1.7 g/cm^3, corresponding to dense sand. For the tests in saturated conditions, demineralized water was added in the interface direct shear test device's container after the vertical loading step. Detailed

properties of the obtained tested specimens are presented in the corresponding results sections.

Parameter	Value
C_u	1.7
D_{10}	0.13
D_{50}	$0.21\ mm$
ρ_s	$2.65\ g/cm^3$
λ	$3.4\ W/m°C$
C_v	$2475\ kJ/m^3°C$

Table 3-4 Fontainebleau sand's main properties
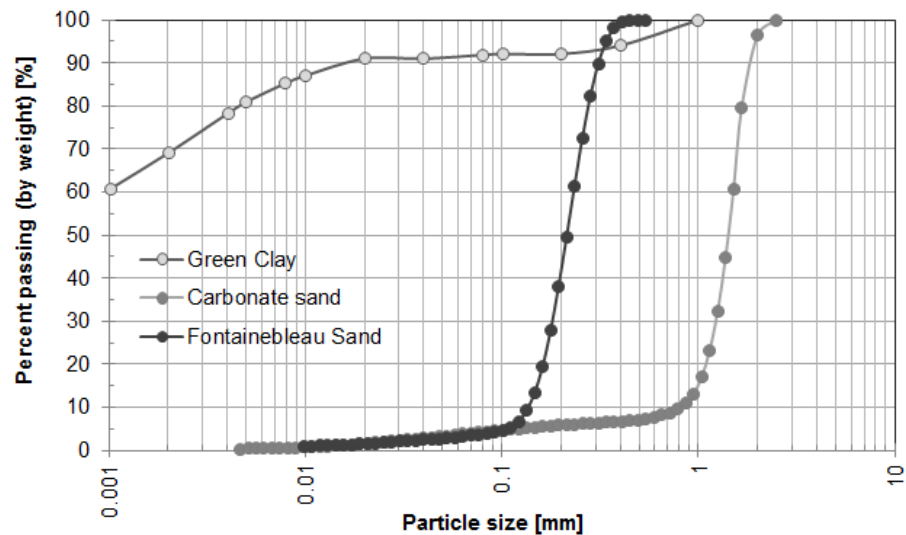
Figure 3-7: Fontainebleau sand, Carbonate sand and Green clay grain size distribution.

3.2.3 The Carbonate sand

The composition of sand varies depending on the local rock sources and depositional conditions, but the most common constituents of sand in inland continental setting is silica (silicon dioxide), usually in the form of quartz. The second most common type of sand is calcareous sand which is formed by the accumulation of pieces of carbonate materials, that originates from shell fragments and skeletal debris of marine organisms (Wang et al. 2011).

Carbonate sand from South China Sea (Figure 3-6 (a)) was used to assess the effect of temperature cycles on the soil-structure interface. The available material is disturbed and uncemented and was obtained by mixing already segregated grain size samples. The grain size distribution, obtained by laser granulometry is presented in Figure 3-7. The content of calcium carbonate exceeds 97% and the main mineral

components are aragonite and magnesium calcite (Wang et al. 2011). Most of the particles are dendritic and crushable. The physical properties of carbonate sand are presented in Table 3-5.

Parameter	Value
C_u	1.45
D_{10}	1.09
D_{50}	1.35
ρ_s	$2.76 \; g/cm^3$
λ	$1.07 \; W/m°C$
C_v	$3140 kJ/m^3°C$

Table 3-5: Carbonate sand's main properties.

All the specimens were prepared by dry tamping, with an initial target dry density of about 1.35 g/cm^3 (loose sand). All the tests were realized in saturated conditions, for which demineralized water was added in the interface direct shear test device's container after the vertical loading step. As mentioned above, calcareous sand particles are crushable, furthermore, unrecoverable relative slip is easy to occur between contiguous particles and the edges and corners are apt to crush under loading. Detailed properties of the obtained tested specimens are presented in the corresponding results sections.

3.2.4 The Green Clay

The clayey soil selected is green clay (Romainville green clay) sampled from the in-situ experimental site from Ecole des Ponts Paris Tech, Paris (Figure 3-6 (c)). The Green Clay presents a fine fraction of (particles diameter<0.08mm) of 92% (Figure 3-7, after (Mantho 2005)).

Parameter	Value
ρ_s	$2.76 \; g/cm^3$
k	$4E-8 \; m/s$
w_L	95
w_P	31
I_P	54
λ	$1.1 \; W/m°C$
C_v	$2475 \; kJ/m^3°C$

Table 3-6: Green clay's main properties.

This material is mainly composed of illite and smectite (Nguyen 2017). The main properties are summarized in Table 3-6, k is the hydraulic permeability, w_L and w_P are the liquid and plastic limits and I_P the plasticity index. Detailed properties of the obtained tested specimens are presented in the corresponding results sections.

3.3 Experiment campaigns on a new interface direct shear device adapted for thermo-mechanical loading

3.3.1 Description of the experimental device

The device used to carry out the experiments is an interface direct shear box, with a square section, adapted for thermo-mechanical tests (Figure 3-8). The normal and shear forces are controlled by two electromechanical force actuators, which are used to control the tests either in displacement or force. A load cell is installed on each actuator in order to accurately measure both the vertical and horizontal loads applied on the sample. Two Linear Variable Displacement Transducers (LVDTs) are used to measure the horizontal and vertical displacements. The square shear box is divided in two parts, subsequently referred to as upper part and bottom part. This box is installed in a container that can be filled with water for testing saturated samples. The upper part can accommodate $100 \, mm \, x \, 100 \, mm$ soil specimens with a maximum initial height of $50 \, mm$. The bottom part can accommodate $140 \, mm \, x \, 100 \, mm \, x \, 11mm$ soil specimens or structural elements and is fitted with a temperature sensor in its lower part. The device was designed for constant volume (e.g. fixed normal displacement) and constant normal load vertical loading and it allows choosing between shear load-controlled mode and a shear displacement-controlled mode both for monotonic and for cyclic tests. The frequency for the cyclic test option ranges between $0 \, and \, 5 \, Hz$ and the maximum amplitude at the highest frequency is of $\pm 1 \, mm$.

The thermal loading is applied through a closed loop circuit, that passes through a system installed under the container accommodating the shear box and that is connected to a refrigerated heating circulator bath with air-cooled cooling machine (Huber Ministat 125). The high precision thermoregulation system is equipped with one Pt100 internal temperature sensor and one Pt100 sensor external connection, in which the bottom temperature sensor is plugged-in. The temperature in the tested specimen is measured through the above mentioned Pt100 temperature sensor installed in the bottom of the lower shear box (Figure 3-8) which is also used for piloting the temperature tests and a top Pt100 temperature sensor installed in the piston, used to measure the

temperature on the superior part of the sample. The allowable temperature range was set between $5\ and\ 50°C$.

Figure 3-8 : Interface direct shear device adapted for thermo-mechanical loading (a) Loading frame, (b) Refrigerated heating circulator bath with air-cooled cooling machine, (c) Container holding the lower box containing a concrete plate.

Sensor	Operating range	Accuracy
Vertical load cell	$0 - 10\ kN$	0.1%
Horizontal load cell	$0 \pm 5\ kN$	0.1%
Vertical LVDT	$\pm 5mm$	0.1%
Horizontal LVDT	± 12.5	0.1%
Pt100	$0 - 50\ °C$	0.2 ℃

Table 3-7: Sensors characteristics.

The thermal loading is applied through a closed loop circuit, that passes through a system installed under the container accommodating the shear box and that is connected to a refrigerated heating circulator bath with air-cooled cooling machine (Huber Ministat 125). The high precision thermoregulation system is equipped with one Pt100 internal temperature sensor and one Pt100 sensor external connection, in which the bottom temperature sensor is plugged-in. The temperature in the tested specimen is measured through the above mentioned Pt100 temperature sensor installed in the bottom of the lower shear box (Figure 3-8) which is also used for piloting the temperature tests and a top Pt100 temperature sensor installed in the piston, used to measure the

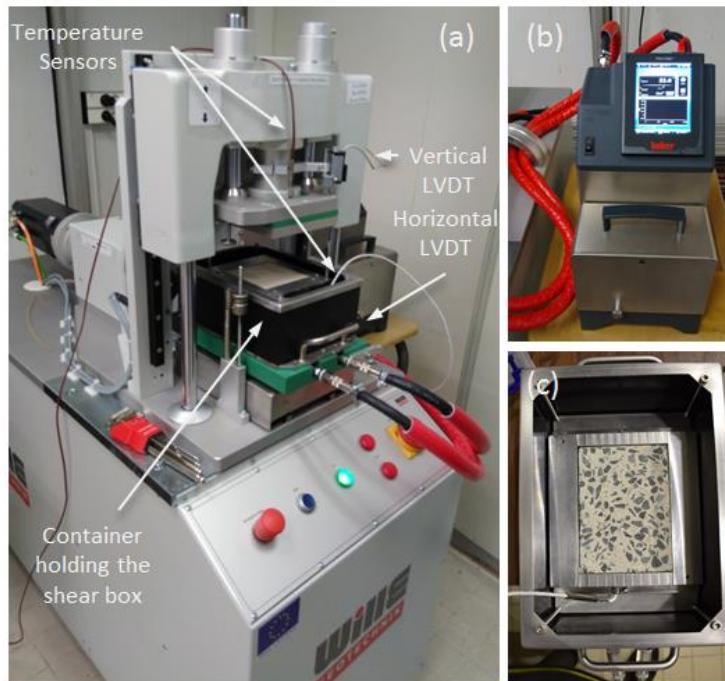temperature on the superior part of the sample. The allowable temperature range was set between $5 \; and \; 50°C$.

Tests can be performed in dry soil or submerged soil (e.g. the soil is plunged in water). For the interface test, a concrete plate is fixed in the lower part of the device and a soil sample in the upper part. During the shearing phase, the upper part of the device is fixed by the piston applying the vertical load and cannot move. The lower part moves horizontally, imposing a relative displacement with respect to the upper part that results in shearing the sample. The characteristics of the sensors are summarized in Table 3-7.

3.3.2 Sample preparation

3.3.2.1 Procedure

For all the sand concrete interface tests, the sample was installed by pouring layers of sand and then compacting them to a target density of 1.35g/cm^3 for the carbonate sand and of 1.60 g/cm^3 for the silica sand, by dry tamping (Figure 3-9).
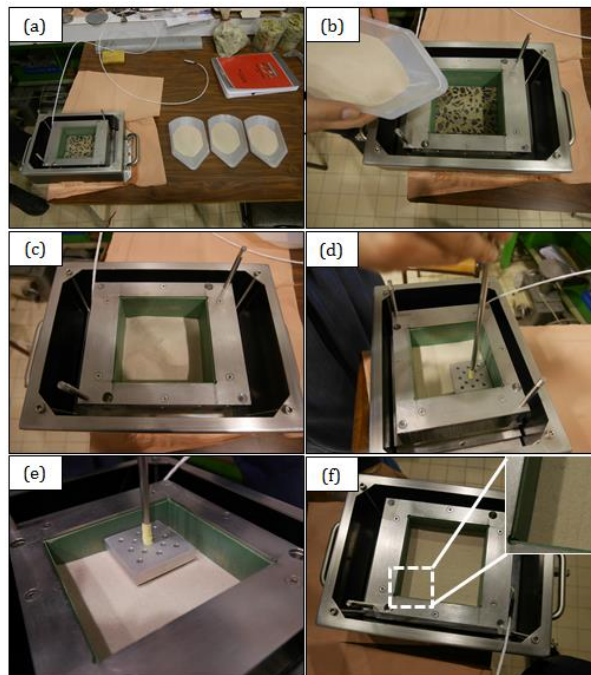
Figure 3-9 Steps of sample preparation: (a) shear box and containers of sand; (b) addition of the first layer of sand; (c) first layer completed; (d) sand packing in the shear box; (e) detail of (d); (f) flat top surface of sand after 3 layers.

The sample was then placed in the loading frame and a vertical load was applied and kept constant during the entire test (Constant Normal Load CNL test). Distilled water was added in the container in order to perform the test in (almost) saturated conditions. Temperature was then set to 13°C at the beginning of the tests.

3.3.2.2 Density measurement

After installing the three layers of sand into the shear box (Figure 3-9 (f)), the sample's density was determined by measuring the height of the sample on 12 different points (3 per side) with a high precision caliper. The weight of the sand placed into the box is known, so the initial density corresponds to the ratio of the mass of the sample divided by its volume into the box. After the application of the vertical stress and the thermal loading, the density was deduced from the vertical strain of the sample, assuming no lateral deformation.

3.3.3 Experimental program

The experimental program is divided in two separate parts: a validation campaign and a new experimental campaign to study the influence of temperature loading on the behavior at the interface between the soil and the concrete interface.

3.3.3.1 The validation campaign

3.3.3.1.1 Sensors validation

A series of 20 verification tests were performed on the two sensors: (a) the vertical displacement (internal sensor) and (b) the vertical extension (external LVDT) sensors, using Johansson gauge blocks. Gauge blocks of calibrated heights between 0,1 to 50 mm were used. An example for 5 blocks is shown in Table 3-8. Vertical and horizontal displacements were measured for increasing gauge heights. The piston was considered in contact with the gauge at a vertical stress of 5 to 15 kPa. The displacement measured between two gauges was compared to the known difference of calibrated heights, to calculate vertical displacement errors, in other words, the accuracy on vertical displacement values.

Gauge Block height	Stress	Vertical position	Imposed displacement	Measured displacement
mm	kPa	mm	mm	mm
10	5	142.16	-	-
20	5	132.169	10	9.991
30	5	122.172	20	19.988
40	5	112.163	30	29.997
50	5	102.153	40	40.007

Table 3-8: Correspondence between the displacement imposed and the displacement measured for the internal sensor.

3.3.3.1.2 Classical direct shear test

Dry soil-soil direct shear tests were performed using Fontainebleau sand employing a classical direct shear test device and the new interface direct shear test device, in order to compare the results and validate the machine.

The experimental program related to this first testing stage is provided in Table 3-9 (C=classical direct shear device, I= New Interface direct shear device).

N°	Test name	Normal effective stress $\sigma'_n [kPa]$	Density $\rho\ [kg/m^3]$
1	C_25kPa	25	1729
2	C_40kPa	40	1715
3	C_80kPa	80	1728
4	I_20kPa	20	1595
5	I_40kPa	40	1715
6	I_80kPa	80	1676

Table 3-9: Validation tests with the classical direct shear test in dry conditions.

It should be noted the classical direct shear test device employed is equipped with a smaller shear box ($60mm \times 60mm \times 24mm$) and possesses only one option for the horizontal loading speed, namely $1.27mm/min$. The vertical loading is performed by adding blocks of known weight on the loading frame and is considered instantaneous. Due to sand's high permeability, drained conditions are guaranteed regardless of the loading speed and saturation conditions. The Terzaghi assumption of effective stress ensures that the response of this material to direct shear testing in dry and fully saturated conditions is equivalent (Di Donna 2014).

According to conventional direct shear testing (NF P94-071-1, 1994), the material is firstly consolidated and then a displacement controlled shear test is performed at a constant speed of $1.27mm/min$. The test was repeated for three normal stress values: $20\ kPa,\ 40kPa,\ 80kPa$, corresponding to typical normal effective stress values acting on the pile soil interface at different depth for pile foundations. The same experimental procedure was used to perform another three sand-sand direct shear tests employing the newly acquired interface direct shear test device adapted for thermal loading. The sand is consolidated by applying a normal stress of $20\ kPa,\ 40kPa$ and $80kPa$ respectively and then a displacement controlled shear test is performed at a constant speed of $1.27mm/min$.

3.3.3.2 Experimental campaign to study the effect of temperature on the soil concrete interface

The second part of the experimental campaign includes soil – concrete interface direct shear tests performed to characterize the effect of temperature and temperature cycles at the soil-concrete interface. The main objectives of this campaign are the study of:

- The impact of temperature changes on the volumetric behaviour and on the shear strength mobilization at a soil-concrete interface
- The impact of temperature cycles on the volumetric behaviour and on the shear strength mobilization at a soil-concrete interface

A series of monotonic displacement-controlled direct shear tests were performed at 13°C, under constant normal stress equal to 50 kPa, 100kPa and 150kPa. The rate of applied horizontal displacement was 0.5mm/min. Tests at 13°C were used as references. A series of monotonic displacement controlled direct shear tests were also performed at 8°C and 18°C. In that case, the temperature was imposed equal to 13°C in a first step and then imposed equal to 8°C or 18°C in a second step. Then a monotonic displacement-controlled direct shear tests was performed for each case.

A series of displacement controlled direct shear tests after 10 thermal cycles were also performed for the three vertical stress values cited above (50kPa, 100kPa and 150kPa). In this case, after the application of the vertical load and setting the temperature of the sample equal to 13°C, the temperature varied between 8°C and 18°C ($\Delta T = 10°C$) for ten cycles. A monotonic displacement-controlled direct shear test was performed for each case.

3.3.3.2.1 Fontainebleau sand – concrete experimental campaign

A list describing the tests performed for this part of the experimental campaign is presented in Table 3-10. The monotonic tests were repeated between 2 and 5 times, and the cyclic tests were repeated 3 times each (FS= Fontainebleau Sand; C1, C2, C3 = Cyclic temperature test 1, 2 and 3; 13, 8, 18, 8-18 represent the temperature or temperature ranges; 50kPa, 100kPa, 150kPa represent the applied normal load).

3.3.3.2.2 Carbonate sand – concrete experimental campaign

A list describing the tests performed for this part of the experimental campaign is presented in Table 3-11. Due to the limited amount of available carbonate sand, test repeatability was not investigated (CS= Carbonate Sand; C1= Cyclic temperature test 1; 13, 8, 18, 8-18 represent the temperature or temperature ranges; 50kPa, 100kPa, 150kPa represent the applied normal load).

3.3.3.2.3 Green clay – concrete experimental campaign

Intact core samples were collected from Ecole des Ponts Paris Tech in order to perform soil – concrete interface direct shear tests. These tests were meant to complete the results obtained from the in-situ experimental campaign (chapter 2.3), thus providing insight in the effect of temperature cycles at the soil-pile interface. Unfortunately most of the material found in these core samples (cumulative length of all tubes of about 7m) was highly heterogeneous, making the preparation of the interface direct shear test sample quasi impossible (Figure 3-10). Preparation of disturbed samples by wet sieving and then consolidated in an oedometer cell was thus considered. Nonetheless, due to the unusual size of the shear cell (100mmx10mmx50mm) it was decided that this procedure cannot be fitted in the timeframe of this study. For these reasons, only two tests were performed on intact Green Clay soil.
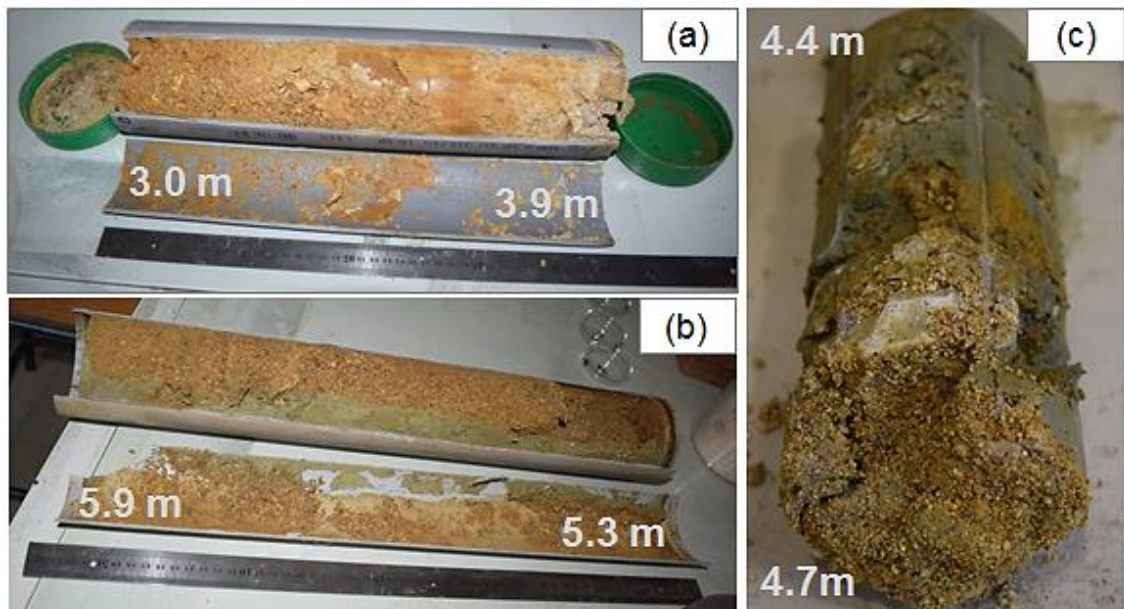

Figure 3-10: Green Clay borehole between (a) 3 to 3.9m deep, (b) 5.3 to 5.9m deep, (c) magnification view on the cores at a depth of 4.7m.

N°	Test name	Normal effective stress $\sigma'_n[kPa]$	Density ρ [kg/m³]	Temperature [°C]
1	FS_13_50kPa	50	1733	13
2	FS_13_100kPa	100	1735	13
3	FS_13_150kPa	150	1735	13
4	FS_8_50kPa	50	1739	8
5	FS_8_100kPa	100	1790	8
6	FS_8_150kPa	150	1789	8
7	FS_18_50kPa	50	1799	18
8	FS_18_100kPa	100	1698	18
9	FS_18_150kPa	150	1705	18
10	C1_FS_8-18_50kPa	50	1707	10 cycles 8-18
11	C1_FS_8-18_100kPa	100	1715	10 cycles 8-18
12	C1_FS_8-18_150kPa	150	1720	10 cycles 8-18
13	C2_FS_8-18_50kPa	50	1734	10 cycles 8-18
14	C2_FS_8-18_100kPa	100	1734	10 cycles 8-18
15	C2_FS_8-18_150kPa	150	1739	10 cycles 8-18
16	C3_FS_8-18_50kPa	50	1739	10 cycles 8-18
17	C3_FS_8-18_100kPa	100	1749	10 cycles 8-18
18	C3_FS_8-18_150kPa	150	1753	10 cycles 8-18

Table 3-10: Fontainebleau Sand Concrete interface tests.

N°	Test name	Normal effective stress $\sigma'_n[kPa]$	Density ρ [kg/m³]	Temperature [°C]
1	CS_13_50kPa	50	1325	13
2	CS _13_100kPa	100	1353	13
3	CS _13_150kPa	150	1333	13
4	CS _8_50kPa	50	1357	8
5	CS _8_100kPa	100	1331	8
6	CS _8_150kPa	150	1309	8
7	CS _18_50kPa	50	1337	18
8	CS _18_100kPa	100	1338	18
9	CS _18_150kPa	150	1317	18
10	C1_ CS _8-18_50kPa	50	1285	10 cycles 8-18
11	C1_ CS _8-18_100kPa	100	1302	10 cycles 8-18
12	C1_ CS _8-18_150kPa	150	1312	10 cycles 8-18

Table 3-11: Carbonate sand concrete interface test.

3.4 Results

3.4.1 Validation campaign

To validate the new device, a series of soil-soil direct shear test were performed, and compared to the results obtained using a classical direct shear test device. As it can be observed from Table 3-9 and Figure 3-11 the vertical load applied on the sample is slightly different between the tests performed using the classical device and those performed using the new device. This is due to the difficulties to control the vertical load on the classical direct shear device available in the laboratory. Nonetheless these small differences do not affect the calculation of the critical friction angle.
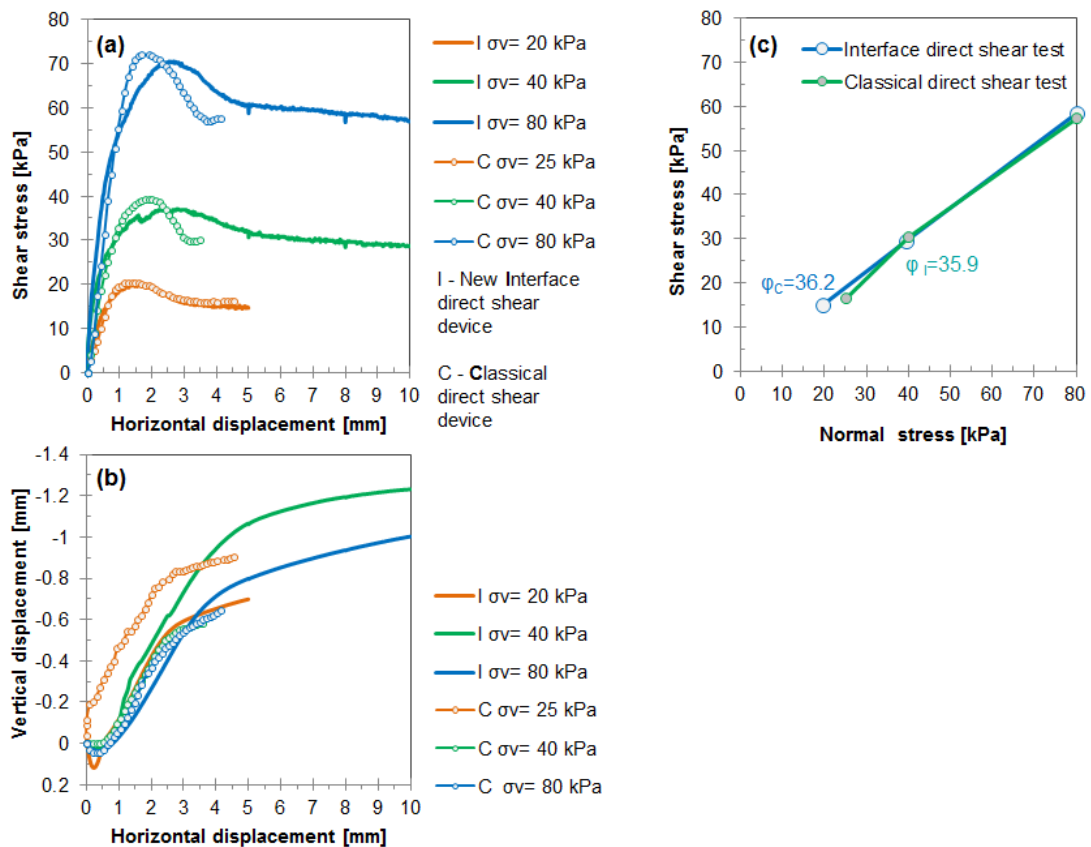
Figure 3-11: : Comparison between the direct shear test performed using the classical direct shear test device and the new interface direct shear test device (a) Shear strength, (b) Vertical displacement versus horizontal displacement (c) Critical internal friction angle.

Figure 3-11 (a) (a) presents the shear strength mobilization during the direct shear test for different vertical stress values for both devices. It can be noted that for the classical shear device the peak shear strength values are higher than those obtained for the same vertical stress using the new interface direct shear device. Moreover, the peak values are recorded for lower values of horizontal displacement. These observations can be however attributed to scale effects (the classical box is almost two times smaller than

the new interface direct shear box). Previous studies (Palmeira and Milligan 1989; Cerato and Lutenegger 2006) on the effect of the size of the shear box pointed out that the behaviour of the sample may be significantly affected by the scale of the test, due to the fact to a different mobilization of the dilatancy during shearing (less dilatancy in larger boxes). On the other hand, the post peak behaviour is similar for the two devices. The critical friction angle values (Figure 3-11 (c)) are also very close (a difference of only 0.3°). Since large displacements are often encountered along the shaft of a pile foundation, it is interesting to note that the two devices yield similar results at critical state, validating thus the use of the new interface direct shear device.

3.4.2 Thermo-mechanical behavior of Fontainebleau sand – concrete interface subjected to monotonic and cyclic thermal loading

3.4.2.1 Reference test at 13°C

The in-situ results presented in chapter 2 point out the fact the undisturbed soil temperature below 5 m with respect to the ground level is constant and on average equal to 13°C (Figure 2-15, Figure 2-43 (a)). Based on this observation, a series of interface direct shear tests were performed in the laboratory at 13 °C (to be used as reference) and the results are presented in Figure 3-12.

The evolution of the mobilized shear stress with the horizontal displacement (Figure 3-12 (a)) shows for the chosen imposed normal stress and sample density that the sample doesn't present a peak phase before reaching the critical state (constant volume conditions). These results are typical of larger size shear boxes (the shear box has a surface of 100mm x 100 mm). Although the sample densities before the shear test ($\rho_{50kPa} = 1800 \ kg/m^3$, $\rho_{100kPa} = 1820 \ kg/m^3$, $\rho_{150kPa} = 1840 \ kg/m^3$) are indicative of very dense sand, the results in terms of volumetric response, presented in Figure 3-12 (b) reveal sample compaction, common for loose sand (Figure 3-1). Only the tests performed under normal stress equal to 150kPa includes a dilative phase, typical for dense sand. It is worth noting though that the volumetric response is highly influenced by the specimen fabric and that it is extremely difficult to reproduce identical specimens especially in the case of sandy soils (Di Donna et al. 2016; Yavari et al. 2016a). The shear stress under constant volume conditions as a function of normal stress is presented in Figure 3-13. As expected in the case of sands the value of adhesion is almost null (cohesionless soil). In this study case the interface friction angle δ is equal to 26.8°, while the internal friction angle of the soil φ is equal to 36°. This result

confirms that shearing occurs at the interface rather than in the soil, which corresponds to a surface roughness lower than the critical one.
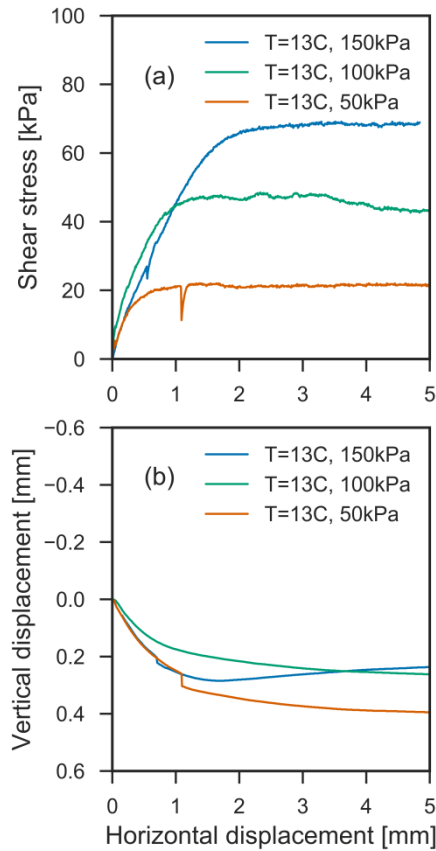
Figure 3-12 : a) Shear stress as a function of horizontal displacement during shearing phase; b) vertical displacement of the sample as a function of horizontal displacement during shearing phase.

Figure 3-13: Interface friction angle of Fontainebleau sand – concrete interface at 13°C.

3.4.2.2 Effect of monotonic thermal loading

In order to evaluate the effect of temperature on the response of silica sand-structure interface, a series of experiments were performed for different vertical stress values (50kPa, 100kPa, and 150kPa) representing the stress normal to the pile's surface at

different depths, and different temperature gradients (±5°C). The range of the chosen temperatures is representative for energy piles operation (Figure 2-39 (a)).
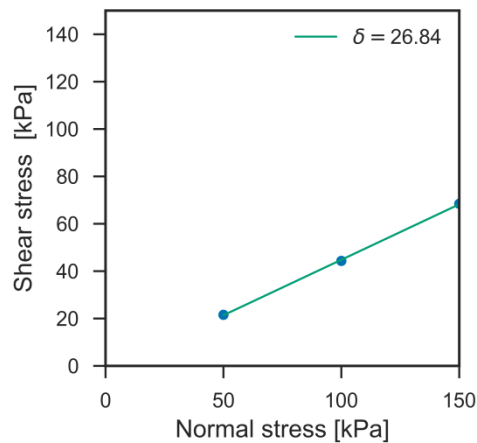
In a first phase, the effect of heating the soil was studied by increasing the samples' temperature from the reference temperature (i.e. $13°C$) to 18°C ($\Delta T = +5°C$). Then the effect of cooling was investigated by repeating the same procedure, but this time imposing a temperature gradient $\Delta T = -5°C$, thus resulting in cooling the samples from $13°C$ to $8°C$. Figure 3-14 presents the evolution of temperature and volumetric strain during heating, while Figure 3-15 presents the same results during cooling. The sand's temperature changed by $5°C$ in ~ 20 minutes (average rate of $0.2°C/min$). Once the temperature reached the imposed target value, it was held constant for 40 minutes to allow the possible dissipation of the pore water pressure induced by the temperature change. During heating all the tested specimens showed contractive volumetric strain ranging between ~ 0.1% and ~ 0.02%. Strains during cooling have opposite values: expansive volumetric strain ranging between ~ 0 and ~ 0.05%. Once the target temperature is reached and stays constant, all the heated specimens display expansive volumetric strain resulting, at the end of thermal loading, in strains ranging between ~ 0 and ~ 0.05%. The exact opposite happens during the cooling phase: once the temperature is constant the sample contracts resulting in total volumetric strains ranging between ~ 0 and ~ 0.1% ($0mm - 0.03mm$). Although small, these values are larger than the measurement accuracy (i.e. 0.01mm). A possible explanation for this phenomenon is provided by (Vargas and McCarthy 2007) who, using discrete element method simulations, found that under constant confining stress, the thermal expansion of sand particles may trigger particle rearrangements and introduce plastic volumetric contraction inside the specimen, which would stiffen the soil skeleton. (Sitharam 2003), points out that loose and medium dense sand has some unstable voids that can collapse due to heating induced particle rearrangements, resulting in contraction. This cannot however explain why expansive volumetric strain was observed during cooling. Qualitatively, the same behavior is observed for different normal stress values, confirming the repeatability of the results. The amplitude of the volumetric strain is nonetheless dependent on the applied vertical load: larger volumetric strains were observed when the sand is under lower stress, probably due to lower top restraint from the piston. The results of Ng et al. (2016) indicate that another possible explanation for the observed contractive/expansive behavior during heating/cooling may be due to the difference between the coefficient of thermal

expansion of the shear box and that of the tested sand. It is possible that, during heating the shear box expands more than the sand resulting in additional settlement of the specimen. To support this hypothesis, (Chen 2008) also found that the measured settlement of the specimen was larger when the thermal expansion coefficient of the container was larger. Once the target temperature is reached at the end of the heating phase though, the sand begins to expand. The same behavior is observed during the entire time the temperature remains constant (Figure 3-14 (a)).
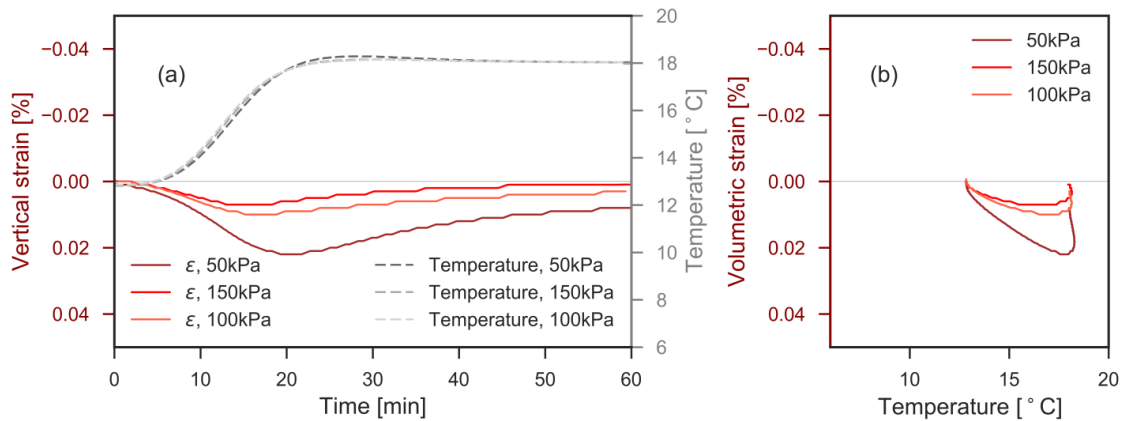

Figure 3-14: (a) Volumetric strain and temperature as a function of time during the heating phase 13 to 18°C of the sample at a vertical stress of 50, 100 and 150 kPa; b) volumetric strain as a function of temperature during the heating phase from 13 to 18 °C.
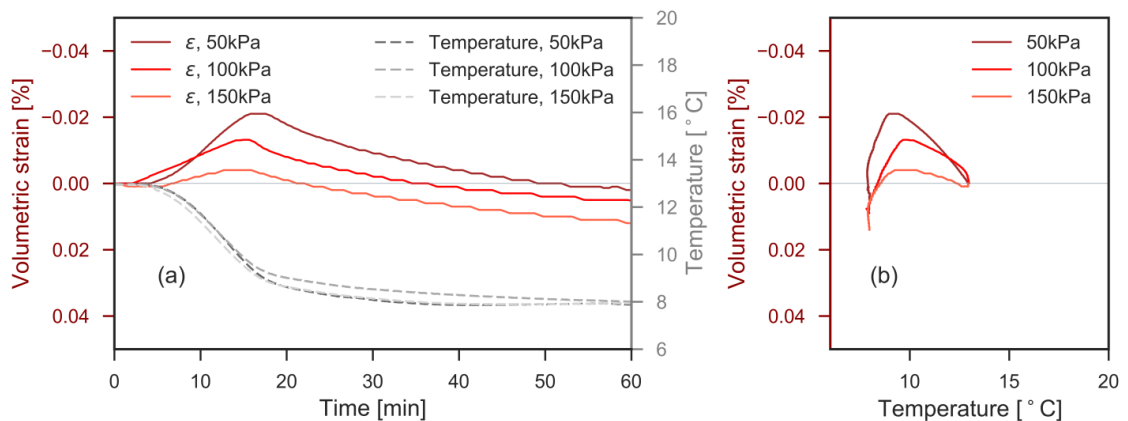
Figure 3-15: (a) Volumetric strain and temperature as a function of time during the cooling phase 13 to 8°C of the sample at a vertical stress of 50, 100 and 150 kPa; b) volumetric strain as a function of temperature during the cooling phase from 13 to 8 °C.

This may be due to the fact that a delay is to be expected in order for the entire soil mass to reach the constant target temperature. It should be also noted that this study was performed on submerged samples and the coefficient of thermal expansion of water varies with temperature variation and is much larger than that of the sand (water coefficient of thermal expansion at $8°C$ is $58.8 \times 10^{-6}/°C$, at $13°C$ it is $125.8 \times$

$10^{-6} / °C$ and at 18°C it is $184.6 \times 10^{-6} / °C$, while silica sand's coefficient of thermal expansion is equal to $12 \times 10^{-6} / °C$), which may explain the amplitude of the constant temperature deformation both during heating and cooling.

Following the heating or cooling of the sample, a displacement controlled interface direct shear test was performed to assess the impact of the temperature change on the interface friction angle. The evolution of the mobilized shear stress with horizontal displacement (Figure 3-16 (a), (b), (c)) shows that none of the sample undergoes a peak phase before reaching the constant volume conditions. These results are consistent with the conclusions of the reference test. Moreover, the critical state shear stress has similar values for each level of vertical stress applied regardless of the sample's temperature. The small differences in shear stress intensity were attributed to the variability in specimen density. These results confirm the fact that monotonic heating or cooling doesn't impact silica sand's behavior (Di Donna et al. 2016; Yavari et al. 2016a).
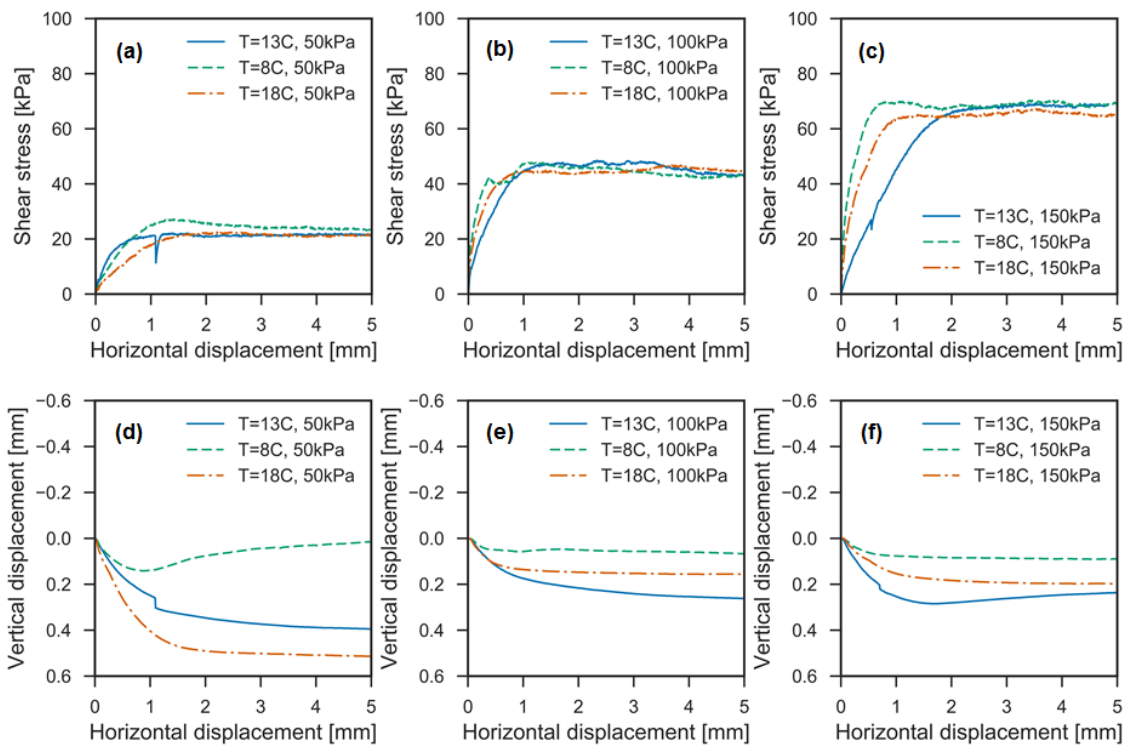
Figure 3-16 : Shear stress as a function of horizontal displacement at a) 50kPa, b) 100kPa, c) 150kPa; Vertical displacement as a function of horizontal displacement at a) 50kPa, b) 100kPa, c) 150kPa for monotonic thermal loadings at 8, 13 and 18°C.

Less consistent results are recorded for the volumetric behavior during shearing (Figure 3-16 (d), (e), (f)). The differences between the tests can be however correlated to slightly different initial density before the start of the shear test. Lower initial

densities allow the overall contraction of the samples. The volumetric behaviour is then consistent with the observed shear behaviour.

The resulting interface friction angle after each thermal loading test series (8°C, 18°C) was determined and compared to the value obtained for the reference case (13°C). The results, presented in Figure 3-17, show very similar results for 8°C,13°C and 18°C. The interface friction angle is 25°±0.7°, confirming once more that the temperature has no effect on the mobilization of shear strength at the interface concrete − silica sand.
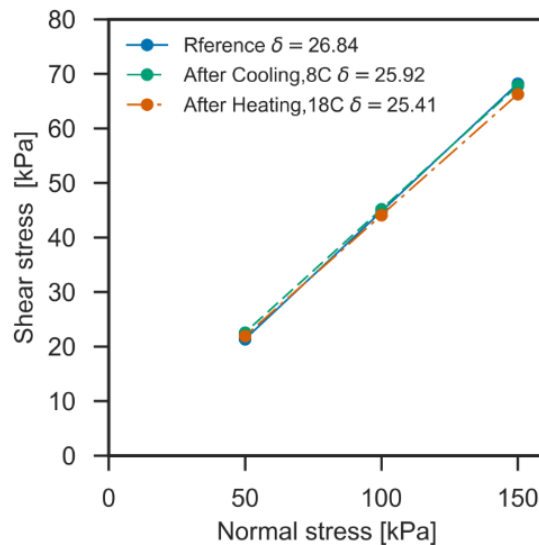

Figure 3-17: Interface friction angle of Fontainebleau sand – concrete for different monotonic thermal loadings.

3.4.2.3 Effect of cyclic thermal loading

A series of interface direct shear tests have been performed in order to account for the effect of cyclic thermal loading on the silica sand –concrete interface. The temperature and volumetric strain change during these tests are presented in Figure 3-18, Figure 3-19 and Figure 3-20 representing the results obtained during thermomechanical loading under normal stress values equal to 50kPa, 100kPa and 150kPa respectively.

The volumetric strain ε_v evolution reveals a cyclic behaviour consistent with the imposed temperature changes and maximum amplitude of ~0.2% (Figure 3-18 (a), Figure 3-19 (a), Figure 3-20 (a)). Along these thermal cycles, the sample describes an overall contractive behaviour resulting in average volumetric strain reduction of ~-0.1%. As it was observed during the monotonic heating and cooling test series, each heating phase is characterized by contractive behaviour followed by expansive behaviour while the temperature is kept constant (Figure 3-18 (b), Figure 3-19 (b), Figure 3-20 (b)).
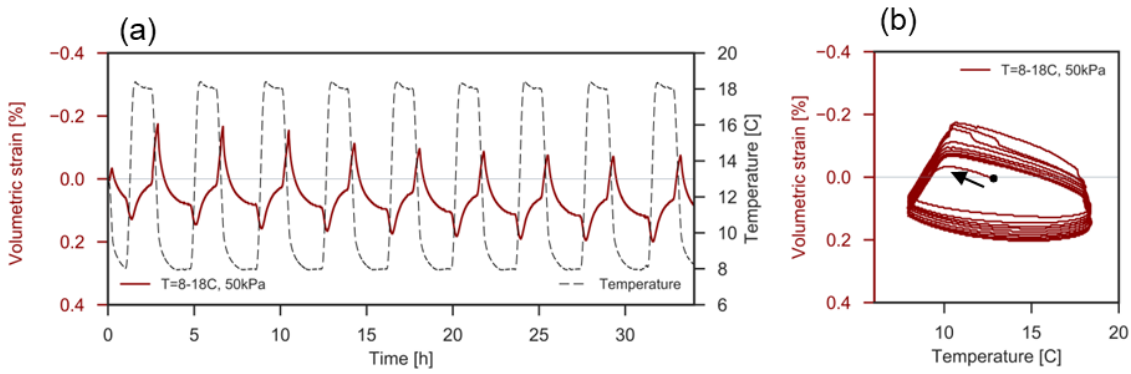
Figure 3-18: (a) Volumetric strain and temperature as a function of time for a vertical stress of 50 kPa; (b) volumetric strain as a function of temperature at 50 kPa during a thermal cycle between 8 and 18°C.
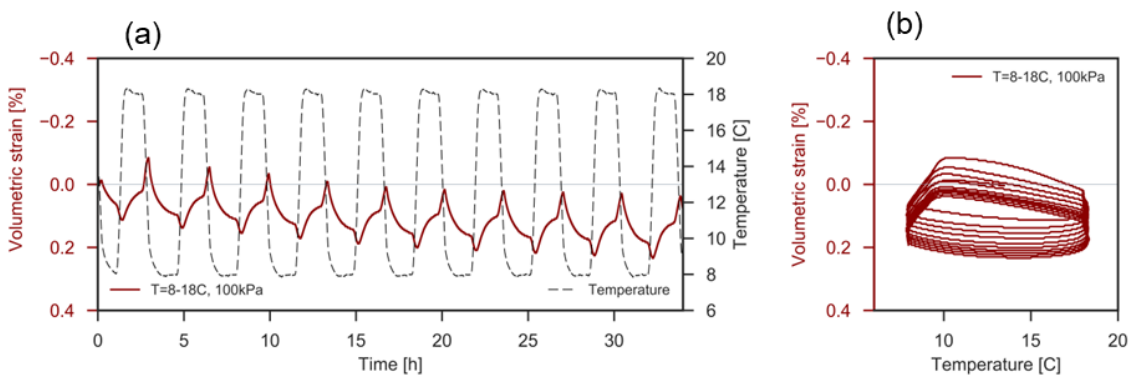
Figure 3-19: (a) Volumetric strain and temperature as a function of time for a vertical stress of 100 kPa; (b) volumetric strain as a function of temperature at 100 kPa during a thermal cycle between 8 and 18°C.
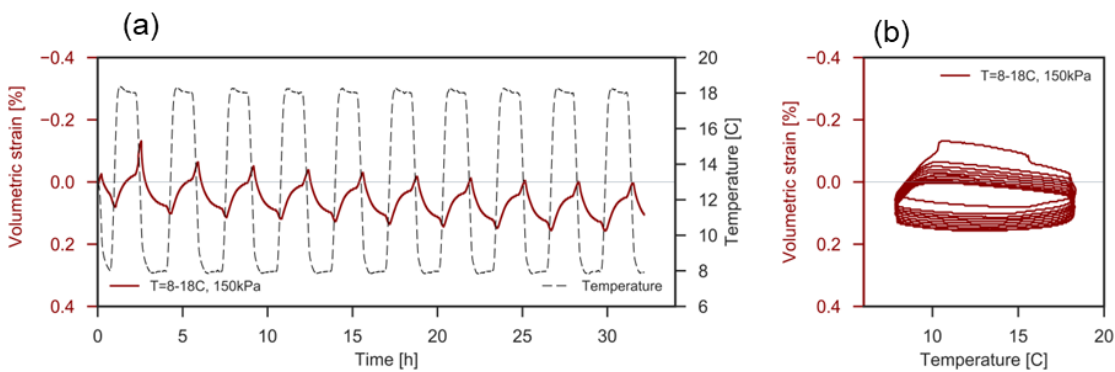
Figure 3-20: (a) Volumetric strain and temperature as a function of time for a vertical stress of 150 kPa; (b) volumetric strain as a function of temperature at 150 kPa during a thermal cycle between 8 and 18°C.

During each cooling phase, the response is reversed: while the temperature is decreasing, the sample is expanding and it starts contracting while the target temperature is reached and it is kept constant. It is not clear what prompts this behaviour. As mentioned previously, (Vargas and McCarthy 2007)attributed this behaviour to the fact that the thermal expansion of sand particles may trigger particle

rearrangements and introduce plastic volumetric contraction inside the specimen. This explanation cannot however account for the expansive behaviour observed during each cooling phase of every cycle. The results of Ng et al. (2016) indicate that another possible explanation for the observed contractive/expansive behavior during heating/cooling may be due to the difference between the coefficient of thermal expansion of the shear box and that of the tested sand, but both the sand and the box have coefficients of thermal expansion smaller then $20 \times 10^{-6} \, /°C$, which for the applied temperature gradient of 10°C would only account for a volumetric strain of 0.02%, while the recorded values during the test are 10 times higher.

The magnitude of the volumetric strain appears to be dependent on the applied vertical load and the sample's density: the higher the applied load, the lower the recorded volumetric strain, and the lower the density, the higher the volumetric strain is (the sample in Figure 3-18 has the density of 1.76 g/cm3, the one in Figure 3-19 has the density of 1.73 g/cm3 and the one in Figure 3-20 has the density of 1.79 g/cm3).
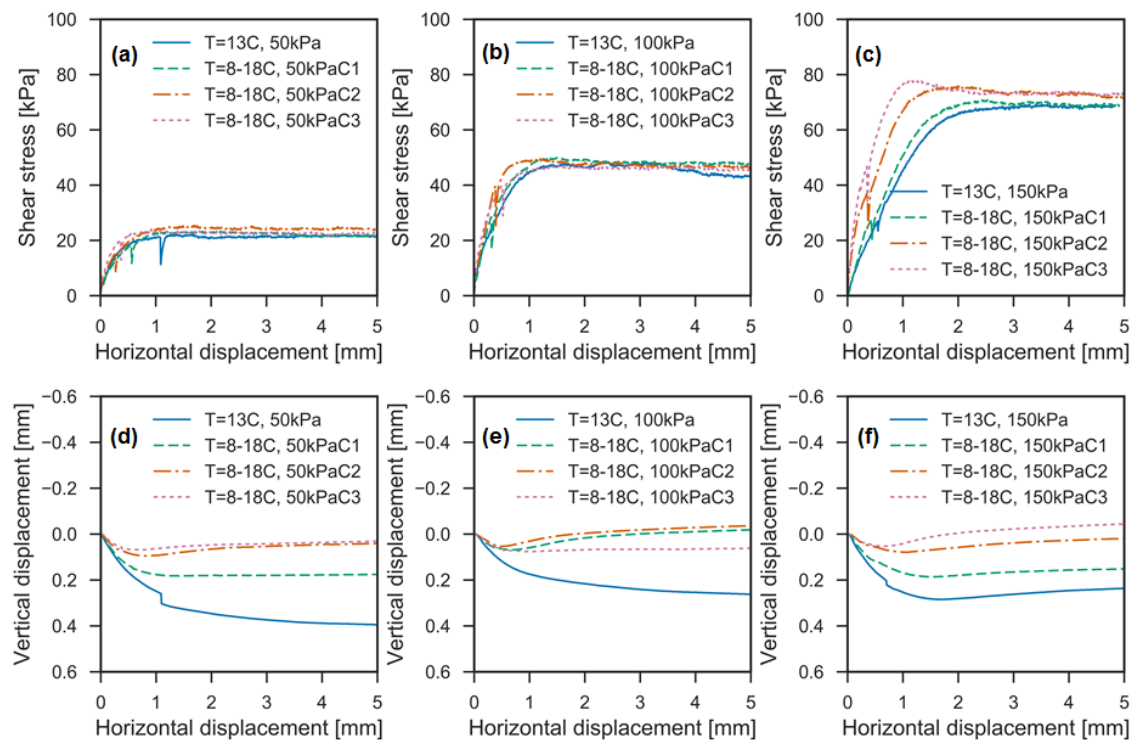

Figure 3-21: Shear stress as a function of horizontal displacement, at (a) 50 kPa, (b) 100 kPa and (c) 150 kPa; Vertical displacement as a function of horizontal displacement at a vertical stress of (d) 50 kPa, (e) 100 kPa and (f) 150 kPa for the reference temperature (13°C) and after each one of the cyclic thermal loading experimental campaign C1, C2 and C3.

The shear stress-horizontal displacement curves of the soil concrete interface after 10 heating-cooling cycles between 8°C and 18°C, under normal stresses of 50kPa, 100kPa, and 150kPa are presented in Figure 3-21 (a), (b) and (c) respectively. The cyclic temperature variation followed by interface direct shear tests, were repeated three times in order to check the repeatability of the results. The results obtained for samples subjected to 50 kPa and 100kPa normal stress are consistent for all repetitions and the average shear stress for constant volume conditions is almost equal to the value obtained in the reference case. The average critical state shear stress obtained under 50kPa vertical stress is equal to 22.5 kPa±1.2kPa, while the one obtained for 100kPa vertical stress is equal to 46.58kPa±1.1kPa. Figure 3-21 (c) suggests that in the case of vertical applied stress equal to 150kPa, the second and the third repetition of the cyclic thermomechanical test yields an increase of the shear stress mobilization, but it should be kept in mind that this difference is in fact very small. The average shear stress at the critical state is equal to 70.92kPa±2.49kPa and the difference between the highest shear stress value and the reference shear stress obtained at 13°C is of only 4.8kPa (7%), and can be attributed to small changes in the microstructure. The evolution of the volumetric response of these samples presented in Figure 3-21 (d), (e) and (f), suggests stiffer volumetric response after each cyclic thermomechanical test resulting in slightly denser samples, for which higher values of mobilized shear stress are obtained. The differences are however again very small.
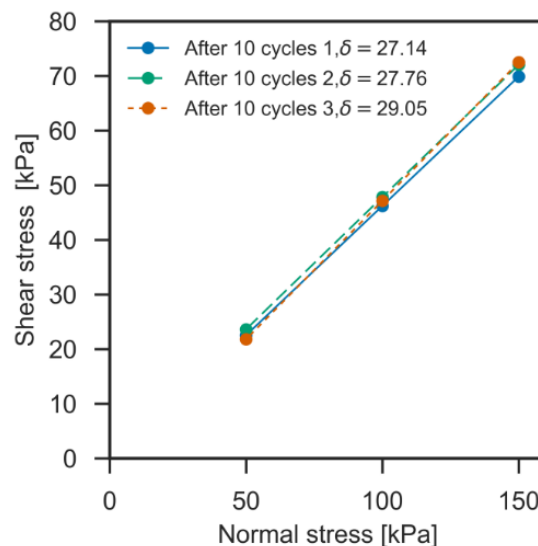

Figure 3-22: Shear envelope for the samples subjected to 10 thermal cycles.

The interface friction angle, calculated from the three displacement controlled interface direct shear tests (for a vertical load of 50 kPa, 100 kPa and 150 kPa respectively) was found equal to 26.8° for the tests performed on Fontainebleau sand at 13°C and 27.9°±0.9° for the three cyclic tests 8-18°C (Figure 3-22). These values are lower than the soil internal friction angle (36°) which confirms that the shearing occurs at the interface rather than in the soil. The maximum 2° difference between the interface friction angles identified for the two types of test suggests that the effect of temperature cycles on the sand-concrete interface remains very limited.

3.4.2.4 Conclusions

The shear behaviour and volumetric response of silica (Fontainebleau) sand-concrete interface at different temperatures (8°C, 13°C, and 18°C) and after 10 temperature cycles (8°C-18°C) was investigated through interface direct shear tests. The following conclusions can be drawn:

- The influence of monotonic thermal loading between 13°C and 8°C and between 13°C and 8°C on the volumetric response of Fontainebleau sand is very limited

- The cyclic thermal loading between between 8°C and 18°C results in overall slight contraction of the sample. The amplitude of the volumetric strain doesn't exceed 0.3% after 10 cycles

- During heating the sample contracts and starts expanding once the target temperature is reached and kept constant

- During cooling the sample expands and starts compacting once the temeprature target is reached and kept constant

- Monotonic heating/cooling of silica sand has no impact on the shear stress mobilization

- Ten heating-cooling cycles resulted in overall sand densification and a very slight increase of the interface friction angle under constant volume conditions

3.4.3 Thermo-mechanical behavior of the carbonate – concrete interface subjected to cyclic thermal loading

3.4.3.1 Reference at 13°C

As previously mentioned, the undisturbed soil temperature below 5m with respect to the ground level, measured in the in-situ tests, is equal to 13°C. Hence, similarly to the

Fontainebleau sand case study, a series of interface direct shear tests were performed at 13°C to be used as reference.
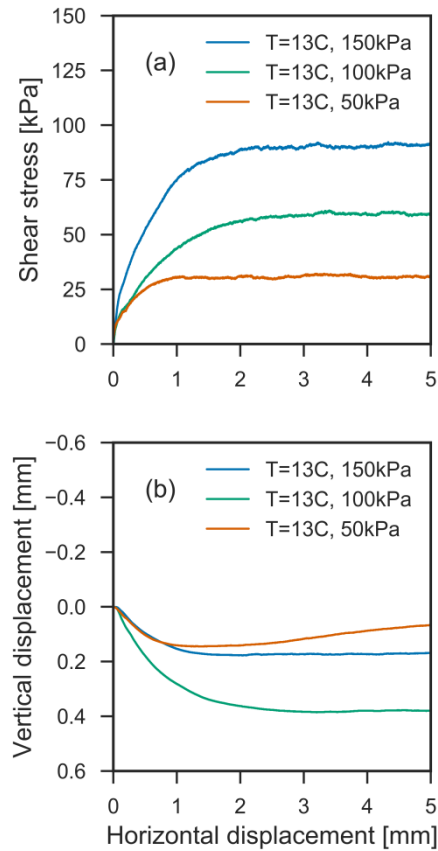
Figure 3-23: a) Shear stress as a function of horizontal displacement during shearing phase; b) vertical displacement of the sample as a function of horizontal displacement during shearing phase.

The evolution of the mobilized shear stress with the horizontal displacement (Figure 3-23 (a)) shows that for the chosen imposed normal stress the sample doesn't present a peak phase before reaching the critical state (constant volume conditions), which is typical of larger shear boxes. In terms of volumetric response, Figure 3-23 (b) indicates sample compaction for all tests. This is due to the low sample density and to grain crushing during shearing. The grain crushing can also explain why the test performed under a normal stress equal to 100kPa results in the sample contracting more than the test performed at 50kPa and 150kPa regardless of the sample's lower initial densities ($\rho_{50kPa} = 1379 \ kg/m^3$, $\rho_{100kPa} = 1490 \ kg/m^3$ and $\rho_{150kPa} = 1439 \ kg/m^3$ before the shear test).

Figure 3-24 shows that the cohesion is almost null for the carbonate sand – concrete plate interface. The interface friction angle is equal to 34.2° whereas the internal friction angle is 41° (Figure 3-24). As for Fontainebleau sand, this result confirms that shearing occurs at the interface rather than in the soil, regardless of the

fact that the normalized roughness of the concrete plate (R_n, Table 3-2) indicates a smooth surface. These results can be explained by the influence of the soil particle characteristics on the soil-structure interface response. Compared to silica sand, the carbonate sand has higher particle angularity and intraparticle porosity and lower grain hardness which results in high friction angle and compressibility (Safinus et al. 2013)
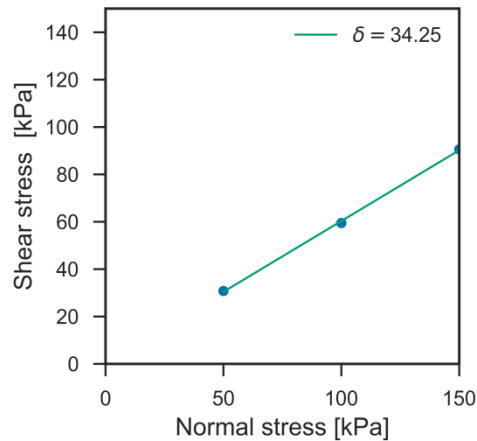
Figure 3-24: Carbonate sand-Concrete interface friction angle at 13°C.

3.4.3.2 Effect of monotonic thermal loading

In order to evaluate the effect of temperature on the response of silica sand-structure interface, a series of experiments were performed for different vertical stress values (50kPa, 100kPa, and 150kPa) representing the stress normal to the pile's surface at different depths and different temperature gradients (±5°C). The range of chosen temperatures is representative for energy piles operation (Figure 2-15, Figure 2-43 (a)).

The carbonate sand-concrete interface behavior at 18°C and 8°C (T = $\pm\mathbf{5°C}$ with respect to the reference temperature, i.e. 13°C) was studied. The evolution of the mobilized shear stress with respect to the horizontal displacement, presented in Figure 3-25, shows that none of the sample undergoes a peak phase before reaching the constant volume conditions. These results are consistent with the conclusions of the reference test. Moreover, the critical state shear stress has similar values for each level of vertical stress applied regardless of the sample's temperature. The small differences in shear stress intensity can be attributed to grain rearrangement and crushing. As in the case of silica sand, these results confirm the fact that monotonic heating or cooling doesn't impact the carbonate sand- concrete interface behavior.

Considering the volumetric behavior of the carbonate sand-concrete interface, very similar results were observed for the test performed under normal stress equal to

50kPa (Figure 3-25 (d)). Less consistent results are recorded for the volumetric behavior during shearing for normal stress (Figure 3-25 (e) (f)). Although the samples have similar densities before the interface shear test (100kPa test: $\rho_{100kPa,13°C} = 1490 \ kg/m^3$, $\rho_{100kPa,8°C} = 1460 \ kg/m^3$, $\rho_{100kPa,18°C} = 1429 \ kg/m^3$; 150kPa test: $\rho_{150kPa,13°C} = 1439 \ kg/m^3$, ,$\rho_{150kPa,8°C} = 1470 \ kg/m^3$, $\rho_{150kPa,18°C} = 1409 \ kg/m^3$) , indicative of loose sand, the response under an applied vertical load of 100kPa and 18°C displays some dilatancy. Moreover the sample compaction is higher for normal stress equal to 100kPa than for 50kPa and 150 kPa. These results were interpreted by grain crushing during the vertical loading and possibly during the shearing phase. However, due to time limitations, this interpretation was not verified.
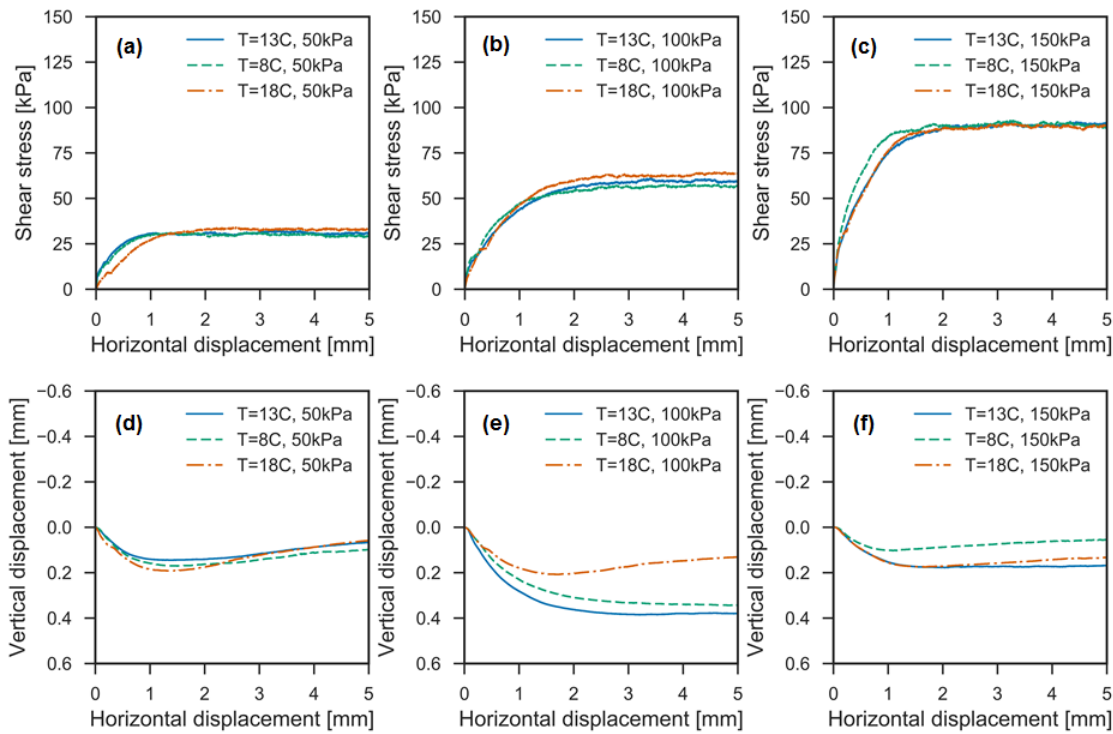
Figure 3-25: Shear stress vs horizontal displacement at (a)50 kPa, (b) 100 kPa (c) 150 kPa and vertical displacement vs horizontal displacement at (d)50 kPa, (e) 100 kPa (f) 150 kPa for interface direct shear tests performed at 13°C, 8°C and 18°C.

The resulting interface friction angle after each thermal loading test series (8°C, 18°C) was determined and compared to the value obtained for the reference case (13°C). The results, presented in Figure 3-26 are very similar for 8°C,13°C and 18°C. The interface friction angle was found equal to 34°±1.4° The small differences between the results obtained for each test series in this case can be rather attributed to modifications of the sample's fabric due to grain crushing rather than due to the effect

of temperature, confirming once more that a temperature change of $\pm 5°C$ doesn't impact the carbonate sand-concrete interface behavior.
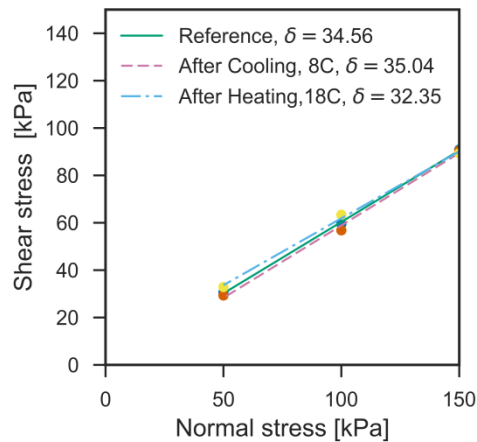
Figure 3-26: Carbonate sand-Concrete interface friction angle at 13°C, 8°C and 18°C.

3.4.3.3 Effect of cyclic thermal loading

A series of interface direct shear tests have been performed in order to account for the effect of cyclic thermal loading on the carbonate sand –concrete interface. The temperature and volumetric strain change during these tests are presented in Figure 3-27, Figure 3-28 and Figure 3-29, representing the results obtained during thermomechanical loading under normal stress values equal to 50kPa, 100kPa and 150kPa respectively.

The same offset between the sample response and the type of loading (heating/cooling), as in the case of Fontainebleau sand can be observed for carbonate sand: the sample starts dilating only after the target temperature was reached, for heating. At the end, the carbonate sand cyclic temperature tests show similar results to those obtained for Fontainebleau sand: a dilating phase during heating is followed by a contracting phase during cooling for each cycle leading to an overall contraction of the sample (Figure 3-27, Figure 3-28 and Figure 3-29). The recorded volumetric strains are small but not negligible and fit in the range between +0.35% and -0.2% (Figure 3-27 , Figure 3-28 and Figure 3-29).

Shear stress and vertical displacements vs horizontal displacement during shearing after thermal cycles are presented in Figure 3-30. The shear stress curves do not show any difference after cyclic and monotonic thermal loadings. However, the vertical displacement is lower than for the monotonic thermal loading case.
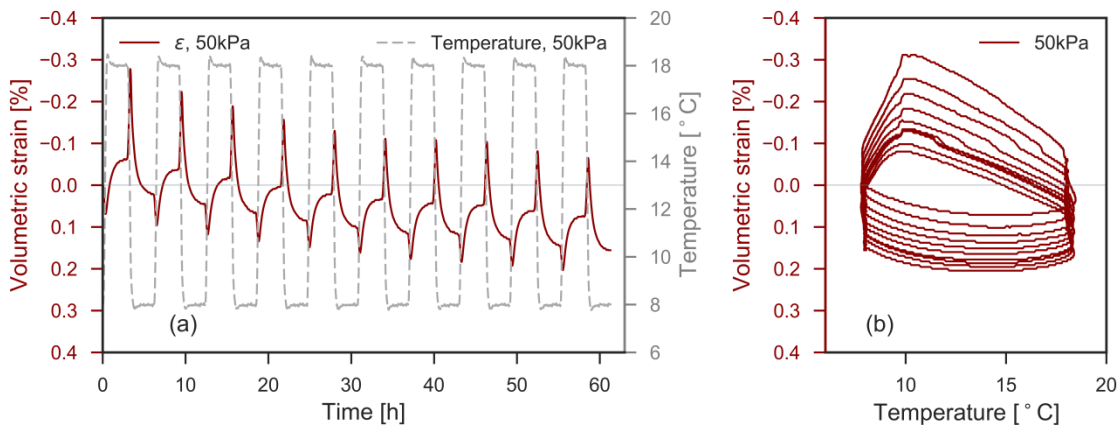
Figure 3-27 : (a) Volumetric strain and temperature vs time, (b) volumetric strain vs temperature at σv=50 kPa.
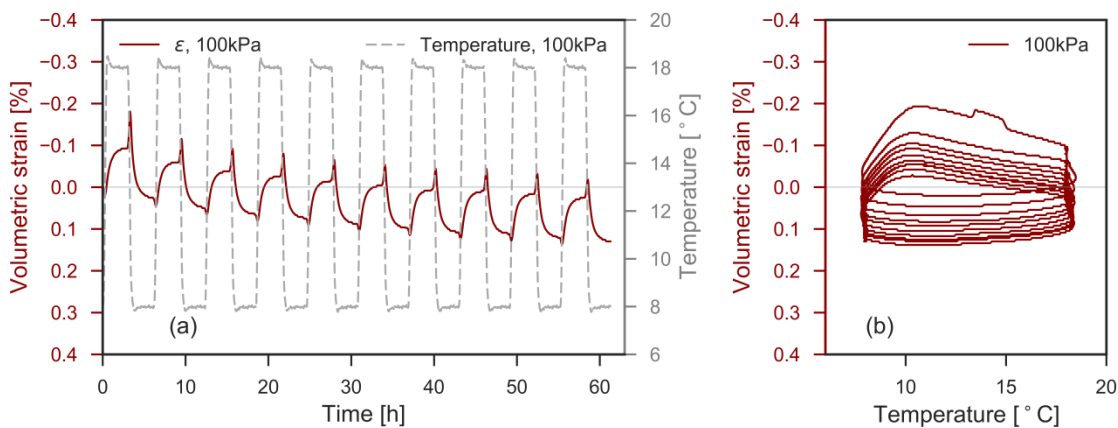
Figure 3-28 : (a) Volumetric strain and temperature vs time, (b) volumetric strain vs temperature at σ$_v$=100kPa.
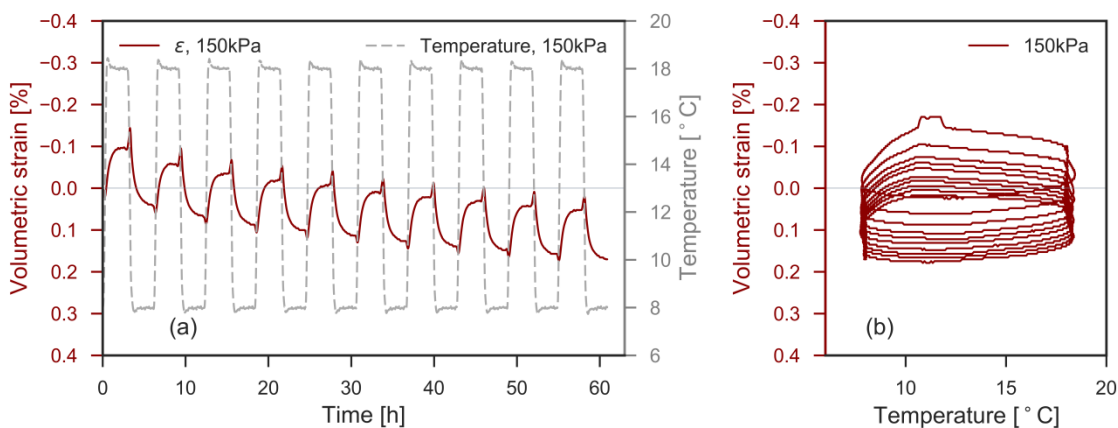
Figure 3-29 : (a) Volumetric strain and temperature vs time, (b) volumetric strain vs temperature at σ$_v$=150 kPa

The interface friction angles, obtained from the displacement-controlled interface direct shear test at 13°C and for the cyclic tests 8-18°C are 34.5° and 34.8° respectively (Figure 3-31). These values are lower than the soil internal friction angle (41°) which confirms that for the carbonate sand-concrete tests the shearing occurs at the interface

rather than in the soil. The small differences between the interface friction angles identified for the two types of test (at constant temperature and after 10 temperature cycles) implies that there is no influence of temperature cycles on the shear strength mobilization for the sand concrete interface.
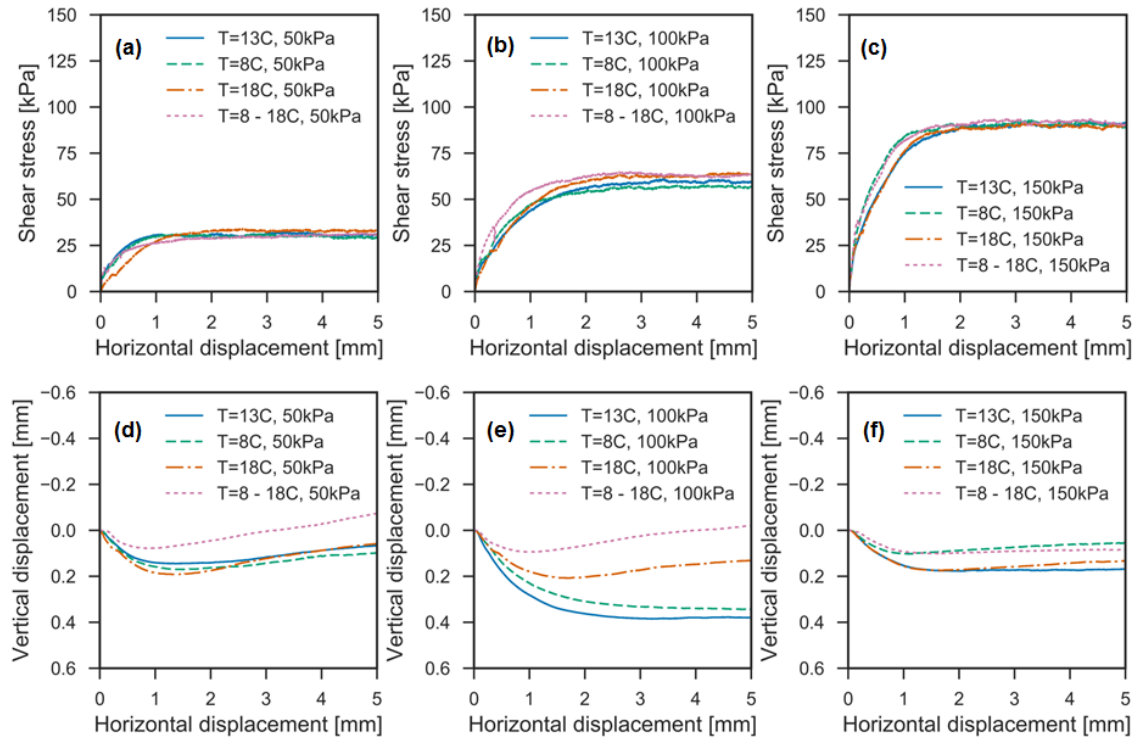
Figure 3-30: Shear stress vs horizontal displacement at (a)50 kPa, (b) 100 kPa (c) 150 kPa and vertical displacement vs horizontal displacement at (d)50 kPa, (e) 100 kPa (f) 150 kPa for interface direct shear tests performed at 13°C, 8°C and 18°C and after 10 (8°C-18°C) temperature cycles.
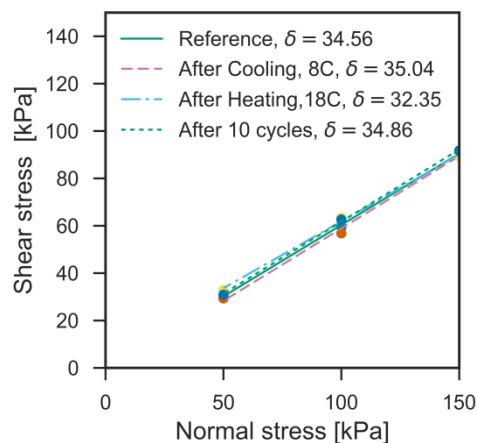
Figure 3-31: Carbonate sand-Concrete interface friction angle at 13°C, 8°C and 18°C and after 10 (8°C-18°C) temperature cycles.

3.4.3.4 Conclusion

The shear behaviour and volumetric response of carbonate sand-concrete interface at different temperatures (8°C, 13°C, and 18°C) and after 10 temperature cycles (8°C-18°C) was investigated through interface direct shear tests. The following conclusions can be drawn:

- The cyclic thermal loading between 8°C and 18°C results in overall slight contraction of the sample. The volumetric strain values are in the range of +0.35 to -0.2%. These values are higher than those obtained for Fontainebleau sand, probably due to a higher thermal dilation coefficient or crushing.

- During heating the sample contracts and starts expanding once the target temperature is reached and kept constant.

- During cooling the sample expands and starts compacting once the temeprature target is reached and kept constant.

- Monotonic heating/cooling of silica sand has no impact on the shear stress mobilization.

- Ten heating-cooling cycles resulted in overall sand densification. Contrary to Fontainebleau sand, there is not any clear trend which describes an increasing of dilatancy with both cyclic thermal loadings and vertical stress. To understand the results, more tests are necessary and grain size distribution should be measured after the tests.

- Grain crushing and grain size distribution changes are expected and may explain the absence of any dense sand behaviour at 150 kPa after thermal cycles. Also, the heterogeneous grain shape could be also involved in the response of this sand during the tests performed.

- The small variation of the value of the interface friction angle are associated to modifications of the sample's fabric due to grain crushing rather than due to the effect of temperature.

- Despite of a lack of repeats on the carbonate sand, the results show a negligible influence of temperature on the value of interface friction angle.

3.5 General discussion and conclusions

The effect of cyclic temperature changes on quartz sand-concrete and carbonate sand-concrete interfaces was studied in the laboratory using an interface direct shear device adapted for thermo-mechanical loading. It was found that the effect of 10

temperature cycles with a gradient $\Delta T=10°C$ on the mobilization of the shear strength at the soil-concrete interface is negligible. Nevertheless, these temperature cycles lead to a slight sample densification for both types of sand.

The mean interface friction angle value, determined at the laboratory scale, completes the work performed at the real scale (see chapter 2). Regarding the geothermal activation performed at the real scale, the laboratory scale results allow demonstrating that the influence of temperature (between 8 and 18°C) is negligible on the constant volume friction angle of sandy soils (silica and carbonate sands) at the interface with a rough concrete pile. Further investigations have to be performed on Green Clay.

For Fontainebleau sand, the volumetric strain shows variation with maximum amplitude of 0.25% during temperature cycles. An accumulation of positive strains is recorded (compaction). These results may be explained by small grain rearrangement and gradual volume reduction. Except for the picks in the strain values recorded in the beginning of each heating and cooling cycle, that need more investigation, a dilating phase during heating is followed by a contracting phase during cooling for each cycle, leading to an overall contraction of the sample. This results also suggest that the magnitude of the volumetric strain is dependent on the applied normal load and the sample's density: the higher the applied load, the lower the recorded volumetric strain; the lower the density, the higher the volumetric (Figure 3-18 has a density of 1.76 g/cm3, the one in Figure 3-19 has a density of 1.73 g/cm3 and the one in Figure 3-20 has a density of 1.79 g/cm3).

The carbonate sand cyclic temperature tests show similar results to those obtained for Fontainebleau sand: except for the picks in the strain values recorded in the beginning of each heating and cooling cycle, , that need more investigation, a dilating phase during heating is followed by a contracting phase during cooling for each cycle, leading to an overall contraction of the sample (Figure 3-27 , Figure 3-28 and Figure 3-29). In the case of carbonate sand though, the sample expansion is more pronounced. The maximum volumetric strain is also more important (0.35% during the first thermal cycle. The carbonate sand test results display more pronounced volumetric strain values for lower load levels and for lower densities.

These results provide also quantitative information concerning the amplitude of the volumetric strain of sandy materials subjected to temperature cycles, useful for the development of numerical models that simulate accurately the effect of temperature at the pile-soil interface. The in situ and laboratory results both demonstrate the limited

impact of temperature changes and temperature cycles in the range of ±10°C on soil and soil-concrete interface. These results support the sustainability of geothermal activation of foundations.

The experimental study in the laboratory, presented in this manuscript, presents however some shortcomings. Only one type of concrete surface was tested ($R_{max} \sim 90 \mu m$) and the roughness of the concrete plate was considered constant during the experiments. Different roughness values should be tested to improve the strength of the conclusions. It is however difficult to assess the in-situ roughness. The temperature range tested is low but adapted for low depth geothermal energy. Higher temperatures should be considered, as well as higher vertical loads in order to consider the behavior of larger piles. The shear box is placed into an open water container, so the water evaporation was not controlled in this study. To insure the same level of water, water was regularly added in the box; it could be an aspect to improve.

The results of the shearing tests on silica and carbonates sands revealed that the influence of temperature loading (monotonic and cyclic) is low and negligible on the interface properties, even though an increasing of soil's density is recorded on silica sand after cyclic thermal loading. More cycles (Figure 3-32) should be applied to confirm the results, and more soils should be tested, especially clayey soils to cover the range of typical soils met in geotechnics.
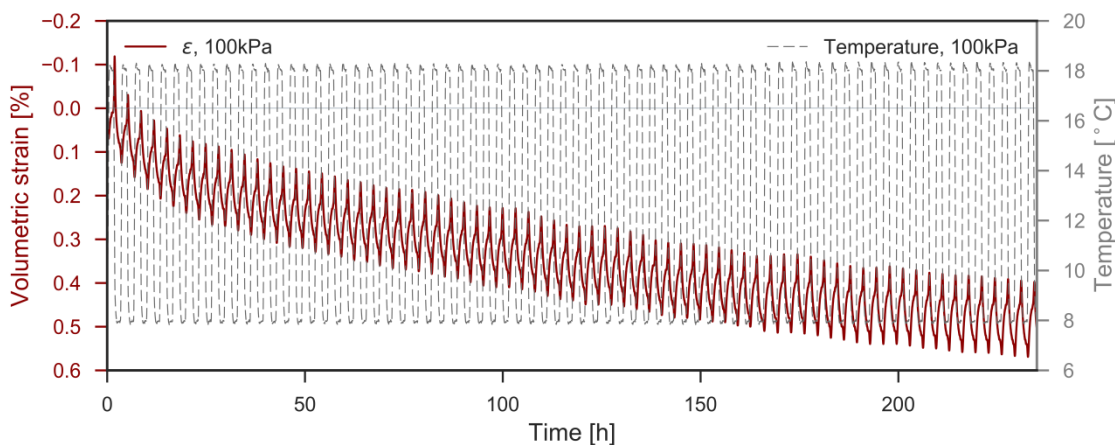
Figure 3-32 Volumetric strain and temperature vs time after 75 temperature cycles at σ$_v$=100 kPa.

4.NUMERICAL MODELLING OF ENERGY PILES

4.1 Introduction

Due to time and material constraints (experimentation costs, availability of appropriate instrumentation etc.), only a limited number of parameters can be evaluated in laboratory and in situ experimental campaigns (see previous chapters). Numerical simulations are therefore needed as prediction tools or in order to further investigate different loading scenarios.

This chapter focuses on the impact of different combinations of thermal and mechanical loads on the thermo-mechanical response of energy piles. A series of numerical simulations are compared to experimental results. Since in-situ experimental conditions are difficult to control (soil variability, temperature variation with depth etc.), a physical model for which both the soil properties and the loading conditions are controlled is first chosen to validate the approach. Then, preliminary results of the simulation of the Sept-Sorts case study are presented.

4.2 Mathematical formulation

A fully thermo-hydro-mechanical formulation is employed in the numerical simulations done with the finite element code Lagamine (University of Liège, Belgium). The equilibrium and balance equations as well as the water and heat diffusion laws are expressed in the moving current configuration through a Lagrangian updated formulation.

The equilibrium equation is (Eq. 4-1):

$$div(\sigma_{ij}) + \rho g_i = 0 \qquad \text{Eq. 4-1}$$

where div denotes the divergence operator, σ_{ij} the total stress tensor, g_i the gravity vector and ρ the bulk density of the material.

The total stress is defined as ((Terzaghi 1943), Eq. 4-2):

$$\sigma_{ij} = \sigma'_{ij} + p_w \delta_{ij} \qquad \text{Eq. 4-2}$$

where σ'_{ij} is the effective stress, p_w is the pore water pressure and δ_{ij} is Kronecker's delta.

The bulk density is defined as (Eq. 4-3):

$$\rho = n\rho_w + (1 - n)\rho_s \qquad\qquad \text{Eq. 4-3}$$

where n is the porosity, ρ_w is the water density and ρ_s is the density of the solid particles.

Introducing equations Eq. 4-2 and Eq. 4-3 in equation Eq. 4-1 results in Eq. 4-4:

$$div(\sigma'_{ij}) + \nabla p_w + [n\rho_w + (1 - n)\rho_s]g_i = 0 \qquad\qquad \text{Eq. 4-4}$$

where ∇ represents the gradient. The effective stress tensor σ'_{ij} is experessed as usual in an incremental form via a constitutive law.

The mass conservation equation is defined as (Eq. 4-5):

$$\frac{\partial p_w}{\partial t}\left[n\frac{1}{K_w} + (1 - n)\frac{1}{K_s}\right] + \frac{\partial T}{\partial t}[n\beta'_w + (1 - n)\beta'_s] + div(v_{rw,i}) = 0 \qquad\qquad \text{Eq. 4-5}$$

where t represents the time, $\frac{1}{K_w}$ and $\frac{1}{K_s}$ the water and the solid skeleton compressibility respectively, T the temperature, β'_w and β'_s the volumetric thermal expansions of water and solid skeleton respectively and $v_{rw,i}$ the relative velocity of water with respect to the solid skeleton. The first two terms of the equation represent the internal mass variation of the water and of the solid induced by the changes in the pore water pressure and temperature respectively. The third term represents the exchange of water between the reference volume and the outside. In the Lagrangian-updated formulation implemented in the finite element code, the mass conservation equation is checked at each step in the deformation configuration so that the solid mass exchange is null.

The relative velocity of the water with respect to the solid can be expressed by the Darcy law (Eq. 4-6):

$$v_{rw,i} = -\frac{k}{\rho_w g}\nabla(p_w + \rho_w gz) \qquad\qquad \text{Eq. 4-6}$$

where k is the hydraulic conductivity and z is the vertical coordinate.

The hydraulic conductivity k, is expressed in terms in of the intrinsic permeability k^{int} as (Eq. 4-7):

$$k = -\frac{k^{int}\rho_w g}{\mu_w} \qquad\qquad \text{Eq. 4-7}$$

where μ_w is the water dynamic viscosity.

The hydraulic conductivity's thermal dependence (thermo-hydraulic coupling) is represented by μ_w (Eq. 4-8) and ρ_w (Eq. 4-9) dependence on temperature (Thomas and King 1994):

$$\mu_w = 0.6612(T - 229)^{-1.562} \qquad \text{Eq. 4-8}$$

$$\rho_w = \rho_{w0}\left(1 + \frac{\partial p_w}{\partial t}\frac{1}{K_w} - \frac{\partial T}{\partial t}\beta'_w\right) \qquad \text{Eq. 4-9}$$

where ρ_{w0} is the water density at the reference temperature and density.

The energy conservation equation is (Eq. 4-10):

$$\rho c_p \frac{\partial T}{\partial t} - div(\lambda \nabla T) + \rho_w c_{p,w} v_{rw,i} \nabla T = 0 \qquad \text{Eq. 4-10}$$

where c_p is the soil specific heat and λ is the soil thermal conductivity.

In this equation, the first term corresponds to the heat stored in the medium, the second the heat transfer by conduction, according to Fourier's law and the third one, the heat transferred by convection (thermo-hydraulic coupling).

$$\rho c_p = n\rho_w c_{p,w} + (1 - n)\rho_s c_{p,s} \qquad \text{Eq. 4-11}$$

where $c_{p,w}$ is the water specific heat and $c_{p,s}$ is the solid particles specific heat.

$$\lambda = n\lambda_w + (1 - n)\lambda_s \qquad \text{Eq. 4-12}$$

where λ_w is the water thermal conductivity and λ_s is the solid particles thermal conductivity.

4.3 Constitutive model

In the following numerical analysis the pile behaviour is assumed thermo-elastic. The soil and the soil-pile interface are assigned a thermo-elasto-plastic constitutive model that is based on the Mohr-Coulomb constitutive law. The increment of total deformation, $d\varepsilon_{ij}$, (Eq. 4-13) includes an elastic component, $d\varepsilon_{ij}^e$, and a plastic component, $d\varepsilon_{ij}^p$:

$$d\varepsilon_{ij} = d\varepsilon_{ij}^e + d\varepsilon_{ij}^p \qquad \text{Eq. 4-13}$$

The response inside the elastic domain is thermo-elastic and the increment of effective stress, $d\sigma'_{ij}$ (Eq. 4-14), is defined as follows:

$$d\sigma'_{ij} = C_{ijkl}(d\varepsilon_{kl} + \beta'I_{kl}dT) \qquad \text{Eq. 4-14}$$

where C_{ijkl} is the stiffness tensor that contains the material properties, β' is the vector containing the linear thermal expansion coefficient of the material, I_{kl} is the identity matrix and dT is the temperature increment.

The limit between the elastic domain and the elasto-plastic domain in the stress space is expressed by the yield surface, f (Eq. 4-15). For the Mohr-Coulomb criterion the yield surface is defined as follows:

$$f = \sqrt{J_2} - \frac{m \sin\varphi'}{3}I_1 - mc'\cos\varphi' = 0 \qquad \text{Eq. 4-15}$$

where J_1 and J_2 are the first invariant of the stress tensor and the second invariant of the deviatoric stress tensor respectively , φ' is the soil angle of shear strength, c' is the soil cohesion and m (Eq. 4-16) is defined as follows:

$$m = \frac{\sqrt{3}}{\sqrt{3}\cos\theta_l + \sin\theta_l\sin\varphi'} \qquad \text{Eq. 4-16}$$

where θ_l is the Lode angle.

When the yield locus is attained, the increment of effective stress is (**Eq. 4-17**):

$$d\sigma'_{ij} = C_{ijkl}(d\varepsilon_{kl} - d\varepsilon^p_{kl} + \beta'I_{kl}dT) \qquad \text{Eq. 4-17}$$

The increment of plastic deformation is described by the following flow rule (Eq. 4-18):

$$d\varepsilon^p_{ij} = \lambda_p \frac{\partial g}{\partial \sigma'_{ij}} \qquad \text{Eq. 4-18}$$

where λ_p is the plastic multiplier and g is the plastic potential.

This model assumes that the plastic potential has the same form as the yield function but the friction angle at shear strength is replaced by the dilatancy angle ψ' (non-associated flow rule). Integration of the constitutive law is performed using an implicit backward Euler scheme with a return mapping normal to the flow surface.

4.4 Numerical model for energy piles in saturated sand - centrifuge tests

The centrifuge model tests used as reference for the numerical simulations presented hereafter were carried out at the Geotechnical Centrifuge Facility of the Hong Kong University of Science and Technology and are presented in detail by Ng et al. (2014b). These tests were chosen to validate the adopted numerical approach due to controlled material and loading conditions.

4.4.1 Centrifuge modelling of energy foundations

Physical modelling has been widely used to investigate pile's behaviour in different soils (Georgiadis et al. 1992; Horikoshi and Randolph 1996; McVay et al. 1998; Hölscher et al. 2012). Geometric similitude is employed to extrapolate the load-settlement behaviour of model-scale energy foundations to the full-scale prototype.

Parameter	Scale	Parameter	Scale
Acceleration	N	Force	$1/N^2$
Length	$1/N$	Stress-strain	1
Area	$1/N^2$	Time(dynamic)	$1/N$
Volume	$1/N^3$	Time(consolidation/diffusion)	$1/N^2$
Mass	$1/N^3$	Time(creep)	1
Density	1	Pore fluid velocity	N
Unit Weight	N	Thermal flow	$1/N^2$

Table 4.1 Scaling factor for centrifuge tests Schofield (1980) and Taylor (1995).

In the case of energy piles, the effect of temperature must be considered. Spatial measurements of temperature in dry quartz sand surrounding a cylindrical heat source during centrifugation at different g-levels by Krishnaiah and Singh (2004) showed that centrifugation does not lead to change in the heat-flow process and that the time required for heat flow by conduction is N^2 times faster in the centrifuge model. Savvidou (1988) derived the same scaling factor for the time required for heat flow for the case of one-dimensional heat conduction in Cartesian coordinates using the diffusion equation. This translates into a greater volume of soil surrounding the model pile being affected by heating. According to Stewart and McCartney (2013) one solution to address the scaling conflict is to calibrate numerical finite element simulations of the tests using the model-scale measurements (Rotta Loria et al. 2015). A

list of relevant scaling factors proposed by Schofield (1980) and Taylor (1995) are presented in Table 2.3.

4.4.2 Centrifuge model

The tests were performed in a container with internal dimensions of $1245mm \, x \, 350mm \, x \, 850mm$ (Figure 2-26), (Ng et al. 2014b). The internal container walls were insulated by an 18 mm thick wooden layer coated with plastic membranes to prevent water flow. Three model piles were installed in Toyoura sand: one reference pile, labelled RP and two energy piles, labelled EP1 and EP2 respectively. The spacing between each pile and the borders of the centrifuge was larger than 10 times the pile diameter thus ensuring sufficient space to prevent boundary effects or interactions between the piles (Bolton 1998).

The model piles were made of aluminium alloy pipes with an inner diameter of 19mm, an outer diameter of 13mm and a total length of 600 mm (out of which only 490 mm were embedded in sand). Ten levels of strain gauges were installed at 60 mm intervals, beginning at 40 mm from the pile cap (Figure 2-26 a, b). The energy piles were also equipped with thermocouples installed next to the strain gauges. To protect the instruments, a 1.5mm of epoxy resin was applied on the piles surface resulting in a final pile diameter of 22mm.

To simulate the heating of the energy piles, a heating rod was fabricated by coiling a heating wire around a hollow aluminium tube and was inserted in the piles cavity. The space between the heater and the inner wall of the piles was backfilled with Toyoura sand to improve heat conduction. To account for the model energy piles increase in self-weight, the reference pile was also backfilled with Toyoura sand.

The loading was performed using a hydraulic jack with servo valve control system. A load cell was used to record the applied load and a LVDT transducer to measure the piston movement.

The reference pile was loaded first, following the procedure recommended by ASTM D1143M-07. Loads were applied at 2.5 min intervals at 200N increments, until the pile settlement exceeded 10% of the pile diameter (2.2mm). After the final load increment the pile was unloaded in 5min intervals in four equal unloading steps.

Two thermomechanical tests were then performed. The model energy pile EP1 temperature was increased from 22°C to 37°C in 10 minutes (ΔT=15°C) and the model energy pile EP2 temperature from 22°C to 52°C (ΔT=30°C) in 10 minutes. Then, the temperatures were kept constant for 110 minutes. The two energy piles were then

loaded and unloaded using the same procedure as the one employed for the reference pile.
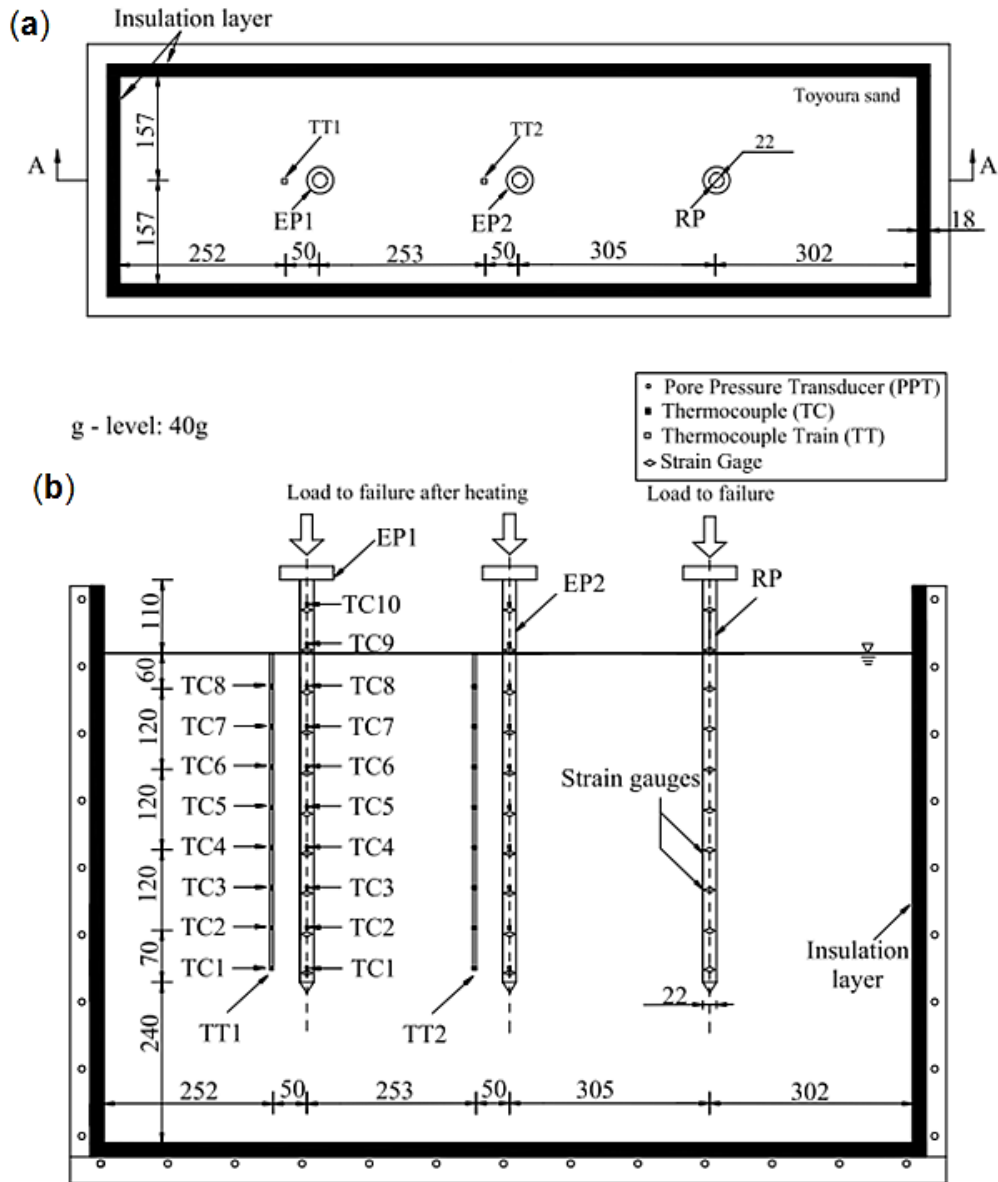
Figure 4-1 Schematic diagrams of the centrifuge package (Ng et al. 2014b): (a) Plan view of the three model piles: RP, EP1, EP2, (b) Elevation view of the three model piles: RP, EP1, EP2.

4.4.3 Axisymmetric finite element model

The model-scale piles were discretised in the finite element simulations presented hereafter using the finite element code Lagamine (University of Liège, Belgium) and the appropriate scale factors were employed for reporting the obtained results at prototype scale. The geometry and boundary conditions are represented in Figure 4-2 a and b. Axisymmetric conditions are considered, with the axis of symmetry on the left

side of the mesh. The finite element model is composed of 266 quadrilateral thermo-hydro-mechanical quadrilateral elements with 8 nodes and 4 integration points and two linear elements with 3 nodes and 2 integration points for the application of the mechanical load at the pile head. The pile soil interface was modelled using a layer of thermo-hydro-mechanical quadrilateral elements with an aspect ratio (height/width) of 9.8.

Soil and soil-pile interface properties				Pile properties	
E	11 MPa	δ'	28°	E	27.8 GPa
υ	0.20	ψ'	9°	υ	0.33
ρ_s	2654 kg/m³	ψ'_{int}	1.8°	ρ_s	2640 kg/m³
n	0.42	k^{int}	10^{-14} m²	n	0.15
c'	1 kPa	α	10 μm/m/°C	α	22.2 μm/m/°C
φ'_{max}	38°	λ	3 W/mK	λ	54.7 W/mK
φ'_{max}	31°	c_p	2339 J/kgK	c_p	863 J/kgK

Table 4.2 Material properties for the soil, the soil-pile interface, and the pile used for the numerical simulations (Rotta Loria et al. 2015).

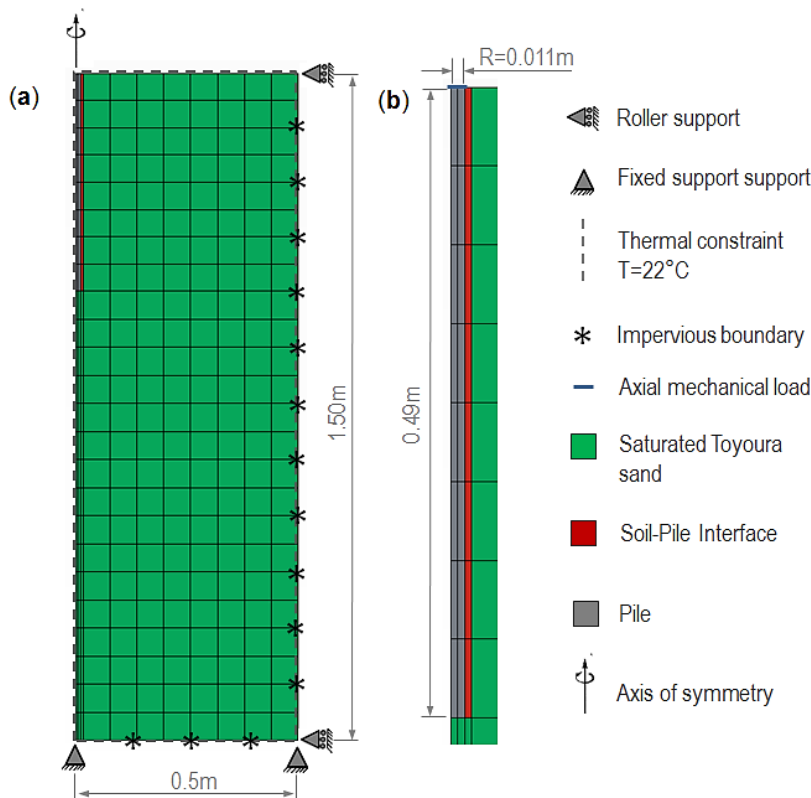**Figure 4-2 (a) Finite element mesh used to simulate the real-scale problem, (b) Zoom over the elements representing the pile and the pile soil interface.**

The considered mechanical, thermal and hydraulic boundary conditions are summarized in fig Figure 4-2 a and b. The initial stress state due to gravity in the pile and in the soil is considered geostatic and is determined assuming a coefficient of earth

pressure at rest K_0 according to the formula proposed by Jaky. The initial temperature in the model is set to 22°C. The initial pore water pressure corresponds to the hydrostatic profile with the water table located at the top surface. The numerical analysis was performed in time-scaled conditions.

A summary of the relevant properties used in the numerical simulations is presented in table Table 4.2.

4.4.4 Results and discussion

The experimental results (E) Ng et al. (2014b) are compared with the numerical simulations (S) in the following. Compression is considered negative and unless otherwise specified, all results are expressed in prototype scale.
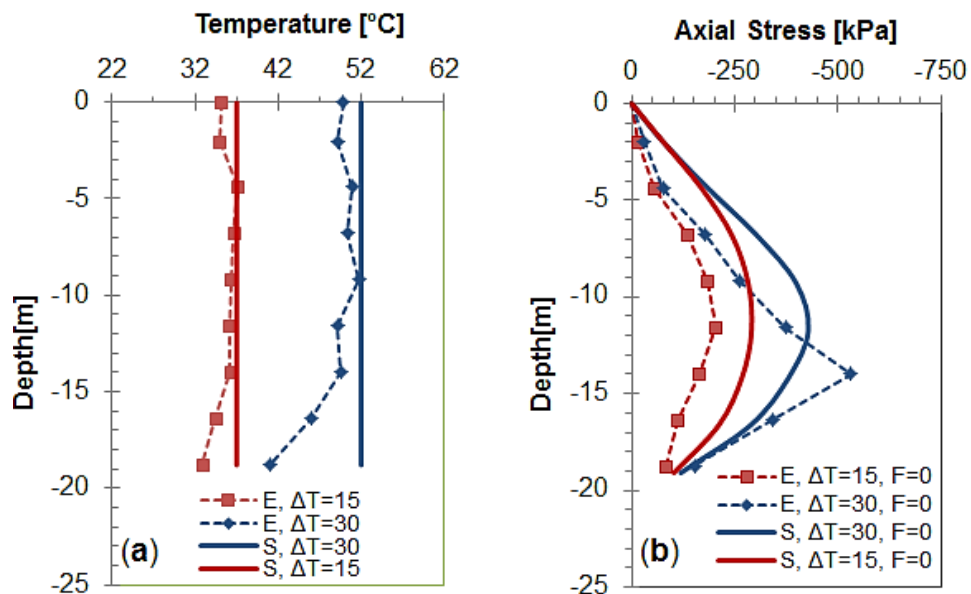
Figure 4-3 Figure 4-4 Comparison between the experimental (E) and the numerical simulations (S) for the two energy piles EP1 and EP2 (a) temperature distribution at the end of thermal loading, (b) thermal axial stresses along the pile length at the end of thermal loading.

Figure 4-3 a shows the temperature profiles along the foundation length for the energy piles EP1 and EP2 (Figure 2-26) at the end of the constant heating phase and prior to the application of the axial load for both the centrifuge tests and the numerical simulations. The temperature of the model pile EP1 (ΔT=15°C), is fairly uniform between 4.4m and 14 m below the ground level. Lower temperature values can be noticed in the pile head, probably due to the influence of the air temperature in the centrifuge package or due to enhanced thermal convection due to a higher air velocity during centrifuge spinning. The lower temperature values registered close to the pile toe may be due to the soil's thermal inertia of the soil mass under the pile. Similarly, the

model energy pile EP2 subjected to an increase in temperature of ΔT=30°C had a uniform temperature from the ground to a depth of 14 m. However larger heat loss was observed both at the pile head and toe, that can be attributed to the larger temperature gradient applied to the pile. On the other hand, the simulations of the two energy piles resulted in uniform temperature along the entire pile as a uniform temperature increase was imposed in all the nodes of the elements defining the pile.

The resulting axial stress distribution in the two energy piles after each heating phase (ΔT=15°C and ΔT=30°C) for both the centrifuge experiment and the numerical simulations are presented in Figure 4-3 (right). The maximum (absolute) compression axial stress measured experimentally in the pile EP1 for a temperature gradient of 15°C is equal to -200kPa and -530kPa in the pile EP2 for a temperature gradient of 30°C. The corresponding numerical results are -290kPa and -430kPa respectively. A temperature increase results thus in increased axial stresses that stay however limited comparing to the pile elastic domain. The differences between the resulting axial stresses between the centrifuge tests and the numerical simulations may be explained by the differences between the applied thermal loading (in the simulation a constant temperature increase was applied along the entire pile, see Figure 4-3 (b)).

Figure 4-5 Comparison between the experimental (E) and the numerical simulations (S) for the reference pile RP for different mechanical loads: axial load along the pile length.

Figure 4-5 shows the axial load distribution in the reference pile RP for different mechanical loading steps. Both experimental and numerical results show a gradual increase in shaft resistance without a remarkable increase in toe resistance for applied head load smaller than 787 kN. After this threshold, the experimental results indicate an increase of participation of the toe resistance from 280 kN to 470 kN (Ng et al. 2014b).

The numerical simulations present the same trend but at a slower rate (an increase from 119kN to 369 kN).

Similar results are obtained for the two thermomechanical tests performed on the two energy piles EP1 and EP2 that undergo a temperature increase of $\Delta T = 15°C$ and $\Delta T = 30°C$ respectively before the mechanical loading steps (Figure 4-6 and Figure 4-7). An increase of the axial compressive stresses appear with increasing temperature (see also (Ng et al. 2014b)). The axial load distribution along the piles presents a gradual increase in shaft resistance with increasing axial load. Both for the experimental and the numerical results, negative skin friction develops in the upper part of the pile for axial loads smaller than 787kN (due to pile expansion during heating).
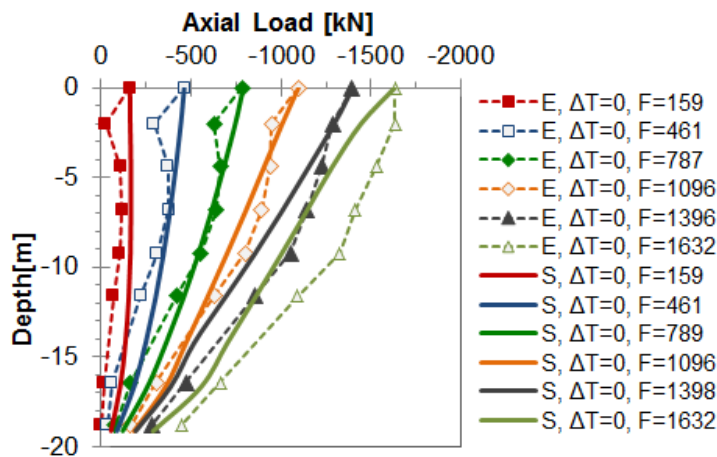

Figure 4-6 Comparison between the experimental (E) and the numerical simulations (S) for the energy pile EP1 (ΔT=15°C) for different mechanical loads: axial load along the pile length.

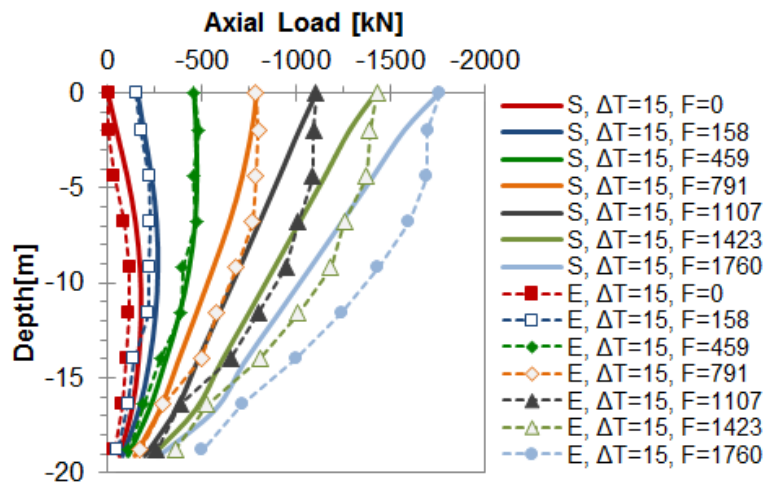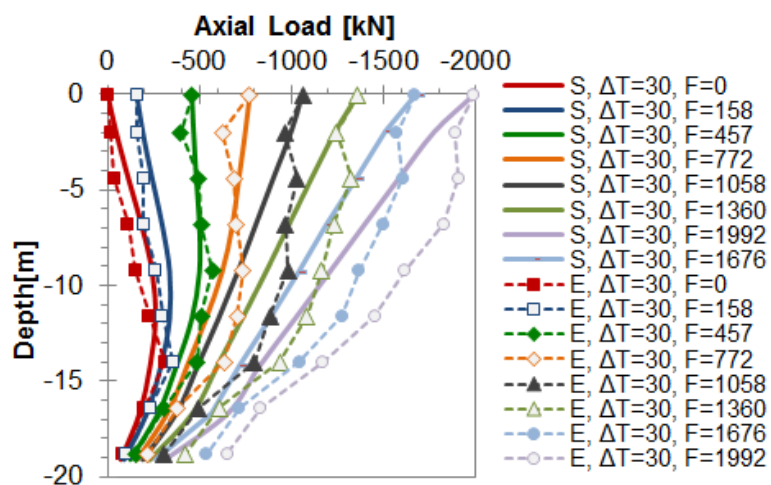**Figure 4-7 Comparison between the experimental (E) and the numerical simulations (S) for the energy pile EP2 (ΔT=30°C) for different mechanical loads: axial load along the pile length.**

4.5 Numerical model for energy piles in exploitation conditions - Sept Sorts Pile

In order to numerically investigate the effect of temperature changes on the behaviour of energy piles under exploitation conditions, the finite element method was employed to simulate the Sept Sorts case study. For this purpose, the geothermal energy pile P18 is used hereafter as reference (Figure 2-27). First, a comparison between the numerical simulations and the experimental in situ results obtained before the exploitation of the pre-treatment building is presented, in order to assess the axial load force in the pile due to mechanical loading (i.e. load transferred from the building). Then, the effect of the first cooling phase (28/11/2017-10-12/2017) is analysed. Finally, the effect of a temperature gradient of $\pm 10°C$ is considered.

4.5.1 Axisymmetric finite element model

The geometry and boundary conditions of the modelled energy pile are represented in Figure 4-8. The simulations are made under axisymmetric conditions, with the axis of symmetry on the left side of the mesh. The finite element model is made of 299 thermo-hydro-mechanical quadrilateral elements with 8 nodes and 4 integration points and two linear elements with 3 nodes and 2 integration points for the application of the mechanical load at the pile head. The pile soil interface is modelled using a layer of thermo-hydro-mechanical quadrilateral elements with an aspect ratio (height/width) of 9.8. The stratigraphy (different soil types) is considered.

The considered mechanical, thermal and hydraulic boundary conditions are summarized in fig Figure 4-2 a and b. The initial stress state due to gravity in the pile and in the soil is considered geostatic and is determined assuming a coefficient of earth pressure at rest K_0 according to the formula proposed by Jaky. The initial temperature in the model is set to 13°C (as seen in chapters 2 and 3). The initial pore water pressure corresponds to the hydrostatic profile with the water table located at the top surface. The numerical analysis was performed in time-scaled conditions.

Both the soil and the pile are assumed fully saturated and the pile behaviour is considered elastic. The soil and the soil-pile interface follow an elasto-plastic constitutive model based on the Mohr-Coulomb constitutive law. The temperature is considered uniform in the pile; hence the thermal loading is applied by imposing the same temperature variation along the pile. For simplicity, the in-situ pile temperature evolution was approximated for the simulations by a logarithmic function (Figure 4-9).
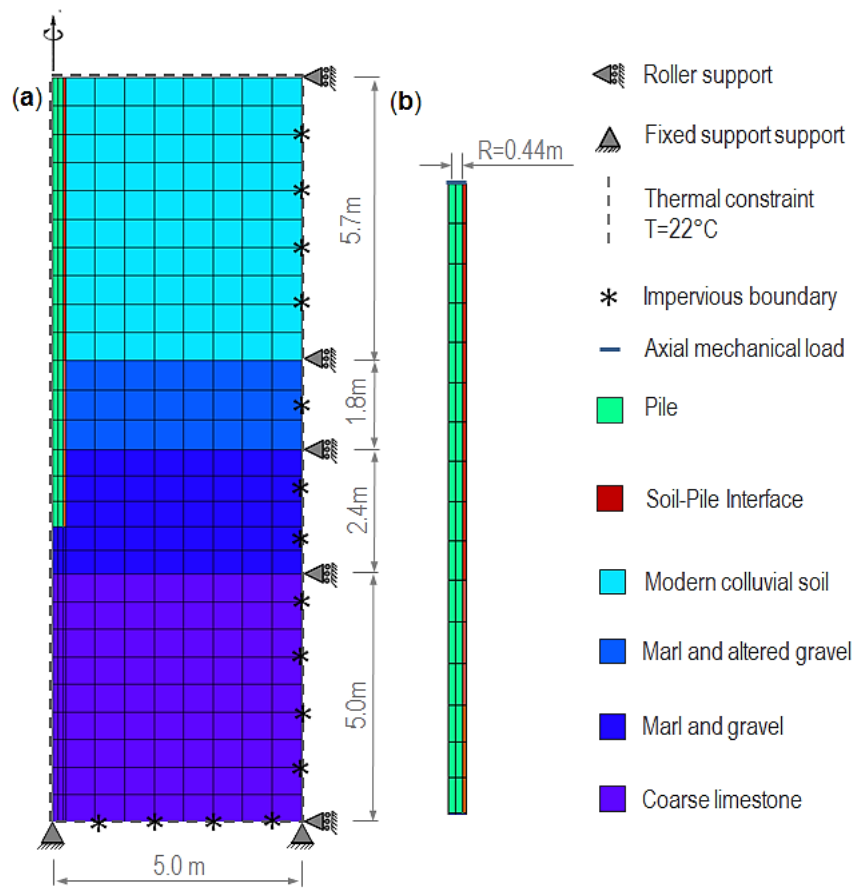
Figure 4-8 Sept Sorts (a) Finite element mesh, (b) Zoom over the elements representing the pile and the pile soil interface.
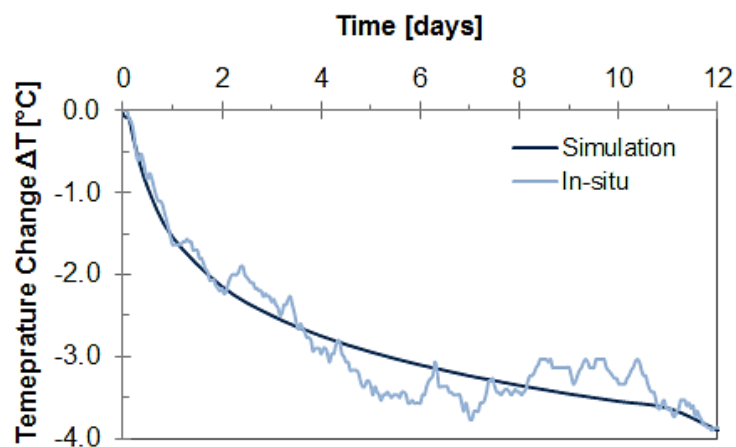

Figure 4-9 Sept Sorts - The in situ average temperature evolution and the temperature evolution used for simulations.

A summary of the material properties used in the numerical simulations is presented in table Table 4.3.

Profile	ρ (kg/m3)	E (MPa)	ν (-)	c' (kPa)	φ' (°)	δ (°)	Ψ' (°)	λ (W/m/°C)	Cs (J/kg/°C)	α (μm/m/°C)
Pile	2354	3300	0.2	-	-	-	0	1.4	880	10
Modern colluvial soil	1770	6.5	0.33	1	30	20	0	1.7	1427	10
Marl and altered gravel	1540	22.3	0.33	5	25	17	0	1.8	1042	10
Marl and gravel	1540	40.5	0.33	10	25	17	0	1.8	1042	10
Coarse limestone	1450	135	0.33	50	30	20	50	2.2	862	3.3

Table 4.3 Sept Sorts - Material properties used for the numerical simulations.

In the absence of a load cell installed in the pile head, the applied axial load under exploitation conditions is difficult to determine. For the numerical simulations two scenarios are considered: (i) empty building -225kN (i.e. only the permanent loads), (ii) full load -375kN (i.e. self-weigh, exploitation loads, wind, snow). The magnitude of these loads was obtained from the pre-treatment building design documentation (PINTO 2015), which presents the results of a 3D finite element analysis of the superstructure under different design loading scenarios, performed using the software Robot Structural Analysis Professional from Autodesk.

4.5.2 Results and discussion

The experimental (E) and numerical simulations (S) results before the beginning of the exploitation of the pre-treatment building (mechanical loading) are presented in Figure 2-39. Slight differences can be noted, resulting from the uncertainties related to the soil parameters and loading, typical to real exploitation conditions. The simulations reproduce however fairly well the in-situ results (maximum difference of 35kN). The axial load distribution along the pile corresponds to that of the "empty building" scenario, before the start of the pre-treatment building's exploitation.

The results of the first cooling phase (28/11/2017-10-12/2017) are presented in Figure 4-11 a and b. The temperature of the pile P18 is uniform for the first 7m below the ground level. Lower temperature values can be noticed near the pile toe, but this is expected since the geothermal tubes are buried only up to 7m deep. A uniform temperature was considered for the simulation of the energy pile, i.e. a uniform temperature increase was imposed in all the nodes of the finite elements used for the discretisation of the pile.
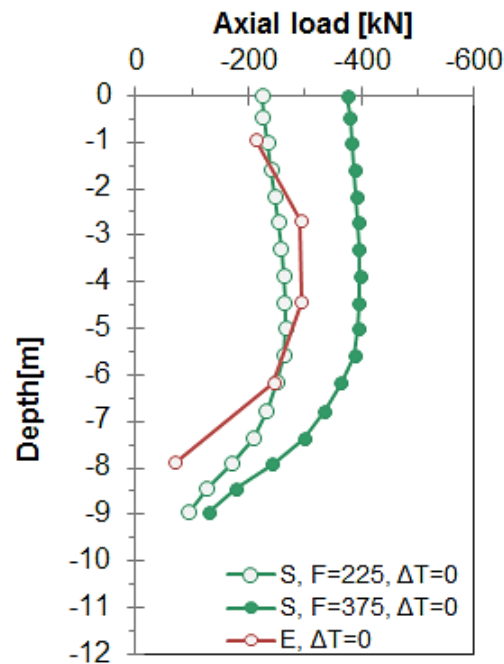
Figure 4-10 Sept Sorts - Comparison between the experimental (E) and numerical simulations (S) before the beginning of the exploitation of the pre-treatment building.

The axial load distribution along the pile P18 at the end of the first cooling phase (ΔT=3.9°C), presented in Figure 4-11 b, is typical for energy pile foundations subjected to both mechanical and thermal (cooling) loadings: decrease of the compressive axial stress all along the foundation shaft (Figure 4-11 b, Figure 4-12 b). As presented in chapter 1, restraint conditions and cooling leads to the development of thermal tensile load (Figure 4-11 b, Figure 4-12 a) that superposes to the compression mechanical axial load. Since the geothermal activation tubes are installed until a depth of 7m, the experimental results indicate no change in axial load at 7.7m. The numerical simulations indicate a slightly higher axial load compared to the experimentally obtained results. This may be due to the differences between the soil parameters used in the numerical simulations and the actual in-situ material properties.

To explore the influence of the estimated average seasonal variation (i. e. $\Delta T = 10°C$) on the energy pile's response, two numerical simulations are performed considering the empty building case configuration (i.e. -225kN, only permanent loads). Figure 4-12 a and b show the thermal axial load distribution (a) and the thermo-mechanical axial load distribution for the considered cases. Results indicate that the highest thermal axial load appears in the lower part of the pile and is equal to -153kN when heating the pile by 10°C and 149kN when cooling the pile by 10 °C. The small

difference (in absolute values) between the maximum axial load developed in the pile in the case of heating and cooling may be explained by a higher restrain posed by the toe boundary conditions during heating (restrained expansion). The toe load is -84kN for heating and 67.5kN for cooling.
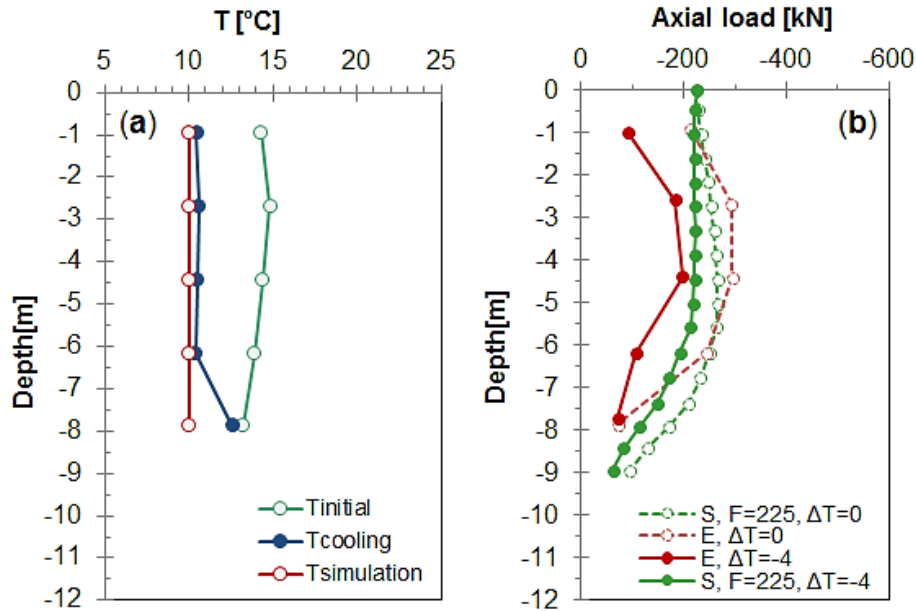
Figure 4-11 Sept Sorts - Comparison between the experimental (E) and numerical simulations (S) at the end of the first cooling period (a) temperature distribution in the energy pile P18, (b) Axial load distribution in the energy pile P18.
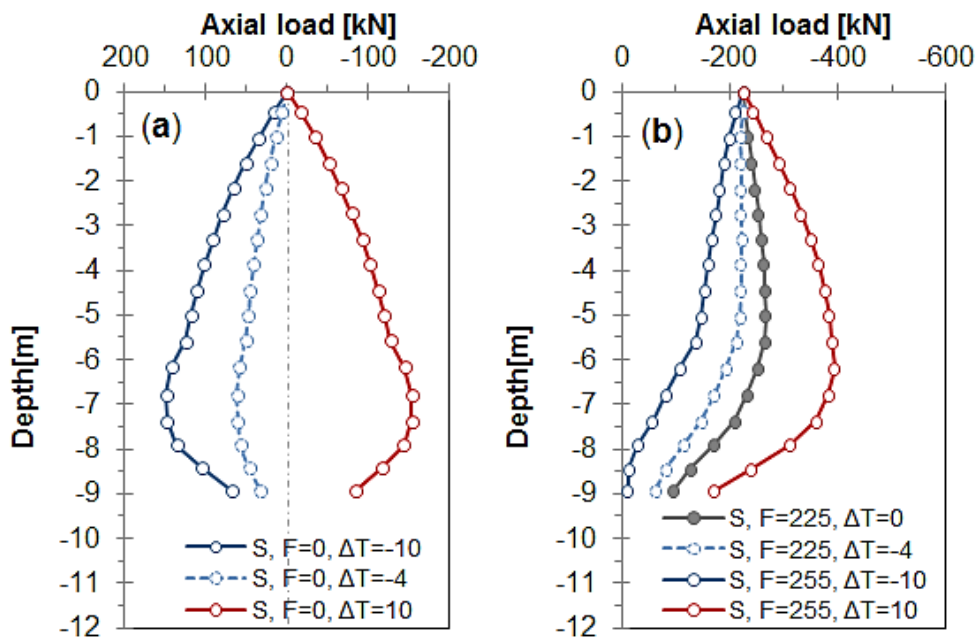
Figure 4-12 Sept Sorts, numerical simulations (S) (a) Axial load distribution along the P18 pile for different temperature gradients, (b) Axial load distribution along the P18 pile for different thermo-mechanical loading scenarios.

The pile response to thermo-mechanical loading is presented in Figure 4-12 b. As previously mentioned, pile cooling results in decreasing the compressive axial load along the entire pile by up to 150kN or up to 65% compared to mechanical loading only case. Conversely, heating increase the compressive axial load, resulting in a maximum compressive axial load in the lower part of the pile (6.17m) equal to -393kN, more significant than the applied mechanical load in the full load loading scenario (-375kN, self-weigh, exploitation loads, wind, snow).

4.6 Conclusions

The axial stress and axial load values obtained through thermo-hydro-mechanical simulations are in good agreement with the experimental results obtained through centrifuge and in situ tests. In this context, the following conclusions can be drawn:

- The use of finite elements with a significant aspect ratio to model soil-pile interfaces under different mechanical and thermal loads seems to be an apropriate method, if non specific contact elements are available.

- For low levels of applied axial load and high temperature gradient the upper part of the pile may experience negative skin friction.

- For higher mechanical and thermal loads, a larger stress component is supported by the pile toe.

- Cooling the pile reduces significantly the compressive axial load along the pile shaft (up to 35% for a temperature change of -3.9°C and up to 65% for a temeprature change of -10°C).

- Heating increases the compressive axial load distribution along the pile up to 65% with respect to the mechanical loading.

5.CONCLUSIONS AND PERSPECTIVES

This PhD thesis, collaboration between PINTO, the French National Federation of Public Works (FNTP) and Centrale Nantes (thèse CIFRE) presents a framework for understanding the factors participating in the energy piles design and execution. For this purpose, two full scale in-situ experimental campaigns have been carried out, the results of which are used to estimate the effect of geothermal activation of a pile foundation, on its bearing capacity as well as on its long-term exploitation. In order to complement the results obtained from the in-situ tests, an additional experimental campaign was performed in the laboratory in order to assess the effect of temperature and temperature cycles at the soil-pile interface. Finally, preliminary numerical simulations were presented using a thermo-hydro mechanical model able to capture the main phenomena.

5.1 Experimental outcomes

5.1.1 Ecole des Ponts Paris Tech case study: controlled loading conditions

The long-term performance of energy foundations was investigated using a full-scale pile. The pile was initially loaded to its estimated SLS capacity and then a series of three heating/cooling cycles were performed. At the end of the thermal cycles the pile was unloaded and then loaded again in order to determine its full mechanical loading capacity. The following conclusions can be drawn:

- The literature review reveals that thermal cycles with an amplitude of 21°C can be representative of the annual temperature variation in energy piles, hence each of the three performed cycles can be associated to one year of geothermal exploitation. Even though some time dependent phenomena (such as creep or heat diffusion in the soil) cannot be acurately reproduced, the experimental results thus obtained provide insight about the long term termo-mechanical behaviour of energy piles (pile head settlement, temperature in the pile, pile capacity after cyclic thermal loading).
- The temperature within the pile is uniform with the exception of the first 5 meters that are exposed to seasonal temperature variations

- The thermal cycles under a constant head load induced small irreversible pile settlement. The most important irreversible settlement occurred after the first thermal cycle.

- Good agreement was found between the estimated pile capacity and the expermental results for the mechanical loading

The results obtained in the present work could help to predict the long-term behavior of buildings equipped with energy geostructures. A similar test program is currently conducted on a second pile installed next to the one presented in this study, but for a pile head load equal to 50% of the pile's full capacity, in order to determine the impact of the magnitude of the axial load on the thermo-mechanical behavior.

5.1.2 Sept Sorts case study: geothermal exploitation conditions

The Sept Sorts case study monitored the behavior of an energy foundation for one year before and one year after its geothermal activation. The results obtained up to now confirm the feasibility of energy piles for meeting both the building's structural and heating/cooling needs. The conclusions that can be drawn from the data analysis include:

- Daily and seasonal cyclic temperature variations were recorded up to 5m below the foundation level (~8m with respect to the ground level), after which the temperature of the soil is relatively constant (13°C)

- The recorded dayly and seasonal temperature variations lead to the development of small but not negligible axial strains along the instrumented piles. The values of recorded axial strains remain nonetheless well within the concrete's elastic limit.

- During the circulation of the fluid with temperature ranging between 3.5°C and 30°C through the closed loop circuit within the pile foundation, the temperature of the reinforced concrete ranges between 16.8°C and 12.3°C. The reinforced concrete temperature is relatively uniform with depth, with the exception of the pile head sensor (0.98m) that is slightly impacted by the ambiant temperature variation and the pile toe sensor (7.70m) situated 0.7m below the geothermal loops and hence less impacted by the geothermal activation

- The thermal axial strains due to the geothermal activation of the foundation are comparable in magnitude to the values recorded before starting the operation of the ground source heat pump, but the axial strain profile within the length of the

> pile is more uniform. The recorded values are small and rest within the concrete's elastic limit

- A change in the mobilized coefficient of thermal expansion appears to occur after the first cooling phase. More data are however necessary in order to validate this observation and to understand the origin

5.1.3 Laboratory study of the effect of temperature on the pile-soil interface

The effect of cyclic temperature changes on quartz sand-concrete and carbonate sand-concrete interfaces was studied in the laboratory using an interface direct shear device adapted for thermo-mechanical loading.

It was found that the effect of 10 temperature cycles with a gradient ΔT=10°C on the mobilization of the shear strength at the soil-concrete interface is negligible. Nevertheless, the temperature cycles lead to a slight sample densification for both types of sand. The preliminary conclusions of this work therefore confirm the limited effect of temperature cycles on sandy soil pile interfaces below the level of groundwater table. These results provide also quantitative information concerning the amplitude of the volumetric strain of sandy materials subjected to temperature cycles for further development of numerical models that simulate accurately the effect of temperature at the pile-soil interface.

Further interface direct shear tests will be conducted to explore the effect of a higher number of cycles (50 to 100 cycles) and higher temperature gradients on the soil-concrete interface. A series of clay concrete-interface tests will also be conducted in order to determine the effect of temperature cycles on the shear strength parameters. This new series of experiments will help understand the relationships between the temperature and shearing behaviour of a large panel of natural soils and will aid to improve the design of more efficient energy geostructures.

5.1.4 Numerical outcomes

A 2D axisymmetric thermo-hydro-mechanical numerical model was adopted with the purpose of simulating the behavior of energy piles under various thermal and mechanical load conditions. The model was first validated with results from a centrifuge test and the Sept Sorts case study. Only preliminary results were then presented for the Sept Sorts case study.

A good agreement is found between the experimental and the numerical results. The axial load distribution along the energy pile presents an important decrease (but not

tensile loads) while cooling. Increasing the pile foundation temperature results in increasing the axial load that stayed however smaller than the pile's axial capacity. Further calculations will be conducted to simulate the influence of the temperature variation and the results will be compared with the Sept Sorts monitored energy pile.

6.REFERENCES

Abdelaziz S, Ozudogru TY (2016) Non-uniform thermal strains and stresses in energy piles. Environ Geotech 3:237–252 . doi: 10.1680/jenge.15.00032

AFNOR (2015) NF EN 1992-1-1 Eurocode 2 — Design of concrete structures — Part 1-1: General rules and rules for buildings

AFNOR (1999) NF P94-150-1 Sols : Reconnaissance et essais. Essai statique de pieu isolé sous un effort axial

AFNOR (1994) NF P94-071-1 - Août 1994 Soil investigation and testing. Direct shear test with shearbox apparatus. Part 1 : direct shear. - Sols : reconnaissance et essais

Akrouch GA, Sánchez M, Briaud JL (2014) Thermo-mechanical behavior of energy piles in high plasticity clays. Acta Geotech 9:399–412 . doi: 10.1007/s11440-014-0312-5

Al-Douri RH, Poulos HG (1992) Static and cyclic direct shear tests on carbonate sands. Geotech Test J 15:138–157 . doi: 10.1520/GTJ10236J

Amatya B, Soga K, Bourne-Webb PJ, Amis T, Laloui L (2012) Thermo-mechanical behaviour of energy piles. Géotechnique 62:503–519 . doi: 10.1680/geot.10.P.116

Andersland OB, Ladanyi B (2013) An Introduction to Frozen Ground Engineering

Boulon M (1989) Basic features of soil structure interface behaviour. Comput Geotech 7:115–131 . doi: 10.1016/0266-352X(89)90010-4

Boulon M, Nova R (1990) Modelling of soil-structure interface behaviour a comparison between elastoplastic and rate type laws. Comput Geotech 9:21–46 . doi: 10.1016/0266-352X(90)90027-S

Bourne-Webb P, Burlon S, Javed S, Kürten S, Loveridge F (2016) Analysis and design methods for energy geostructures. Renew Sustain Energy Rev 65:402–419 . doi: 10.1016/j.rser.2016.06.046

Bourne-Webb PJ (2013) An overview of observed thermal and thermo-mechanical response of piled energy foundations. Eur Geotherm Congr 2013 1–8

Bourne-Webb PJ, Amatya B, Soga K (2013) A framework for understanding energy pile behaviour. Proc Inst Civ Eng - Geotech Eng 166:170–177 . doi: 10.1680/geng.10.00098

Bourne-Webb PJ, Amatya B, Soga K, Amis T, Davidson C, Payne P (2009) Energy pile test at Lambeth College, London: geotechnical and thermodynamic aspects of pile response to heat cycles. Géotechnique 59:237–248 . doi: 10.1680/geot.2009.59.3.237

Brandl H (2006) Energy foundations and other thermo-active ground structures. Géotechnique 56:81–122 . doi: 10.1680/geot.2006.56.2.81

Cerato A, Lutenegger A (2006) Specimen Size and Scale Effects of Direct Shear Box Tests of Sands. Geotech Test J 29:100312 . doi: 10.1520/GTJ100312

CFMS-SYNTEC-SOFFONS-FNTP (2017) Recommandations pour la conception, la mise en oeuvre des géostructures thermiques

Chen K (2008) Granular Materials Under Vibration and Thermal Cycles. 122

Connolly D, Vad B, Poul M, Østergaard A, Möller B, Nielsen S, Lund H, Persson U, Nilsson D, Planenergi SW, Trier D (2012) Heat roadmap Europe 2050

DeGennaro V, Frank R (2002) Elasto-plastic analysis of the interface behaviour between granular media and structure. Comput Geotech 29:547–572 . doi: 10.1016/S0266-352X(02)00010-1

DeJong JT, White D, Randolph M (2006) Microscale observations and modelling of soil-structure interface behaviour using particle image velocimetry. Soils Found 46:15–28

DeJong JT, Zachary J, Westgate ZJ (2009) Role of Initial State, Material Properties, and Confinement Condition on Local and Global Soil-Structure Interface Behavior. J Geotech Geoenvironmental Eng 135:1646–1660 . doi: 10.1061/(ASCE)1090-0241(2009)135:11(1646)

Desai C, Drumm E, Zaman M (1985) Cyclic testing and modeling of interfaces. J Geotech Geoenvironmental Eng I:793–815 . doi: 10.1061/(ASCE)0733-9410(1985)111:6(793)

Di Donna A (2014) Thermo-mechanical aspects of energy piles

Di Donna A, Ferrari A, Laloui L (2016) Experimental investigations of the soil–concrete interface: physical mechanisms, cyclic mobilization, and behaviour at different temperatures. Can Geotech J 53:659–672 . doi: 10.1139/cgj-2015-0294

Di Donna A, Laloui L (2015) Response of soil subjected to thermal cyclic loading: Experimental and constitutive study. Eng Geol 190:65–76 . doi: 10.1016/j.enggeo.2015.03.003

EGEC (2011) Developing geothermal district heating in europe

Faizal M, Bouazza A, Mccartney JS, Haberfield C (2018) Axial and radial thermal responses of an energy pile under a 6-storey residential building. Can Geotech J 570–588 . doi: 10.1139/cgj-2018-0246

Fakharian K, Evgin E (1997) Cyclic simple shear behaviour of sand-steel interfaces under constant normal stiffness condition. J Geotech Geoenvironmental Eng 123:382–388 . doi: 10.1061/(ASCE)1090-0241(1997)123:12(1096)

Fang P, Bouazza A, Wang Z (2018) Bearing Performance of Geothermal Energy Pile Subjected to Thermal Loading. 1:710–717

Farouki OT (1981) Thermal properties of soils

Fioravante V, Ghionna VN, Pedroni S, Porcino D (1999) A constant normal stiffness direct shear box for soil-solid interface tests. Riv. Ital. di Geotec. 7–22

GEOCOM (2015) Handbook of best practices of geothermal resources management

Georgiadis M, Anagnostopoulos C, Saflekou S (1992) Centrifugal testing of laterally loaded piles in sand. Can Geotech J 29:208–216 . doi: 10.1139/t92-024

Ghionna VN, Mortara G (2002) An elastoplastic model for sand–structure interface behaviour. Géotechnique 52:41–50 . doi: 10.1680/geot.2002.52.1.41

GHSP (2012) Thermal pile design, installation and materials standards

Glisic B (2000) Fibre Optic Sensors and Behaviour in Concrete At Early Age. Ecole Polythechnique Fédérale de Lausanne

HASSAN AH (1995) Etude experimentale et numerique du comportement local et global d'une interface sol granulaire-structure. http://www.theses.fr

Hölscher P, van Tol AF, Huy NQ (2012) Rapid pile load tests in the geotechnical centrifuge. Soils Found 52:1102–1117 . doi: 10.1016/J.SANDF.2012.11.024

Horikoshi K, Randolph MF (1996) Centrifuge modelling of piled raft foundations on clay. Géotechnique 46:741–752 . doi: 10.1680/geot.1996.46.4.741

Hu L, Pu J (2004) Testing and Modeling of Soil-Structure Interface. J Geotech Geoenvironmental Eng 851–860

Kishida H, Uesugi M (1987) Tests of the interface between sand and steel in the simple shear apparatus. Géotechnique 37:45–52 . doi: 10.1680/geot.1987.37.1.45

Laloui L, Cekerevac C (2008) Non-isothermal plasticity model for cyclic behaviour of soils. Int J Numer Anal Methods Geomech 32:437–460 . doi: 10.1002/nag.629

Laloui L, Moreni M, Vulliet L (2003) Comportement d'un pieu bi-fonction, fondation et échangeur de chaleur. Can Geotech J 40:388–402 . doi: 10.1139/t02-117

Laloui L, Nuth M, Vulliet L (2006) Experimental and numerical investigations of the behaviour of a heat exchanger pile. Int J Numer Anal Methods Geomech 30:763–781 . doi: 10.1002/nag.499

Lerat P Etude de l'interface sol-structure dans les milieux granulaires à l'aide d'un nouvel appareil de cisaillement annulaire

Loveridge F (2012) The Thermal Performance of Foundation Piles used as Heat Exchangers in Ground Energy Systems. Univ Southhampt 206

Loveridge F, Powrie W (2012) Pile heat exchangers: thermal behaviour and interactions. Proc Inst Civ Eng - Geotech Eng 166:178–196 . doi: 10.1680/geng.11.00042

Loveridge F, Powrie W, Nicholson D (2014) Comparison of two different models for pile thermal response test interpretation. Acta Geotech 9:367–384 . doi: 10.1007/s11440-014-0306-3

Loveridge FA, Powrie W, Wischy M, Kiauk J (2016) Long term monitoring of CFA energy pile schemes in the UK. Energy Geotech 585–592 . doi: 10.1201/b21938-92

Low JE, Loveridge FA, Powrie W (2013) Measuring soil thermal properties for use in energy foundation design. 18Th Int Conf Soil Mech Geotech Eng 3375–3378

Mantho AT (2005) Echanges sol-atmosphere. Application a la secheresse

Marshall JK, Hunter P (1980) Effect of temperature on vibrating wire strain gauges. Strain 37–44

Martin JR, Abdelaziz SL, Olgun CG (2010) Renewable Energy Applications Using Thermo-Active Deep Foundations. Int Sci Conf CIBv 2010 289–304

McCartney JS, Murphy KD (2017) Investigation of potential dragdown/uplift effects on energy piles. Geomech Energy Environ 10:21–28 . doi: 10.1016/j.gete.2017.03.001

McCartney JS, Murphy KD (2012a) Strain Distributions in Full-Scale Energy Foundations (DFI Young Professor Paper Competition 2012). DFI J - J Deep Found Inst 6:26–38 . doi: 10.1179/dfi.2012.008

McCartney JS, Murphy KD (2012b) Strain Distributions in Full-Scale Energy Foundations. DFI J - J Deep Found Inst 6:26–38 . doi: 10.1179/dfi.2012.008

McCartney JS, Murphy KD, Henry KS (2015) Response of an energy foundation to temperature fluctuations. Proc Int Found Conf Equip Expo (IFCEE 2015) 1691–1700 . doi: 10.1061/9780784479087.153

McVay M, Zhang L, Molnit T, Lai P (1998) Centrifuge Testing of Large Laterally Loaded Pile Groups in Sands. J Geotech Geoenvironmental Eng 124:1016–1026 . doi: 10.1061/(ASCE)1090-0241(1998)124:10(1016)

Mehta PK (Povindar K, Monteiro PJM (2006) Concrete. Microstructure, Properties and Materials. McGraw-Hill

Meteo France Données climatiques à la station de Le Bourget - Novembre 2018. http://www.meteofrance.com/climat/france/le-bourget/95088001/normales. Accessed 2 Nov 2018

Minh Tang A, Yavari N, Tri Nguyen V, Hassen G, Pereira J-M, Vasilescu R, Kotronis P, Housse P-J, Fabien Szymkiewicz F (2017) Etude expérimentale du comportement thermomécanique des pieux énergétiques dans l'argile Experimental studies on the thermo-mechanical behavior of energy piles in clay. Proc 19th Int Conf Soil Mech Geotech Eng 3467–3470

Mortara G, Mangiola A, Ghionna VN (2007) Cyclic shear stress degradation and post-cyclic behaviour from sand–steel interface direct shear tests. Can Geotech J 44:739–752 . doi: 10.1139/t07-019

Murphy KD, McCartney JS (2015) Seasonal Response of Energy Foundations During Building Operation. Geotech Geol Eng 33:343–356 . doi: 10.1007/s10706-014-9802-3

Ng CWW, Shi C, Gunawan A, Laloui L (2014a) Centrifuge modelling of energy piles subjected to heating and cooling cycles in clay. Géotechnique Lett 4:310–316 . doi: 10.1680/geolett.14.00063

Ng CWW, Shi C, Gunawan A, Laloui L, Liu HL (2014b) Centrifuge modelling of heating effects on energy pile performance in saturated sand. Can Geotech J 1–44

Ng CWW, Wang SH, Zhou C (2016) Volume change behaviour of saturated sand under thermal cycles. Géotechnique Lett 6:124–131 . doi: 10.1680/jgele.15.00148

Nguyen VT (2017) Comportement thermique et thermo-mécanique des pieux énergétiques. Université Paris-Est

Nguyen VT, Tang AM, Pereira JM (2017) Long-term thermo-mechanical behavior of energy pile in dry sand. Acta Geotech 12:729–737 . doi: 10.1007/s11440-017-0539-z

Olgun CG, Bowers GA (2016) Experimental investigation of energy pile response for bridge deck deicing applications. DFI J 10:41–51 . doi: 10.1080/19375247.2016.1166314

Olgun CG, Ozudogru TY, Abdelaziz SL, Senol A (2015) Long-term performance of heat exchanger piles. Acta Geotech 10:553–569 . doi: 10.1007/s11440-014-0334-z

Palmeira EM, Milligan GWE (1989) Scale effects in direct shear tests on sand. In: Proceedings ofthe 12th Interna- tional Conference on Soil Mechanics andFoundation Engineer- ing. pp 739–742

PINTO (2015) Note de calcul bâtiment de prétraitement

Porcino D, Fioravante V, Ghionna VN, Pedroni S (2003) Interface behavior of sands from constant normal stiffness direct shear tests. Geotech Test J 26:289–301 . doi: 10.1520/GTJ11308J

Pra-Ai S (2013) Behaviour of interfaces subjected to a large number of cycles. Application to piles. 353

Rammal D, Mroueh H, Burlon S (2018) Impact of thermal solicitations on the design of energy piles. Renew Sustain Energy Rev 92:111–120 . doi: 10.1016/j.rser.2018.04.049

Rees SJ (2016) Advances in Ground-Source Heat Pump Systems

Rees SW, Adjali MH, Zhou Z, Davies M, Thomas HR (2000) Ground heat transfer effects on the thermal performance of earth-contact structures. Renew Sustain energy Rev 4:213–265 . doi: 10.1016/S1364-0321(99)00018-0

Rotta Loria AF (2018) Performance-based Design of Energy Pile Foundations. DFI J - J Deep Found Inst 12:94–107 . doi: 10.1080/19375247.2018.1562600

Rotta Loria AF, Gunawan A, Shi C, Laloui L, Ng CWW (2015) Numerical modelling of energy piles in saturated sand subjected to thermo-mechanical loads. Geomech Energy Environ 1:1–15 . doi: 10.1016/j.gete.2015.03.002

Safinus S, Hossain MS, Randolph MF (2013) Comparison of stress-strain behaviour of carbonate and silicate sediments. In: Proc. 18th Int. Conf. on Soil Mechanics and Geotechnical Engineering: Challenges and Innovations in Geotechnics. pp 267–270

Said I (2007) Comportement des interfaces et modelisation des pieux sous charge axiale. Ecole des Ponts ParisTech

Sanner B, Systems O, Systems C, Pumps GH (2001) Shallow geothermal energy. Geo-Heat Cent Bull 19–26

Shakir RR, Zhu J (2009) Behavior of compacted clay-concrete interface. Front Archit Civ Eng China 3:85–92 . doi: 10.1007/s11709-009-0013-6

SIA (2005) Utilisation de la chaleur du sol par des ouvrages de fondation et de soutènement en béton. Guide pour la conception, la realization et la maintenance

Singh RM, Bouazza A, Wang B, Barry-Macaulay D, Haberfield C, Baycan S, Carden Y (2011) Geothermal Energy Pile : Thermal cum Static Load Testing. Aust Geotherm Energy Conf 2011 245–248

Sitharam T (2003) Discrete element modelling of cyclic behaviour of granular materials. Geotech Geol Eng 21:297–329

Soroka I (2013) Portland cement paste and concrete. PALGRAVE

Stewart MA, McCartney JS (2013) Centrifuge Modeling of Soil-Structure Interaction in Energy Foundations. J Geotech Geoenvironmental Eng 140:04013044 . doi: 10.1061/(asce)gt.1943-5606.0001061

Sung C, Park S, Lee S, Oh K, Choi H (2018) Thermo-mechanical behavior of cast-in-place energy piles. Energy 161:920–938 . doi: 10.1016/j.energy.2018.07.079

Suryatriyastuti ME, Mroueh H, Burlon S (2012) Understanding the temperature-induced mechanical behaviour of energy pile foundations. Renew Sustain Energy Rev 16:3344–3354 . doi: 10.1016/j.rser.2012.02.062

Suryatriyastuti ME, Mroueh H, Burlon S (2014) A load transfer approach for studying the cyclic behavior of thermo-active piles. Comput Geotech 55:378–391 . doi: 10.1016/j.compgeo.2013.09.021

Sutman M, Brettmann T, Olgun CG (2018) Full-scale in-situ tests on energy piles: Head and base-restraining effects on the structural behaviour of three energy piles. Geomech Energy Environ. doi: 10.1016/j.gete.2018.08.002

Sutman M, Olgun G, Brettmann T (2015) Full-Scale Field Testing of Energy Piles. Geotech Spec Publ 1638–1647 . doi: 10.1061/9780784479087.148

Tabucanon JT, Airey DW, Poulos HG (1995) Pile skin friction in sands from constant normal stiffness tests. Geotech Test J 18:350–364 . doi: 10.1520/GTJ11004J

Terzaghi K (1943) Theoretical soil mechanics

Tsubakihara Y, Kishida H, Nishiyama T (1993) Friction between cohesive soils and steel. Soils Found 33:145–156 . doi: https://doi.org/10.3208/sandf1972.33.2_145

Uesugi M, Kishida H (1986) Frictional resistance at yield between dry sand and mild steel. Soils Found 26:139–149

Vargas WL, McCarthy JJ (2007) Thermal expansion effects and heat conduction in granular materials. Phys Rev E - Stat Nonlinear, Soft Matter Phys 76: . doi: 10.1103/PhysRevE.76.041301

Vasilescu AR, Fauchille AL, Dano C, Kotronis P, Manirakiza R, Gotteland P (2019) Impact of temperature cycles at soil – Concrete interface for energy piles. In: Springer Series in Geomechanics and Geoengineering. pp 35–42

Vieira A, Maranha JR (2017) Thermoplastic Analysis of a Thermoactive Pile in a Normally Consolidated Clay. Int J Geomech 17:04016030 . doi: 10.1061/(ASCE)GM.1943-5622.0000666

Wang XZ, Jiao YY, Wang R, Hu MJ, Meng QS, Tan FY (2011) Engineering characteristics of the calcareous sand in Nansha Islands, South China Sea. Eng Geol 120:40–47 . doi: 10.1016/j.enggeo.2011.03.011

Williams GP, Gold LW (1977) Les températures du sol. Dig la Constr au Canada, NRC

Xiao S, Asce SM, Suleiman MT, Ph D, Asce M (2017) Soil-Concrete Interface Properties Subjected to Temperature Change s and Cycles Using Direct Shear Tests. Geotech Front 175–183 . doi: 10.1061/9780784480472.018

Xiao S, Suleiman MT, McCartney J (2014) Shear Behavior of Silty Soil and Soil-Structure Interface under Temperature Effects. Geo-Congress 4105–4114 . doi: 10.1061/9780784413272.399

Yavari N, Tang AM, Pereira J-M, Hassen G (2014) Experimental study on the mechanical behaviour of a heat exchanger pile using physical modelling. Acta Geotech 9:385–398 . doi: 10.1007/s11440-014-0310-7

Yavari N, Tang AM, Pereira J-M, Hassen G (2016a) Effect of temperature on the shear strength of soils and the soil–structure interface. Can Geotech J 53:1186–1194 . doi: 10.1139/cgj-2015-0355

Yavari N, Tang AM, Pereira JM, Hassen G (2016b) Mechanical behaviour of a small-scale energy pile in saturated clay. Géotechnique 66:878–887 . doi: 10.1680/jgeot.15.T.026

You S, Cheng X, Guo H, Yao Z (2016) Experimental study on structural response of CFG energy piles. Appl Therm Eng 96:640–651 . doi: 10.1016/j.applthermaleng.2015.11.127

Résumé: Les pieux énergétiques représentent une solution alternative intéressante, face à l'accroissement des besoins mondiaux en énergie et à la réduction de l'utilisation des énergies fossiles. L'objectif principal de la thèse est d'identifier et de quantifier les principaux facteurs influençant le dimensionnement des pieux géothermiques, qui sont impactés par les changements de température des pieux lors de leur activité. Pour ce faire, ce travail de thèse a été dressé en 3 campagnes expérimentales, dont deux à échelle réelle : (i) une première campagne à chargement thermomécanique contrôlé (Marne La Vallée), (ii) une seconde campagne en conditions d'utilisation réelles sous une station d'épuration (Sept Sorts) et (iii) une troisième campagne à l'échelle du laboratoire grâce à une nouvelle machine de cisaillement direct d'interface permettant l'étude du comportement thermo mécanique des interfaces sol-structure. Ces trois campagnes expérimentales ont pour but de quantifier l'effet de la température et des cycles de température sur le comportement des pieux énergétiques. Les premiers résultats expérimentaux de la campagne de Sept Sorts ont ensuite été simules dans le code LAGAMINE via la méthode des éléments finis, afin d'adopter une approche complémentaire permettant de mieux appréhender la réponse thermomécanique de ce type de pieu lors de l'activation géothermique.

Abstract: Energy piles, also called thermo-active piles, are an alternative solution to the increase in the global energy demand as well as in mitigating socio-economical stakes concerning the increase of energy costs due to fossil fuels. Energy piles are double purpose structures that allow transferring the loads from the superstructure to the soil and that integrate pipe circuits allowing heat exchange between the pile and the surrounding ground. The objective of this thesis is to identify and quantify the principal parameters involved in the geotechnical design of pile foundations impacted by temperature changes associated with geothermal activation. For this purpose, this research work was organized in 3 experimental campaigns: (i) A full scale load controlled test at Ecole des Ponts Paris-Tech, (ii) Full scale energy piles monitoring under real exploitation conditions at Sept Sorts, (Seine et Marne, France), (iii) Laboratory tests in order to assess the effect of temperature and temperature cycles at the soil-pile interface. The experimental results are used to estimate the effect of geothermal activation of a pile foundation, on its bearing capacity as well as on its long-term exploitation. Finally, preliminary numerical simulations were performed using a thermo-hydro mechanical model, using the finite element method code LAGAMINE able to capture the main phenomena.